DEPARTMENT OF PHYSICS
UNIVERSITY OF JYVÄSKYLÄ
RESEARCH REPORT No. 4/2017

LOW-TEMPERATURE THERMAL AND PLASMA-ENHANCED ATOMIC LAYER DEPOSITION OF METAL OXIDE THIN FILMS

BY

MARI NAPARI

Academic Dissertation
for the Degree of
Doctor of Philosophy

To be presented, by permission of the
Faculty of Mathematics and Science
of the University of Jyväskylä,
for public examination in Auditorium FYS1 of the
University of Jyväskylä on June 16th, 2017
at 12 o'clock noon

Jyväskylä, Finland
June 2017

ABSTRACT

Napari, Mari
Low-temperature thermal and plasma-enhanced atomic layer deposition of metal oxide thin films
Jyväskylä: University of Jyväskylä, 2017, 110 p. (+included articles)
Department of Physics Research Report No. 4/2017
ISSN 0075-465X
ISBN 978-951-39-7098-7 (paper copy)
ISBN 978-951-39-7099-4 (PDF)
Diss.

Atomic layer deposition (ALD) is a method for thin film fabrication with atomic level precision. This thesis focuses on low-temperature thermal and plasma-enhanced ALD and presents results on thin film growth by these techniques with examples of common ALD materials: Al_2O_3, ZnO and TiO_2.

As an example of limitations of the thermal ALD the nucleation and growth of Al_2O_3 and ZnO films on different grades of poly(methyl methacrylate) (PMMA) are presented, showing that the initiation of the growth is strongly dependent on both the deposited material and the substrate. A potential application of the ALD ZnO films in polymer surface functionalization is demonstrated by changing in the surface wettability by means of UV-illumination.

To overcome the nucleation delay in thermal ALD, room-temperature PEALD of ZnO films was demonstrated. It is shown that the growth and properties of the films depend on the PEALD reactor configuration and the plasma conditions therein. The plasma species interactions shown to be beneficial to the film growth were observed to damage the polymer substrates, the severeness depending on the polymer material.

The last part of this thesis describes plasma mode transitions in capacitively- and inductively-coupled plasmas, that are typically used in PEALD processing. In addition to the mode transition induced changes in the plasma parameters, the contribution of the different plasma species to the growth and properties of ZnO and TiO_2 films are demonstrated and discussed.

Keywords: atomic layer deposition, plasma-enhanced atomic layer deposition, zinc oxide, polymers

Author	Mari Napari Department of Physics University of Jyväskylä Jyväskylä, Finland
Supervisor	Prof. Timo Sajavaara Department of Physics University of Jyväskylä Jyväskylä, Finland
Reviewers	Dr. Matti Putkonen Technical Research Centre of Finland (VTT) Espoo, Finland
	Prof. Christophe Vallée Universités Polytech Grenoble Laboratoire des Technologies de la Microélectronique (LTM) Grenoble, France
Opponent	Prof. Christophe Detavernier Department of Solid State Sciences Ghent University Ghent, Belgium

TIIVISTELMÄ (ABSTRACT IN FINNISH)

Atomikerroskasvatus (atomic layer deposition, ALD) on menetelmä ohutkalvojen valmistamiseen atomikerroksen tarkkuudella. Tässä väitöskirjassa keskitytään metallioksidikalvojen matalan lämpötilan termiseen ja plasma-avusteiseen atomikerroskasvatukseen. Tutkimuksen kohteena oli ALD-menetelmille tyypillisien materiaalien: alumiinioksidin (Al_2O_3), sinkkioksidin (ZnO) ja titaanidioksidin (TiO_2) kasvu.

Yhtenä esimerkkinä termisen ALD:n rajoituksista esitetään alumiini- ja sinkkioksidikalvojen kasvun alkuvaihe, nk. nukleaatio, erilaisiin sovelluskohteisiin tarkoitetuille polymetyylimetakrylaattipinnoille. Työssä näytetään, että kalvon kasvu riippuu vahvasti paitsi kasvatettavasta materiaalista myös kasvatusalustan eli substraatin ominaisuuksista. ALD-kasvatettujen ZnO kalvojen soveltamista polymeeripintojen funktionalisointiin demonstroitiin muuntelemalla pintojen vettymisominaisuuksia ultraviolettivaloa käyttäen.

Termisessä atomikerroskasvatuksessa havaittu nukleaatiovaiheen viivästyminen voidaan välttää käyttämällä plasma-avusteista atomikerroskasvatusta (plasma-enhanced ALD, PEALD), joka mahdollistaa kasvatukset jopa huoneenlämmössä. Työssä näytetään, että ZnO-kalvojen kasvu ja ominaisuudet riippuvat sekä käytetyn PEALD-reaktorin konfiguraatiosta että vallitsevista plasmaolosuhteista. Lisäksi ohutkalvojen kasvulle suotuisten plasmahiukkasten vuorovaikutusten havaittiin vahingoittavan polymeerisubstraatteja, vahingon vakavuuden ollessa riippuvainen kasvatusalustan materiaalista.

Väitöskirjan loppuosassa kuvaillaan plasman eri toimintatiloja eli moodeja ja niiden välisiä siirtymiä sekä kapasitiivisesti että induktiivisesti kytketyissä plasmoissa. Näitä molempia käytetään yleisesti PEALD-prosessoinnissa. Työssä esitetään miten nämä siirtymät vaikuttavat plasman parametreihin sekä demonstroidaan eri plasmahiukkasten vaikutus ZnO- ja TiO_2-kalvojen kasvuun ja ominaisuuksiin.

PREFACE

The work reported in this thesis has been carried out at the Department of Physics, University of Jyväskylä during the years 2013–2017. I want to thank my supervisor Prof. Timo Sajavaara for guiding me through the whole process which lead to the completion of this doctoral thesis. I also thank my pre-examiners Dr. Matti Putkonen and Prof. Christophe Vallée for their effort and for providing valuable comments on the original manuscript.

This journey would have been impossible to accomplish alone, and thus I wish to express my gratitude to the past and present members of the Accelerator Based Materials Science group, especially Dr. Jari Malm for introducing me to the world of ALD, Dr. Mikko Laitinen for all-around technical support, and Dr. Jaakko Julin for the numerous hours spent in the Pelletron Lab as well as the years of (un)scientific discussion, coffee, and laughter in the small shared office.

I would also like to thank all the co-authors of the papers forming the basis of this thesis: Sami Kinnunen, Kai Arstila, Manu Lahtinen, Roope Lehto, Ola Nilsen, Kristian Weibye, Øystein Fjellvåg, Alexey Veselov, and Erik Østreng.

The work involved would not have been as pleasant if not for the great atmosphere provided by the friends and colleagues at the Department. I would also like to thank all the friends outside the University for occasionally reminding me that there is so much more in the world to wonder and enjoy.

I owe by biggest debt of gratitude to my mother Eeva Puustinen for teaching me to believe in myself. And finally, I would like to thank Olli for standing by me through this journey. I think we are ready for new adventures now.

Jyväskylä, June 2017,

Mari Napari

The work presented in this thesis was supported by Academy of Finland Center of Excellence in Nuclear and Accelerator Based Physics (Ref. 251353) and Doctoral Programme in Nuclear and Particle Physics (University of Jyväskylä). 'Hooking together European research in atomic layer deposition' (HERALD, MP1402), supported by European Cooperation in Science and Technology (COST) is acknowledged for mobility grants.

ACRONYMS AND NOMENCLATURE

AFM	Atomic force microscopy
ALD	Atomic layer deposition
ATR	Attenuated total reflection
CCP	Capacitively coupled plasma
CVD	Chemical vapor deposition
DEZ	Diethylzinc, $Zn(C_2H_5)_2$
FTIR	Fourier transform infrared spectroscopy
GPC	Growth per cycle
HIM	Helium ion microscopy
ICP	Inductively coupled plasma
IR	Infrared
OES	Optical emission spectroscopy
PC	Polycarbonate
PEALD	Plasma-enhanced atomic layer deposition
PECVD	Plasma-enhanced chemical vapour deposition
PMMA	Poly(methyl methacrylate)
RBS	Rutherford backscattering spectrometry
RF	Radio frequency
RMS	Root mean square
SEM	Scanning electron microscopy
TMA	Trimethylaluminium, $Al(CH_3)_3$
TOF-ERDA	Time-of-flight elastic recoil detection analysis
UV	Ultraviolet
XPS	X-ray photoelectron spectroscopy
XRD	X-ray diffractometry

LIST OF INCLUDED ARTICLES

PI Mari Napari, Jari Malm, Roope Lehto, Jaakko Julin, Kai Arstila, Manu Lahtinen, Timo Sajavaara. Nucleation and growth of ZnO on PMMA by low-temperature atomic layer deposition. *Journal of Vacuum Science & Technology A - Vacuum, Surfaces, and Films 33 (2015) 01A128.*

PII Mari Napari, Manu Lahtinen, Alexey Veselov, Jaakko Julin, Erik Østreng, Timo Sajavaara. Room-temperature plasma-enhanced atomic layer deposition of ZnO: Film growth dependence on the plasma source configuration. *Revised for publication to Surface and Coatings Technology* .

PIII Mari Napari, Olli Tarvainen, Sami Kinnunen, Jaakko Julin, Kai Arstila, Øystein Fjellvåg, Kristian Weibye, Ola Nilsen, Timo Sajavaara. The α and γ plasma modes in plasma-enhanced atomic layer deposition with O_2–N_2 capacitive discharges. *Journal of Physics D: Applied Physics 50 (2017) 095201.*

PI: The author designed the experiments, processed the samples, and performed the ellipsometry, RBS, AFM, and contact angle measurements. The author analyzed the majority of the data, interpreted the results, and wrote the manuscript.

PII: The author designed the experiments, processed the CCP-PEALD samples and contributed to ICP-PEALD sample processing. The author performed the ellipsometry, RBS, ToF-ERDA, ATR-FTIR, and AFM measurements. The author analyzed the majority of the data, interpreted the results, and wrote the manuscript.

PIII: The author designed the experiments and processed the samples. The author performed the OES measurements and rate-coefficient analysis, performed the ellipsometry, and ZnO ToF-ERDA measurements, and contributed to the XRD and XPS measurements. The author analyzed and interpreted the majority of the data and results, and wrote the manuscript.

Additionally, outside the scope of this thesis, the author has contributed to the published work in Refs. [1–8].

CONTENTS

INCLUDED ARTICLES

1 INTRODUCTION

Atomic layer deposition (ALD) has received increasing interest as a thin film deposition method during the last couple of decades [9]. The advantages of the ALD, including the controllable growth of extremely thin, uniform, and pinhole-free films conformally over complex topographies with high aspect ratios make the method unique compared to other traditional thin film deposition techniques [10].

ALD was discovered and developed independently both in Soviet Union in 1960s under the name molecular layering, and in Finland in 1970s where the technique was called atomic layer epitaxy (ALE) at the time [11, 12]. The first industrial application of ALD was electroluminescent (EL) displays [13]. Nowadays, the technological applications of ALD include e. g. semiconductor and microelectronics processing, where ALD films with high dielectric constant are used as gate oxides in the metal-oxide-semiconductor field-effect transistors (MOSFET) [14] and also in the trench capacitors for dynamic random access memories (DRAM) [15]. ALD has also been adapted in the fields of catalysts [16], micro-electro-mechanical systems (MEMS) [17], and solar energy, where the use of ALD is valued in almost every application of the photovoltaics technology, including the silicon, thin film, organic, and dye-sensitised solar cells [18, 19].

In addition to the wide range of established applications, there are emerging fields setting new opportunities and challenges for the ALD processing. For example, the thin film coatings for organic or polymer materials utilised in organic light emitting diodes (OLED) [20, 21], organic photovoltaics [22] and other flexible electronics [23], as well as in medical and biological applications [24], require deposition temperatures lower than typically used in ALD. There is also increasing need for ultrathin films of materials not yet accessible by traditional ALD. To overcome some of the challenges, plasma-enhanced ALD (PEALD) has been developed. In this approach the ALD processing freedom is increased by addition of the reactive species created in the plasma. This allows to reduce the processing temperature and enables a wider choice in deposited materials [25]. However, the use of PEALD can also lead in compromising the film conformality and quality, and the exposure to the plasma can cause degradation of the films and the substrates [26].

Metal oxide thin films, such as Al_2O_3, ZnO, and TiO_2, are among the most common materials grown by ALD [27]. They are also materials that are used in a variety of applications due to their characteristic features. ALD Al_2O_3 is an electric insulator with high dielectric constant, and has also properties ideal for e. g. moisture barrier and encapsulation applications [28]. ZnO and TiO_2 are both wide band-gap semiconductors, and are applicable in e. g. catalysts, solar cells, and sensor technology [19, 29, 30].

This thesis focuses on the low-temperature ALD and PEALD of metal oxide coatings on polymers. The principle of the thermal ALD, and an introduction to the plasma basics and PEALD are presented in the following chapters, together with a brief discussion of the experimental techniques used in this work. Chapters 5–7 present the low-temperature ALD and PEALD and show the results of the experimental work in accordance of the order of the corresponding published articles PI, PII, and PIII. Chapter 5 describes the nucleation and growth of the ALD ZnO and Al_2O_3 thin films on poly(methyl methacrylate) (PMMA) surfaces, and in Chapter 6 the ZnO growth on PMMA and polycarbonate (PC) by means of room-temperature PEALD, and the effect of different PEALD plasma configurations on the film growth are presented. In Chapter 6 the properties of plasma and the plasma mode transitions on the PEALD growth of ZnO and TiO_2 are shown. In addition to the results of the mode transition in the capacitively-coupled plasma, published in PIII, the observations regarding the inductively-coupled plasma PEALD are summarised.

2 ATOMIC LAYER DEPOSITION

2.1 Principles of ALD

Atomic layer deposition is a surface-limited chemical thin film deposition technique. In ideal ALD each atomic layer is formed as a result of one reaction cycle, which consists of sequential self-terminating gas-solid chemical reactions separated by inert gas purges. An ALD reaction cycle involving two reactants, called precursors, is applied in steps including: 1) Self-terminating reaction of the 1st precursor, 2) A purge or evacuation to remove the non-reacted precursor and the reaction by-products, 3) A self-terminating reaction of the 2nd precursor, and 4) purging or evacuating the reaction space [31]. The ALD cycle of Al_2O_3, showing the different deposition steps, is illustrated in Fig.1.

Contrary to conventional chemical vapour deposition (CVD), in ALD the gas phase precursors are not applied to the reactor simultaneously, so no gas phase reactions occur. Each ALD reaction cycle results to a constant increase in the film thickness. Hence, the deposition rate is customarily referred as the growth per cycle (GPC) in the units of nm or Å per cycle, instead of the growth rate in the units of nm per second. With the defined GPC, the film thickness can be controlled precisely by the number of the applied reaction cycles [32]. The self-terminating/-limiting nature of ALD results in continuous films with large area uniformity and conformality over high-aspect ratio topographies. The self-termination of the surface reactions makes the ALD insensitive to the precursor flux above a certain threshold, but instead the GPC depends on the deposition temperature, substrate material, and the used precursors [9]. The time required for one ALD cycle depends also on the substrate morphology, and in the case of complex topographies and porous materials longer precursor pulses and purges are needed for complete self-termination over the surface structures.

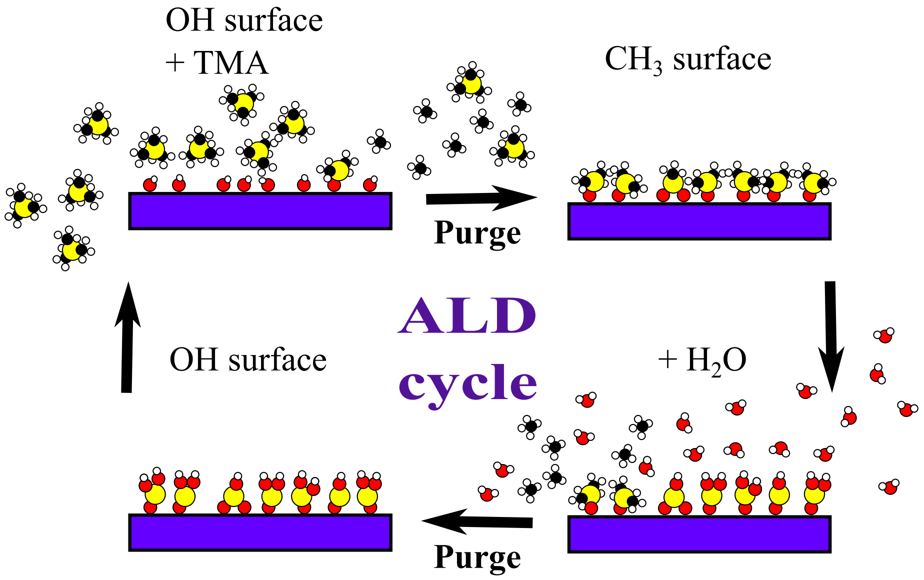

FIGURE 1 A schematic of an ALD cycle for Al_2O_3 process from trimethylaluminium ($Al(CH_3)_3$, TMA) and water precursors.

ALD processes are available for films of wide assortment of materials, with the majority being (binary and ternary) metal oxides, -nitrides, -sulfides, and more rarely -selenides and -tellurides [27]. ALD can also be used to grow pure metals, such as Cu, Pt, and Au, typically involving processes that utilize plasma as a reactant [32, 33]. In addition, organic thin films and organic-inorganic hybrids can be deposited and this variant of ALD is known as *molecular layer deposition* (MLD) [34]. The nature of the ALD enables the combination of the different processes in the fabrication of multi-layered thin films, called nanolaminates, which can be used e. g. to tune the electrical, optical and mechanical properties of the films [35]. The material selection is continuously expanding, being limited mainly by the availability of precursors for different ALD processes.

2.2 ALD surface chemistry

One way to classify the precursors used in typical ALD processes is the division to metal- and non-metal precursors. The metal precursor is molecule containing the metal atom bound with ligands, that are typically organic groups (e. g. ethyl in DEZ and methyl in TMA) or halides (e. g. Cl in $TiCl_4$). The non-metal precursor, the co-reactant, is typically water vapour in the oxide film deposition, but depending on the film material also gases such as H_2S, NH_3, and CH_4 are used for depositions of sulfides, nitrides, and carbides, respectively. The precursors can be gases, volatile liquids or even solids, the criterium being a sufficient vapour pressure, which in the case of solids and some liquids requires the heating of the precursor source. In addition to the volatility, the precursors must be thermally stable at the deposition temperature, and reactive. The surface reactions between the precursors must be complete and the reaction by-products need to be unreactive and volatile to be removed by purging [32].

The key of the successful ALD is the precursor surface chemistry. The ALD reactants must adsorb to the surface, and the adsorption needs to be irreversible and self-terminating. The adsorption is determined by the interaction of the adsorbing species and the surface. In physisorption a weak bond is formed between the surface and species due to van der Waals force, which does not cause structural changes. In chemisorption the electronic structure of the molecule is changed and a strong covalent or ionic bond is formed between the surface and adsorbed species. The physisorption can play a role in the initial nucleation on the surfaces, but generally the ALD surface reactions are based on chemisorption.

Different mechanisms for chemisorption are i) ligand exchange, where the molecule on the surface binds on it by exchanging a part of the molecule with a chemical group of the surface, ii) dissociation, where the fraction(s) of the molecule attach to the surface, and iii) association, where the intact molecule bounds to the surface. The adsorption to the surface can thus occur by either of these mechanisms, or by a combination, where e. g. a molecule chemisorbed by a ligand exchange further dissociates on the surface [36].

Moreover, chemisorption is possible only at the presence of the reactive surface sites, e. g. $-\mathrm{OH}$ and $-\mathrm{NH_x}$ species for oxides and nitrides, respectively, and no binding will occur when these sites are not available. In ALD the used molecules do not provide reactive sites to identical molecules, which leads to self-termination. In perfect surface-saturation a single molecule chemisorbs to each (identical) reactive site covering the surface. However, in reality the surface-saturation is hampered by steric hindrance, where the adsorbed molecule blocks the access to reactive sites. This causes the GPC to typically be only a fraction of a monolayer thickness. Besides the steric hindrance, initial absorption of the molecules can be hampered by the lack of the reactive sites on the surface of the substrate material, leading to a delayed nucleation and film growth [37].

The deposition of Al_2O_3 from trimethylaluminium (TMA) and water is the most studied of the ALD processes [31], and can be considered as a model ALD system, as its reactions are close to ideal under varying deposition conditions due to the extremely high reaction enthalpy (ΔH = -364 kcal) of the overall reaction:

$$2(\mathrm{Al(CH)_3})_3(g) + 3\mathrm{H_2O} \rightarrow \mathrm{Al_2O_3}(s) + 6\mathrm{CH_4}(g)\ . \tag{1}$$

For ALD, however, a more representative description is given by the half-reactions:

$$||-\mathrm{OH} + \mathrm{Al(CH_3)_3}(g) \rightarrow ||-\mathrm{O}-\mathrm{Al}-(\mathrm{CH_3})_\mathrm{x} + \mathrm{y}\,\mathrm{CH_4}(g)\ \text{, and} \tag{2}$$
$$||-\mathrm{O}-\mathrm{Al}-(\mathrm{CH_3})_\mathrm{x} + \mathrm{H_2O}(g) \rightarrow ||-\mathrm{O}-\mathrm{Al}-(\mathrm{OH})_\mathrm{x} + \mathrm{xCH_4}(g)\ , \tag{3}$$

where $||$ denotes the surface, being either hydroxyl- or methyl-terminated for the first and second half-reaction, respectively, and methane is formed as a reaction by-product in the both half-reactions. The GPC for the Al_2O_3 film growth is 1.0–1.2 Å per cycle at deposition temperature range of 150–225 °C [28, 36].

For ZnO, which is the main material studied in this thesis, the corresponding reactions of the ALD process with diethylzinc (DEZ) and water can be written as follows;

the overall reaction equation (reaction enthalpy ΔH =-70 kcal):

$$\mathrm{Zn(C_2H_5)_2}(g) + \mathrm{H_2O} \rightarrow \mathrm{ZnO}(s) + 2\mathrm{C_2H_6}(g)\ . \tag{4}$$

and the ALD half-reactions:

$$||-\mathrm{OH} + \mathrm{Zn(C_2H_5)_2}(g) \rightarrow ||-\mathrm{O}-\mathrm{Zn}-\mathrm{C_2H_5} + \mathrm{C_2H_6}(g)\ \text{, and} \tag{5}$$
$$||-\mathrm{O}-\mathrm{Zn}-\mathrm{C_2H_5} + \mathrm{H_2O}(g) \rightarrow ||-\mathrm{O}-\mathrm{Zn}-\mathrm{OH} + \mathrm{C_2H_6}\ . \tag{6}$$

This reaction at temperature range of 110–170 °C results to GPC value of 1.8–2.0 Å [29].

One approach for characterizing the ALD growth at different processing temperatures is to define a so-called *ALD window*, which considers the temperature range where the GPC value of the process remains approximately constant. Within the ALD window the ALD process is close to ideal with self-terminated reactions. At temperatures below the ALD window the precursors can condense on the surface and will not be removed during the purging step, leading to a higher GPC [38]. Alternatively, the GPC can be decreased due to the lower reactivity of the precursor with the surface species. At temperatures above the ALD window the increase in the GPC is caused by the decomposition of the precursor molecules leading to non-saturated growth. The decrease in the GPC is related to the reduction in the surface density of the reactive sites e. g. by $-$OH removal at high temperatures. However, the definition of the ALD window does not take into account any other aspects effecting the GPC of the material, such as crystal formation or other changes in the film structure.

In thermal ALD the energy for the surface reactions is provided by heating the deposition chamber and the substrate. ALD processes where the reactivity is improved by means of other than heat are categorized as *energy-enhanced ALD* [39]. The energy-enhanced ALD can utilize the reactivity of e. g. ozone (O_3), photons, or plasma species. Of these *plasma-enhanced ALD* (PEALD), being the most established of the techniques and used in PII and PIII, will be presented in Chapter 3.

2.3 Low-temperature atomic layer deposition

2.3.1 Low-temperature ALD of metal oxides

The high reactivity of the precursors used in ALD allows to perform the film deposition at low temperatures. This is especially needed for thin film coatings on temperature-sensitive substrates such as polymers and other organic materials. Many ALD processes can be performed at low temperatures due to their favourable thermochemistry [9]. For example, the exothermic nature of the ALD Al_2O_3 process enables the deposition at temperatures as low as room temperature with only a small decrease in the GPC [28]. Moreover, in some ALD processes the deposition temperature can be lowered by using a catalyst, such as NH_3 in the room-temperature deposition of SiO_2 [40].

The major issue in the low-temperature depositions is to avoid the CVD-like reactions, especially when water is used as a reactant. The removal of the physisorbed water molecules from deposition surface requires long purging times, which reduces the process efficiency as the time to complete each ALD cycle is increased [41, 42]. Also, as mentioned earlier, the precursor reactivity decreases with decreasing temperature. The studies of Al_2O_3 have shown that water is not reactive enough to remove all the methyl groups from the surface, and these persistent $-CH_3$ groups limit the TMA uptake of the next ALD cycle, thus limiting the GPC [38]. The inefficient ligand-removal applies also on other ALD-processes, such as ZnO from DEZ and water. This can lead to non-stoichiometric films and increase the content of precursor-originated impurities, such as hydrogen and carbon. These changes in the composition may further affect the structural, optical, and electrical properties of the films.

2.3.2 ALD on polymers

Despite the challenges regarding to the low-temperature ALD, there are several applications that greatly benefit from the technique. Polymer-based technologies are emerging due to their lightness, transparency, flexibility, low-cost, and ease of processing, but some properties of the polymers, such as high permeability to oxygen and water, can hinder their integration to more sophisticated systems [43]. Organic photovoltaic cells (OPVs) and organic light emitting diodes (OLEDs) are examples of electronics on polymer substrates. In these ALD can be used to deposit barrier layers to protect the devices from degradation, thus increasing their lifetime [44, 45]. ALD barrier coatings have also been applied for packaging materials [46]

Combining thin film coatings with polymers can also be used to modify and functionalize the polymer surface properties [47, 48]. ALD coatings have demonstrated to improve the polymer properties such as adhesion [49, 50], wettability [51, 52], biocompatibility [53], and anti-fouling [54]. The conformality of the ALD films enables thin film coatings on fibers and fabrics [55]. Despite of the wide selection of applications, the industrial use of the large area ALD coatings has not yet been established, mainly due to the low throughput of the ALD process. However, progress has been made on development of roll-to-roll ALD [44, 56].

The properties of the polymers, such as glass transition temperature (T_g) and the coefficient of thermal expansion, set the limit for the ALD processing temperature. These values depend on the polymer material and structure, but are generally on the order of 100 °C and some tens of ppm K^{-1} for the T_g and coefficient of thermal expansion, respectively [57]. While the T_g defines the maximum ALD temperature, the thermal expansion of the substrate can cause a stress buildup in the deposited film, and eventually lead to film cracking. The thermal expansion needs to be taken into consideration especially in applications using micro- and nanostructured polymer substrates and when the film continuity is essential.

Other distinctive features of the polymers affecting the ALD processing are the non-uniform surface structure and lack of reactive surface groups needed for the growth initiation. These aspects and their effect on the film growth are further discussed in Chapter 5, together with the PI results of the ZnO nucleation and growth on PMMA substrates.

2.4 ALD of zinc oxide

ZnO is a wide bandgap ($E_g \approx 3.37$ eV at room temperature) semiconducting material, being of interest for many thin film applications. The attractiveness of ZnO is mainly based on its optical, electric, and optoelectronic properties, and combined with the low materials cost, those make it applicable e. g. in thin film transistors, LEDs, solar cells, and in variety of sensors [30, 58]. In addition to these, ZnO is also known for its antibacterial effect [59, 60].

There are three crystalline forms of ZnO: rocksalt, cubic zinc-blende, and hexagonal wurtzite. As the zinc-blende and rocksalt forms of ZnO can be formed only under specific conditions i. e. at high temperatures and pressures, the hexagonal wurtzite structure ZnO is the most common of these three, and it also the most stable form in ambient conditions [61].

ZnO films can be produced with several methods, including sol-gel processes, magnetron sputtering, electron beam evaporation and CVD [62]. It is also among the most studied materials for ALD [29]. Due to the nature of ALD, it can be considered as an ideal technique for ZnO fabrication for sophisticated applications. As an example, Fu et.al [62] listed requirements for ZnO films for sensing applications. These requirements include strong texture, low defect concentration, uniformity in film microstructure and thickness, smooth surface and good stoichiometry (O/Zn ratio).

Reported precursors for the ZnO ALD process are zinc acetate ($Zn(CH_3COO)_2$, ZnAc) [63, 64], methylzinc isopropoxide ($(CH_3)Zn(OCH(CH_3)_2)$) [65], $ZnCl_2$ [66], dimethylzinc ($Zn(CH_3)_2$, DMZ) [67, 68], diethylzinc ($Zn(C_2H_5)_2$, DEZ) (e.g. Refs. [69–72]) , and even elemental Zn [66]. According to a review by Tynell et al. [29] DEZ is by far the most common of the used precursors. The ALD reaction for the DEZ–water process was presented earlier in Section 2.2. ZnO deposition with DEZ and water precursors is one of the few ALD processes viable at a wide temperature range from room temperature up to 400 °C [71, 73, 74], and the ALD window is estimated to be within 110–170 °C. In addition to water, also O_2 [75], O_3 [76] and N_2O [77] have been used as oxidants for ALD ZnO, but in general these require elevated deposition temperatures > 200 °C. O_2 plasma and plasma-excited H_2O are other typical oxygen sources in the plasma-enhanced ALD of ZnO [78–81]. The PEALD ZnO process will be discussed in detail in Chapter 3.

While the crystalline ALD ZnO films are always of hexagonal wurtzite structure, the crystal orientation, being either (100), (002) or (101) dominated, is influenced by the choice of precursor, deposition temperature, substrate material, purging time, and the film thickness [27, 70, 82]. In addition to the polycrystalline films, the growth of very thin films of amorphous ALD ZnO has been reported at low-temperature depositions [27, 83]. Similarly to the crystal orientation, the deposition parameters also affect the electrical, optical, and mechanical characteristics of the ZnO films [64, 84–86]. In addition to the deposition conditions, ZnO film properties can be influenced e. g. by substrate pre-treatment [87, 88], buffer layer insertion [89], or post-processing such as annealing [90].

Another approach for tuning of the ZnO properties is doping. Natively ZnO is an n-type semiconductor. The conductivity can be enhanced by introducing aluminium atoms in the ZnO matrix i. e. by adding TMA-water cycles to the ALD process. The Al content in the films can thus be precisely controlled by the ratio of Al_2O_3/ZnO ALD cycles [91, 92]. By applying nitrogen or phosphorus dopants the ZnO conductivity can be turned to p-type [93, 94]. Besides these, there are several different dopants used to tune the properties of the ALD ZnO films, including hafnium [95], titanium [96], and gallium [97].

ALD ZnO thin films have been employed in several applications, such as NO_2 gas sensing [98], solar cells [99], UV photodetectors [100], and thin film transistors (TFTs) [101]. Also an antibacterial effect against *E. coli* bacteria has been reported, showing the potential of ALD ZnO also in medical applications [102]. The antimicrobial effect, combined with the barrier properties of the ZnO films are also of interest for the applications concerning of food safety and general packaging hygiene [103]. The viability of the ALD ZnO process at low temperatures allows the deposition on temperature sensitive materials, enabling e. g. the deposition of transparent conducting ZnO layers or fabrication of TFTs for flexible electronics [104]. ZnO/Al_2O_3 nanolaminate barriers can deposited for thin film encapsulation of OLEDs [105, 106]. In addition to barrier layers [103], the ZnO coatings can act as UV-protective layers for polymeric packaging materials [107]. The ability to absorb UV light is connected to the changes in the ZnO surface properties. This feature can be utilized e. g. in controlling of the hydrophobicity/hydrophilicity of the materials by functional ZnO coatings [108], and is also shown in PI.

3 PLASMA-ENHANCED ATOMIC LAYER DEPOSITION

3.1 Plasmas in materials processing

Plasmas are widely utilized in materials processing, and are used for cleaning and etching of the materials as well as in many deposition processes. In thin film processing plasmas have many manifestations, and a variety of plasma generating devices are operated in non-reactive modes (e. g. cleaning, sputtering) with inert plasma gases as well as in reactive modes where the material can be chemically eroded or specific compounds deposited (e. g. reactive ion etching (RIE), plasma-enhanced chemical vapour deposition (PECVD)) [109].

The extensive use of plasmas stems from two essential features. One is the capability of the plasmas to efficiently generate chemically active species. The generation is initiated by the impacts on atoms/molecules by plasma electrons which have sufficient energy e. g. to break chemical bonds. The collision products including radicals and ions can undergo further reactions to form additional reactive species. Another is the formation of the energetic ions, accelerated to energies up to hundreds of electron volts adjacent to the deposition or etching surface [110].

Plasma-enhanced atomic layer deposition, also referred to as plasma-assisted ALD (PA-ALD), exploits the first of the above-mentioned features. Unlike in PECVD, the plasma is applied in pulses to activate the gaseous non-metal reactants, such as O_2 or H_2O in the PEALD of metal oxide films. The high reactivity of the plasma species enables the reduction of the deposition temperatures without compromising the film quality, which is appreciated especially when the thin films are deposited on temperature-sensitive materials. Plasma-enhancement can also lead to improved material properties as well as an increase in the GPC. In addition, the reactivity of the plasma facilitates the use of a wider selection of precursors and enables the deposition of materials that are challenging or inaccessible by the means of thermal ALD [26].

However, plasma is a complex environment, and the comprehension of both the physical and chemical aspects of the plasma, and the plasma-surface interaction from the point of view of the film deposition is important. Hence, a brief introduction to the fundamentals of low-temperature laboratory plasmas is presented before continuing to the essence of the PEALD processing.

3.2 Plasma (basics)

In general, plasma is a gas that contains freely moving neutral and charged species, including all or some of the following: molecules, atoms, positive ions, negative ions, and electrons. A plasma can be created and sustained when the density of free electrons possessing kinetic energies exceeding the ionization potential of the gas atoms or molecules, which is typically between 10 and 20 eV for the common gases, is sufficiently high. By one definition, ionized gas can be described as plasma when the density of the charged particles is adequate for the motion to be governed by their collective interaction [111].

3.2.1 Plasma criteria

The criteria for the collection of gas species to be considered as plasma are as follows [110]:

1. Plasma dimensions must be larger than the Debye length ($L >> \lambda_{\mathrm{D}}$),
2. Number of particles inside the Debye sphere is large ($N_{\mathrm{D}} >> 1$), and
3. Plasma frequency (ω_{pe}) must be higher than the average electron-neutral collision frequency.

Plasmas are on average electrically neutral i. e. the density of the positively charged ions is equal to the density of negative charge carriers (electrons and negative ions). In other words, in quasineutral plasma within macroscopic distances $n_+ = n_-$. In microscopic scale the imbalances in the charge distribution are shielded by the redistribution of the of the surrounding electrons. The shielded potential around a point-like charge q is known as the Debye potential

$$\phi(r) = \frac{q}{4\pi\varepsilon_0 r} \exp\left(-\frac{r}{\lambda_{\mathrm{D}}}\right) , \tag{7}$$

where ε_0 is vacuum permittivity, r the distance from the charge, and λ_D is the Debye length, defined as

$$\lambda_\mathrm{D} = \left(\frac{\varepsilon_0 k T_\mathrm{e}}{n_\mathrm{e} e^2} \right)^{1/2} , \tag{8}$$

where n_e is the electron density, e is the elementary charge, k is Boltzmann's constant, and kT_e denotes the electron temperature (see Section 3.2.2), usually given in units of eV [1]. Hence, the number of electrons N_D in a sphere of radius λ_D, known as the Debye sphere is

$$N_\mathrm{D} = \frac{4}{3} \pi \lambda_\mathrm{D}^3 n_\mathrm{e} \, . \tag{9}$$

The first two plasma criteria are therefore fulfilled when the Debye length is much smaller than the physical dimensions of the plasma and much larger than the average distance between plasma electrons.

The plasma (electron) oscillation frequency ω_pe can be written as:

$$\omega_\mathrm{pe} = \left(\frac{n_\mathrm{e} e^2}{\varepsilon_0 m_\mathrm{e}} \right)^{1/2} = \left(\frac{k T_\mathrm{e}}{m_\mathrm{e} \lambda_\mathrm{D}^2} \right)^{1/2} . \tag{10}$$

According to the third plasma criterion ω_pe must be higher than the electron–neutral collision frequency, which sets the lower limit for the ionization degree of the plasma.

Plasmas in materials processing are typically weakly ionized, meaning that the ionization degree, the fraction of the ionized species in the plasma, is much less than unity. In weakly ionized plasmas the dominant interactions are the neutral–neutral and electron–neutral collisions. For the electron–neutral collisions the average distance between collisions is defined by the mean free path $\lambda_\mathrm{mfp} = (1/n_\mathrm{n}\sigma)$, where n_n is the neutral density and σ is the process cross section, a measure of probability for given collision process. Hence, according to the third plasma criterion the electron oscillation length corresponding to ω_pe ($s = 2\pi \cdot (\langle v \rangle / \omega_\mathrm{pe})$) must be shorter than the λ_mfp.

The above-mentioned criteria become important when defining the properties for plasma-surface interaction, i. e. plasma sheath. The formation of the plasma sheath will be discussed later in Section 3.2.3.

---

[1] The unit for the electron temperature kT_e, typically denoted just as T_e, is electron volt (eV), which is approximately equal to the temperature of 11600 K. In materials processing plasmas the average electron temperatures are between 1 and 10 eV. By comparison, the temperatures of the neutral particles in the plasma are typically in the order of few hundred Kelvins ($\sim$0.05 eV).

3.2.2 Thermal properties of the plasmas

The collisions in the plasma can be categorized to elastic and inelastic collisions. In elastic collisions the kinetic energy is conserved and the internal energy of the colliding particles remains unchanged. In inelastic collisions the internal energy of one or both of the colliding particles is altered, for example by ionization or excitation. Another way to is categorize the collision processes by the type of the colliding particles, including electron–electron, electron–ion, electron–neutral, ion–neutral, ion–ion, and neutral–neutral collisions. These collisions can be either elastic or inelastic.

Plasmas are commonly classified by their electron densities and electron temperatures. A Maxwell-Boltzmann distribution, taking into account the elastic collisions of the electrons in thermal equilibrium, is used to define the electron temperature T_e.

The electron energy distribution function (EEDF) describes the number of electrons in a certain energy range i. e. $\mathrm{d}n_e = f(E)\ \mathrm{d}E$. For Maxwell-Boltzmann distribution this can be expressed in the terms of electron energy E as

$$f(E)\ \mathrm{d}E = \frac{2}{\pi}\frac{\sqrt{E}}{(kT_\mathrm{e})^{3/2}}\exp\left(-\frac{E}{kT_\mathrm{e}}\right)\ \mathrm{d}E, \tag{11}$$

where $f(E)$ is the EEDF, proportional to the number of electrons having a kinetic energy between E and $E + \mathrm{d}E$, and $(k)T_\mathrm{e}$ is the electron temperature, which – strictly speaking– can be defined only for the Maxwell-Boltzmann distribution. Figure 2 shows the Maxwell-Boltzmann probability distribution function for different electron temperatures T_e.

The electron kinetic energy is given classically [2] by $E = (1/2)m_\mathrm{e}v_\mathrm{e}^2$, where m_e is the mass of the electron and v_e the electron velocity [111]. The velocity distribution function (EVDF) corresponding to the EEDF in Eq. (11) is thus:

$$f_e(v)\mathrm{d}v = 4\pi\left(\frac{m_\mathrm{e}}{2\pi kT_\mathrm{e}}\right)^{3/2} v^2 \exp\left(-\frac{m_\mathrm{e}v^2}{2kT_\mathrm{e}}\right)\mathrm{d}v\ . \tag{12}$$

The average electron energy is obtained from Eq. (11) as

$$\langle E\rangle = \int Ef(E)\mathrm{d}E = \frac{3}{2}kT_\mathrm{e}\ . \tag{13}$$

---

[2] A relativistic correction is required for electrons with kinetic energy $>\sim$ 1 keV, and can therefore be neglected for typical processing plasmas.

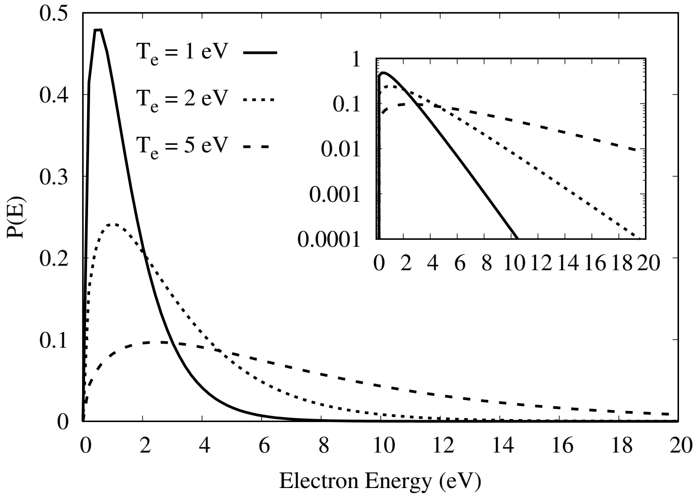

FIGURE 2 Maxwell-Boltzmann probability distribution functions for electron temperatures of T_e = 1, 2, and 5 eV. The inset shows the corresponding functions plotted in logarithmic scale.

In reality, the EEDF deviates from the Maxwellian distribution. The assumption of thermal equilibrium does not hold for the laboratory plasmas, where the average energies of the electrons, ions and neutral particles differ significantly [109]. The Maxwell-Boltzmann distribution also ignores continuous heating of the electrons by applying external power, and the interactions, such as inelastic collisions, with other plasma species. Furthermore, electron losses by diffusion and plasma-surface interactions affect the EEDF. Nevertheless, the electron temperature T_e is typically used when referring to the energy of the plasma electrons[3] [112].

3.2.3 Plasma sheaths

The phenomena causing the deviations from the Maxwell-Boltzmann EEDF also contribute to the formation of plasma sheaths at the plasma boundaries. At the plasma edge the charged particles will diffuse out of the plasma with the flux of $j = (n_{\mathrm{e,i}} v_{\mathrm{e,i}}/4)$, where $n_{\mathrm{e,i}}$ is the density of the electrons/positive ions and $v_{\mathrm{e,i}}$ the (thermal) velocity ($v_{\mathrm{e,i}} = \sqrt{3kT_{\mathrm{e,i}}/m_{\mathrm{e,i}}}$, where $m_{\mathrm{e,i}}$ is the mass of the particle). Because $m_\mathrm{e} << m_\mathrm{i}$ the electron velocity is much higher than the ion velocity [110].

---

[3] Sometimes other distribution functions, such as Druyvesteyn and Margenau, are used to describe the EEDF of the plasma. These are modifications of the Maxwellian distribution and take into account the heating of the electrons. However, the application of these requires accurate determination of the plasma conditions, such as the strength of the (alternating) electric field in the plasma [112].

When considering the non-conducting or isolated conducting surface, the initial flux of electrons to the wall is higher due to their higher mobility. This will cause the plasma to build up in positive charge as the excess of slower positive ions are left behind. Hence, an electric field will develop and decelerate the electrons while accelerating the ions, making the net current zero. The magnitude of this potential is thus in the order of $V_0 = 3kT_\mathrm{e}/e$, and declines from the plasma into the surface over the plasma sheath, which here has a thickness of the Debye length λ_D [110].

However, in most cases the boundary surfaces are conducting, and the potential of the electrode is large, and negative with respect to the plasma. In these cases the sheath thicknesses can be approximated using Child-Langmuir Law. To the potential $V = V(x)$ applies:

$$\frac{\mathrm{d}^2 V}{\mathrm{d}x^2} = -\frac{n_\mathrm{i} e}{\varepsilon_0} \,. \tag{14}$$

If n_e at the surface is zero the current density J can be given by $J = n_\mathrm{i} e v_\mathrm{i}$. Using the conservation of ion energy ($m v_\mathrm{i}^2 = 2 \cdot e \cdot V(x)$) the Eq. (14) can be written as:

$$\frac{\mathrm{d}^2 V}{\mathrm{d}x^2} = -\frac{J}{\varepsilon_0} \left(\frac{m_\mathrm{i}}{2eV} \right)^{1/2} \,. \tag{15}$$

From Eq. (15) J can be solved. Child-Langmuir Law for space-charge–limited current flow is thus:

$$J = J(x) = \frac{4}{9} \varepsilon_0 \left(\frac{2e}{m_\mathrm{i}} \right)^{1/2} \frac{V(x)^{3/2}}{x^2} \,. \tag{16}$$

Defining the sheath thickness as $x = s$ and the sheath potential $V(x) = V_{0\mathrm{s}}$, the sheath thickness can be written with the Debye length λ_D using Eq. (8) as [109]:

$$s = \frac{\sqrt{2}\lambda_\mathrm{D}}{3} \left(\frac{2V_{0\mathrm{s}}}{T_\mathrm{e}} \right)^{3/4} \,. \tag{17}$$

For example, in typical processing plasmas, where electron temperature $T_\mathrm{e} \approx$ 2 eV and the density $n_\mathrm{e} \approx 10^{10}$ cm^{-3}, the Debye length is in the order of 100 µm. In this case the sheath thickness can be of the order of 100 Debye lengths (~1 cm) as the sheath voltages are often driven to be very large compared to T_e. However, here the plasma sheath is assumed to be collisionless i. e. the ion velocity is not reduced in the collisions within the sheath [109]. Increase in the gas pressure above ca. 10^3 mbar will lead to a collisional sheath, which will cause a decrease in the sheath thickness. This reduction depends on the mean free path of the ions [113, 114]. The collisions in the sheath also decrease the ion energies, which is important from the materials processing point of view, where the energetic ions can affect the surface processes, e. g. in the PEALD film growth. The significance of the plasma sheath is discussed also in the Chapter 7, where the sheath properties play a major role in the plasma mode transition in the capacitively-coupled plasma PEALD.

3.3 Oxygen discharges

Oxygen plasmas are valued in various materials processing applications, such as oxidation, surface treatments, sterilization, etching, and thin film deposition [109, 115]. Oxygen discharges are also used in the PEALD of metal oxide films, where species generated in the plasma are used as oxidizing reactants. Therefore it is important to understand the basic characteristics of the O_2 discharges [4].

Oxygen is a simple diatomic gas. However, in an oxygen plasma, as in plasmas in general, a variety of different species can be formed. These include positive and negative ions, neutral oxygen molecules and atoms, that can be excited to a higher (chemical) potential and are typically referred to as plasma radicals, and ozone. These species are generated through inelastic collisions in the plasma, and make the oxygen plasma chemistry more complicated, especially due to the presence of the metastable atomic and molecular species and their interactions [116]. Table 1 shows a selection of different collision processes in the oxygen discharge.

TABLE 1 Representative examples of reactions in oxygen discharge [109, 117]

Electron–neutral collisions	
$e + O_2$ momentum transfer	$e + O_2(\nu) \rightarrow O_2(\nu') + e$
$e + O_2 \rightarrow {O_2}^+ + e + e$	$e + O_2 \rightarrow O_2^* + e$
$e + O_2 \rightarrow O + O^{(*)} + e$	$e + O_2 \rightarrow O^- + O$
$e + O \rightarrow O^* + e$	$e + O \rightarrow O^+ + e + e$
Electron–ion collisions	
$e + {O_2}^+ \rightarrow O_2^{+*} + e$	$e + {O_2}^+ \rightarrow O + O^{(*)}$
$e + O^+ \rightarrow O$	$e + O^- \rightarrow O + e + e$
Ion–neutral collisions	
$O^- + O \rightarrow O_2 + e$	$O^+ + O_2 \rightarrow O + {O_2}^+$
$O^- + O_2^* \rightarrow {O_2}^- + O$	$O^- + O_2^{(*)} \rightarrow O_3 + e$
Ion–ion collisions	
$O^- + {O_2}^+ \rightarrow O + O_2$	$O^- + O^+ \rightarrow O + O^{(*)}$
Neutral–neutral collisions	
$O^* + O_2 \rightarrow O + O_2^{(*)}$	$O^* + O \rightarrow O + O^{(*)}$

$*$ denotes an electronically excited state, including metastable states.
If in parentheses, $(*)$, the molecule/atom can be either on ground - or excited state.

---

[4] The plasmas considered here are sustained by electric fields, and are also referred to as (electric) discharges. A slight distinction between the terms 'plasma' and 'discharge' exists, i. e. discharges can contain regions where the criteria for plasma are not satisfied, but as a practical matter this distinction is not significant, and thus both terms can be used interchangeably.

The ionization potentials for O_2 molecule and O atom are 12.06 eV and 13.62 eV, respectively. For the generation of atomic O, the two major dissociation processes in the oxygen discharge are direct electron impact dissociation (EID) and dissociative electron attachment (DEA) via formation of an unstable ${O_2}^{-*}$ intermediate state. The complete reactions are:

$$\text{EID:} \qquad e^- + O_2(X^3\Sigma_g^-;\nu) \rightarrow O_2^{-*} \rightarrow O^-(^2P) + O(^3P) \qquad (18)$$

$$\text{DEA:} \qquad e^- + O_2(X^3\Sigma_g^-;\nu) \rightarrow O_2^{-*} \rightarrow 2O(^3P) + e^- \qquad (19)$$

The $O_2(X^3\Sigma_g^-;\nu)$ refers to the ground state O_2 on a vibrational level ν, and the (^3P) and (^2P) are the ground states of the neutral O atom and O^- ion, respectively. The energy level diagram for the O atom as well as the potential energy curves for O_2 can be found in Chapter 4.2, where they are presented in context of the optical emission spectroscopy of oxygen-containing plasmas. The threshold energies are 5.11 eV for the EID and 3.64 eV for the DEA from vibrational level $\nu = 0$ of the intial O_2, and decrease at higher vibrational levels. [118]. Due to the lower energies these processes can dominate over the ionization in the low-temperature plasmas, producing the reactive O species to be exploited in the PEALD processing.

Oxygen discharges are weakly electronegative, which means that a fraction of the negative charge is carried by ions instead of electrons [119]. The negative ions can be either O^-, ${O_2}^-$ and even ${O_3}^-$, of which the atomic O^- formed in the DEA process, are dominant [117]. However, oxygen plasmas differ from the other electronegative discharges, such as H_2, Cl_2, CF_4 and SF_6 [120]. This is due to the high concentration of metastable oxygen molecules in the discharge, that consume the negative O^- ions in the detachment processes ($O^- + O_2(a^1\Delta_g) \rightarrow$ products) [115, 121].

Gudmundsson et al. have shown by simulations the role of metastable $O_2(a^1\Delta_g)$ and $O_2(b^1\Sigma_g^+)$ molecules on the thermal properties of the O_2 disharge [115, 122]. According to their simulations the detachment process has a significant influence on the electron heating process at pressures >50 mTorr ($6.66 \cdot 10^{-2}$ mbar). Figure 3(left) shows the simulation results of the EEDF evolution in the capacitively-coupled oxygen plasma with increasing pressure. The plotted electron energy probability function is related to the EEDF as EEPF $= E^{-1/2}$EEDF. Figure 3(right) shows the Maxwell-Boltzmann distributed EEPFs corresponding to the distributions shown in Fig. 2, with plasma electron temperatures T_e =1–6 eV.

Fig. 3 shows that at low pressures the EEPF is convex compared to the Maxwellian, and the population of the low-energy electrons is relatively low. The number of low-energy electrons increases and the population of high-energy electrons de-

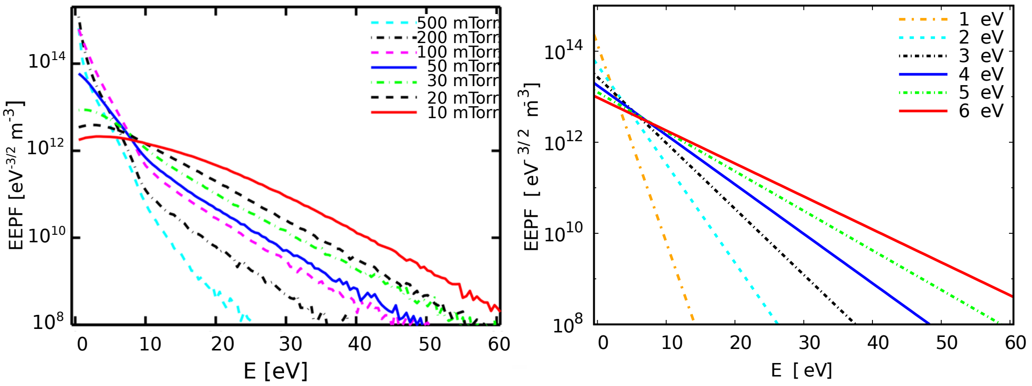

FIGURE 3 Left: The electron energy probability functions (EEPFs) for a RF capacitively coupled oxygen discharge at several pressures. Reprinted from Ref. [122] with permission from AIP Publishing. Right: Maxwell-Boltzmann distributed EEPFs for electron temperatures T_e =1–6 eV.

creases as the pressure is increased. This causes the EEPF to develop a concave shape. However, regardless of the pressure, the deviations from the Maxwell-Bolztmann distribution can still be considered relatively small, which justifies the use of the distribution when the rate coefficients for different O_2 plasma processes are calculated (Section 4.2.2).

The high density of the excited neutrals, especially the reactive atomic oxygen O(^1D)(1.97 eV), contribute also to the PEALD growth of oxides [26]. The densities of the atomic oxygen and the metastable oxygen molecules are largely governed by their interactions, mainly recombination reactions and quenching, in the plasma as well as with the walls of the plasma chamber. Rates of these reactions depend on recombination coefficient (γ) of the wall material, being higher for the metals (e. g. for atomic O, both the ground state O(^3P) and the metastable O(^1D), on stainless steel $\gamma_O \approx 0.17$ [123]) than for typical plasma device insulators such as quartz ($\gamma_O = 1.8 \cdot 10^{-4}$). The recombination coefficients for the metastable $O_2(a^1\Delta_g)$ are $\gamma_{O_2^*} = 0.007$ and $\gamma_{O_2^*} \leq 10^{-3}$ for Fe and Al surfaces, respectively [124]. The $\gamma_{O_2^*}$ can be assumed to be even lower for insulating oxide surfaces, though no reference to confirm this was found. Besides the surface material, also the prevailing conditions, such as pressure, and the temperatures of the neutral gas and the surface effect the recombination rate [125–127]. The recombination of the reactive species also inflects the growth and conformality of the PEALD grown films especially on high aspect ratio structures [128–130].

In PEALD a gas mixture is often used. In the case of oxide film deposition the so called carrier gas is typically N_2 or Ar. The addition of the inert carrier gas does not have a significant influence on the above-mentioned discharge properties, such as the electronegativity. Instead, it has been shown that the plasma electron density and O_2 dissociation into O and O^- increase by the addition of Ar to the O_2 plasma.This is due to the higher ionization potential for the Ar (15.76 eV) than for molecular and atomic oxygen, which increases the electron temperature of the plasma [131]. When N_2 carrier is used the number of different possible reactions in the O_2–N_2 discharge increases enormously [132] possibly influencing the plasma parameters depending on the O_2/N_2 ratio in the plasma. However, the formation of atomic O is somewhat insensitive to the fraction of N_2 in the mixture [133, 134], making the use of N_2 carrier suitable for PEALD processing. Yet it is possible that the reactive N species may cause nitrogen incorporation in the deposited films.

3.4 Plasma enhanced atomic layer deposition

Due to the wide variety of species in the plasma, the surface chemistry during the PEALD is more complex compared to thermal ALD. In general, the plasma radicals are considered to govern the surface reactions and film growth, but in addition, the ions and the energetic photons, mainly ultraviolet and vacuum ultraviolet (UV/VUV in ~200–350 nm/~50–200 nm range, respectively) radiation emitted by the plasma, can have influence on the the film deposition [135]. Moreover, unlike in thermal ALD, in PEALD the configuration of the reactor affects the PEALD processes. The surface chemistry of the PEALD of metal oxide films is first discussed generally in this Section before continuing to the details of the different PEALD reactor designs.

3.4.1 PEALD surface chemistry

As mentioned in Chapter 2, ALD of Al_2O_3 can be considered as a model ALD process. Similarly to the thermal ALD, the surface chemistry of Al_2O_3 PEALD process from TMA and O_2 plasma has been widely studied using variety of methods [136, 137]. Based on these studies, Langereis et al. [137] have proposed the half-reactions for the PEALD Al_2O_3, that take into account solely the atomic O species of the plasma and can be written as:

$$||{-}\mathrm{OH} + \mathrm{Al(CH_3)_3}(g) \rightarrow ||{-}\mathrm{O}{-}\mathrm{Al(CH_3)_2} + \mathrm{CH_4}(g) \tag{20}$$

$$||{-}\mathrm{O}{-}\mathrm{Al(CH_3)_2} + \underbrace{4\,\mathrm{O}(g)}_{\text{From plasma}} \rightarrow ||{-}\mathrm{O}{-}\mathrm{Al}{-}\mathrm{OH} + \mathrm{CO_2}(g) + \mathrm{H_2O}(g)\,. \tag{21}$$

When these are compared to the half-reactions of the thermal ALD of Al_2O_3 in Eqs. (2) and (3) in Section 2.2, it can be seen that the plasma does not directly influence the first half of the PEALD cycle i. e. the surface adsorption of the TMA on the –OH terminated surface. During the plasma pulse the O radicals, in addition to the Al_2O_3 generation, react with the precursor ligands forming water and carbon dioxide as reaction products.

The complexity of PEALD processing follows from what happens during the plasma pulse. The ligand exchange reactions have been studied by means of *in situ* quadrupole mass spectrometry (QMS) [136] and Fourier transform infrared spectroscopy (FTIR) [136, 138, 139]. QMS measurements have shown the formation of the CO and CO_2 species during the O_2 plasma pulsing, but also a presence of CH_x and even higher hydrocarbons C_2H_x have been detected [136]. While the reaction products and their relative concentrations can be measured with QMS, the actual surface reactions have been investigated with FTIR. It has been observed that the combustion-like reactions between surface $-CH_3$ groups and the O_2 plasma species govern the Al_2O_3 film growth both by direct oxidation leading to the $-OH$ surface termination and a formation of intermediate carbonate (CO_3) species at the surface [137–139]. Both of these can act as adsorption sites for the following TMA molecules, but the relative concentrations of the OH and CO_3 surface species are determined by the deposition temperature as well as the plasma pulse lengths [138, 139]. Moreover, the PEALD reaction products can undergo further reactions in the plasma and further redeposit on the surface [140]. These features of the PEALD with metal-organic precursors contradict the self-terminating nature of the ALD processing.

Similar combustion-like reaction mechanism governs also the PEALD of ZnO from DEZ and O_2 plasma. Alike for the Al_2O_3, the equations for the half-reactions can be written as [141]:

$$||-OH + Zn(C_2H_5)_2(g) \rightarrow ||-O-Zn-C_2H_5 + C_2H_6(g)\ \text{, and} \tag{22}$$

$$||-O-Zn-C_2H_5 + 6O(g) \rightarrow ||-O-Zn-OH + CO_2 + CO + 2H_2O\,. \tag{23}$$

The combustion-like mechanism of the PEALD ZnO has also been demonstrated by QMS measurements, showing signals corresponding to masses of CO, CO_2, H_2O, and C_2H_6 during the O_2 plasma pulse [141]. The formation of the CO products and the dissociation of the hydrogen containing species can also be observed from the optical emission spectra recorded during the plasma pulse.

Figure 4 shows the optical emission spectra of the capacitively-coupled O_2–N_2 mixture plasma used for the PEALD of ZnO. The first spectrum, recorded during the first 200 ms of the plasma pulse after the DEZ pulse, shows emission lines of the fragments of the reaction products in the plasma. After 1 s of the plasma pulse these fragments are no longer detectable. When the spectra are divided, the difference spectrum showing the reaction products is observed to be dominated by the sharp peaks originating from the H Balmer series (H_α 656 nm, H_β 486 nm). The broad rise in the difference spectrum at wavelength range of 350–600 nm is due to the CO Ångström series, with band heads at ∼450, 480, and 520 nm [142]. In this case the presence of CO_2 and H_2O among the reaction products was

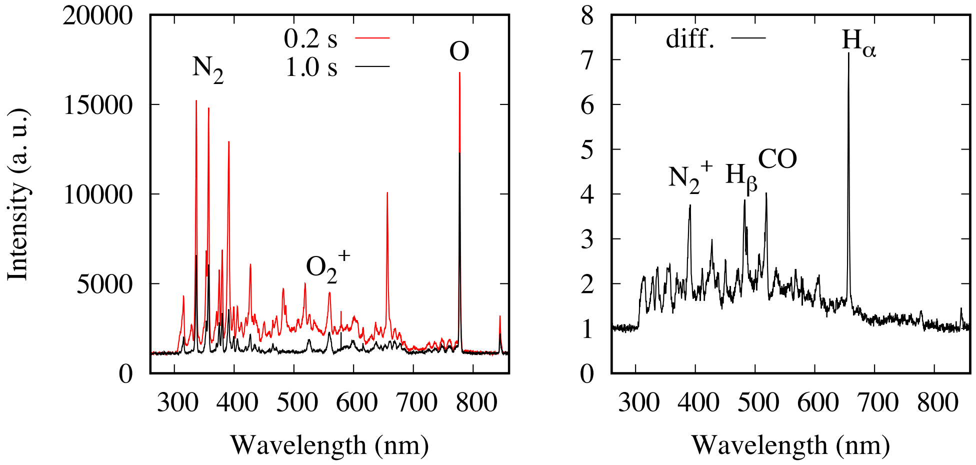

FIGURE 4 Left: The optical emission spectra recorded from the capacitively-coupled O_2–N_2 mixture plasma after 0.2 s and 1.0 s of plasma pulse after the DEZ exposure in the PEALD ZnO process. Right: The difference spectrum showing the optical emission originating from the DEZ–O_2 plasma reaction products.

not detected, possibly due to the high dissociation degree of these species in the plasma.

For the PEALD process of TiO_2 from a halide precursor $TiCl_4$ and O_2 plasma the surface chemistry can be assumed to be more straightforward. In this case the equations for the half-reactions can be written as:

$$||{-}\mathrm{O} + \mathrm{TiCl_4}(g) \rightarrow ||{-}\mathrm{O}{-}\mathrm{Ti}{-}\mathrm{Cl_2} + \mathrm{Cl_2}(g)\ , \text{ and} \tag{24}$$

$$||{-}\mathrm{O}{-}\mathrm{Ti}{-}\mathrm{Cl_2} + \mathrm{O}(g) \rightarrow ||{-}\mathrm{O}{-}\mathrm{Ti}{-}\mathrm{Ox} + \mathrm{Cl_2}(g)\ . \tag{25}$$

In the reactions it is assumed that the chlorine is released as gaseous Cl_2 that does not react with the O_2 plasma species. Unlike the processes involving metal-organic precursors, PEALD of TiO_2 process does not involve intermediate surface species. Due to this the process is more self-terminating by nature and, thus, the film composition is less sensitive to the plasma and deposition parameters, as will be shown in Chapter 7. However, the relevance of the energetic plasma ions to the TiO_2 film formation and structure is significant.

Contribution of ions and photons

As discussed in 3.2.3, a plasma sheath is formed between the plasma and adjacent surface, and the potential difference over the sheath causes the positive ions to be perpendicularly accelerated towards the surface. The (maximum) kinetic energy of the ions is proportional to the potential difference of the plasma and the surface, being thus $E_\mathrm{i} = e \cdot V_\mathrm{p}$ in the case of the grounded surface, and in the processing plasmas typically in the order of 10^1 eV. However, at the operational pressures higher than 10^{-3} mbar the ions lose energy in the collisional plasma sheath, which leads to a wider energy distribution and decrease in the average ion energy.

Ion bombardment provides additional energy to the surface. In the PEALD processing this dissipated energy can enhance the surface reactions by ligand desorption and adatom migration [143]. For example, the ion bombardment can cause re-ordering of the film structure, leading to changes in its crystallinity [143–145], and influence the film stress [143, 146]. The effect of the ion bombardment to the PEALD of ZnO and TiO_2 films will be discussed in Chapters 6 and 7. The energy of the ions at the substrate can be controlled by implementing a substrate bias, which also enables tailoring of the ion-induced effects to the films [143, 147, 148]. However, care must be taken as too high ion energies can lead to sputtering, which is detrimental to the growing film. In some cases, even without the substrate biasing, the ion energies are sufficient to cause degradation in the film properties [145].

The ion energy dissipation is typically below the damage threshold of the traditional PEALD substrates, such as Si, but enough to cause surface deterioration in more sensitive materials e. g. some polymers. Figure 5 shows AFM images of the PMMA surface before and after exposure to the ion bombardment under typical direct plasma PEALD conditions. The degradation of the surface is clearly visible as an increase in the surface roughness.

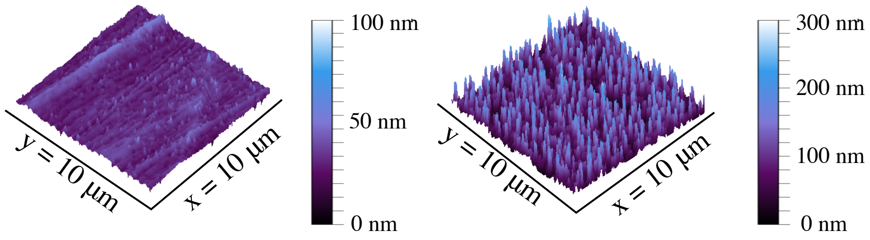

FIGURE 5 AFM images of the PMMA surface (left) before and (right) after 15 minutes of O_2–N_2 plasma exposure. The corresponding RMS surface roughesses are 5 nm and 35 nm, respectively.

In addition to radicals and ions, also energetic electromagnetic radiation, namely ultraviolet (UV) and vacuum ultraviolet (VUV), are generated in the plasma (see Section 4.2.1). Like the ion bombardment, the energetic photons can be beneficial to the film deposition. As a matter of fact, a branch of ALD, called either photo-assisted ALD or UV-enhanced ALD, has been developed. There the illumination by UV light is adapted as a part of the ALD cycle. The UV exposure has been shown to enhance the surface reactions and lead to improved film properties [149–151]. But, likewise the ions, the energetic photons can also cause damage to the films and substrates [135, 152, 153]. The extent of the substrate exposure to the plasma ions and photons is determined by the PEALD reactor configuration and the processing conditions.

3.4.2 PEALD reactor configurations

There are several different equipment configurations for PEALD, characterized by the contact between the plasma and the deposition surface, and the type of plasma species accounting for the surface reactions during the film growth [26].

In the *radical-enhanced* ALD only the neutral plasma species participate to the deposition process. This is realized by placing the radical generator (typically a microwave plasma source) to a remote location with respect to the deposition area, which eliminates the flux of energetic ions and photons to the substrate [154–156]. The recombination reactions on the way to the deposition area also reduce the flux of radical species, which leads to increased exposure times required to reach sufficient surface-saturation [156].

The distinction to a *remote plasma* ALD is that while in the radical-enhanced ALD the plasma is generated outside the line-of-sight from the deposition surface, in remote plasma ALD the plasma is generated in the vicinity of the deposition area. The plasma generators for the remote plasma ALD can be radio-frequency (RF) driven inductively-coupled- (ICP), hollow-cathode- , microwave- or electron cyclotron resonance (ECR) plasma sources [26]. In remote plasma ALD the proximity of the plasma source enables high flux of radicals to the substrate. Whether the substrate is subjected to ion bombardment or not, depends on the distance of the source as well as the pressure of the PEALD reactor. Typically the substrate is not in contact with the active plasma, but with the plasma "afterglow"[5], where the local electron temperature is too low to cause ionization. However, at low reactor pressures the plasma can still be ionizing at the substrate level [135, 157], which makes the use of the term 'remote' somewhat vague.

In the *direct plasma* ALD the deposition surface is in contact with the active plasma. In typical direct plasma setup the plasma is generated by capacitive coupling between two planar electrodes, of which the other one is powered with an RF signal and the other is grounded. In this configuration the substrate is positioned onto the grounded electrode. In the direct plasma ALD the flux of the plasma species, including the energetic ions, to the substrate is significant. This type of setup can also be operated in a remote plasma configuration. In this approach, adapted from the PECVD processing [158, 159], a grid or a perforated plate is placed be-

---

[5] In plasma (source) physics, the term afterglow is typically considered as the temporal afterglow, meaning e. g. the plasma processes occurring after the power source is switched off. However, here the afterglow is referred to as spatial afterglow, defining the regions adjacent to the plasma where no power is applied and thus no ionization is sustained.

tween the powered electrode and the substrate. This grid acts as an electrode, ostensibly restricting the plasma above it while allowing the flux of radicals to the substrate [160, 161].

Capacitively-coupled plasma PEALD

The capacitive coupling makes the generation of uniform electric fields possible. Thus, it enables high processing uniformity over large areas, determined by the size of the electrodes. As mentioned in the previous section, the capacitively-coupled plasma (CCP) configuration can be utilized in both direct and remote plasma ALD. This type of commercial PEALD reactor (Beneq TFS-200) was also used in the studies presented in Chapters 6 and 7.

Typically the capacitively-coupled plasma (CCP) setup for thin film deposition consists of a vacuum chamber containing two planar electrodes, separated by spacing in the order of 1–10 cm. The discharge between the electrodes is driven by an RF power source, usually with 13.56 MHz frequency. The typical RF driving voltage V_{RF} is 100–1000 V, and the power density 0.1–1 $\mathrm{W/cm^2}$. In CCPs the plasma densities (n_{e}) are in the order of 10^9–10^{10} $\mathrm{cm^{-3}}$, and the electron temperatures (T_{e}) between 1 and 5 eV. The CCP systems can be operated within a wide pressure range, from low pressures of 10^{-3} mbar up to atmospheric pressure [109, 162, 163], but in the PEALD applications the operating pressure is typically in the order of 0.1–10 mbar.

The influence of the operating pressure to the electron temperature in the discharge is illustrated in Fig. 6. These simulation results by Gudmundsson et al. [122] are calculated for a capacitively-coupled oxygen discharge with driving frequency of 13.56 MHz and V_{RF}=222 V. The figure shows the effective electron temperature ($T_{\mathrm{eff}} = (2/3)\langle E \rangle$) profiles between the parallel plate electrodes (diameter 14.36 cm, spacing 4.5 cm), in the pressure range of 10–500 mTorr (0.0133–0.666 mbar).

As seen in the Fig. 6, the effective electron temperature in the discharge volume is high at low pressures and decreases below 1 eV at pressures above 100 mTorr ($\sim$0.1 mbar). At the sheath edges T_{eff} is slightly higher, due to the efficient heating of electrons by the sheath oscillations [122]. Therefore, in the high pressure PEALD operation the dominating plasma processes are governed by the collisions of the low energy electrons, such as the dissociation processes of O_2. However, it is good to keep in mind that these results cannot be directly generalized to all capacitively-coupled plasmas, due to the special electronegative nature of the oxygen discharges, discussed in Section 3.3.

A schematic of the CCP-PEALD reactor setup is presented in Figure 7. In the

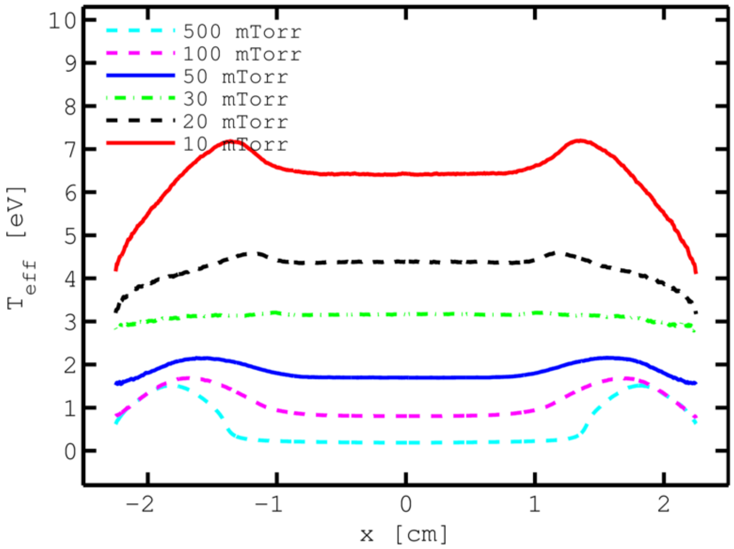

FIGURE 6 The effective electron temperature profiles between the plate electrodes of a capacitively-coupled oxygen discharge at different pressures. Reprinted from Ref. [122] with permission from AIP Publishing.

used setup the plasma gas is fed to the discharge volume through the powered electrode (⌀ = 20 cm) with a showerhead design. In the remote plasma setup a grounded metal grid, with transparency of ca. 50% is placed between the powered electrode and the substrate. The typical spacings in this setup are 2–4 cm for the electrode–grid and ca. 1 cm for the grid–substrate distances. At a pressure of 5 mbar, which is a typical operation pressure for this specific reactor, the 1 cm distance can be considered to be sufficient for effective elimination of the energetic ions passing through the grid holes. This setup can easily be converted to a direct plasma ALD configuration by removing the grid.

Typically a CCP system is driven by a single 13.56 MHz RF power supply. For efficient power transfer, the power is delivered to the discharge via an impedance matching network. Typically, T- or L-type matching networks, which are based on two adjustable capacitors, called the 'load' and 'tune' capacitors, C_L and C_T, respectively, are used for the impedance matching. The T-type network is traditionally used in RF systems, but suffers from the limited tuning range and stray capacitances at low plasma resistance, making the L-type more convenient for most of the applications. The capacitances C_L and C_T are matching to a load $R + jX$ where R is the plasma resistance and jX is the imaginary component of the load impedance and consists of the circuit and stray capacitances and the inductance of the connecting cables. For L-type network C_L and C_T can be expressed as [164]:

$$C_L = \frac{1}{2\omega R}\left[1 - \left(1 - \frac{R}{R_0}\right)\right]^{1/2} \quad \text{and} \quad C_T = \left(\omega X - \frac{1 - R/R_0}{C_L}\right)^{-1}, \qquad (26)$$

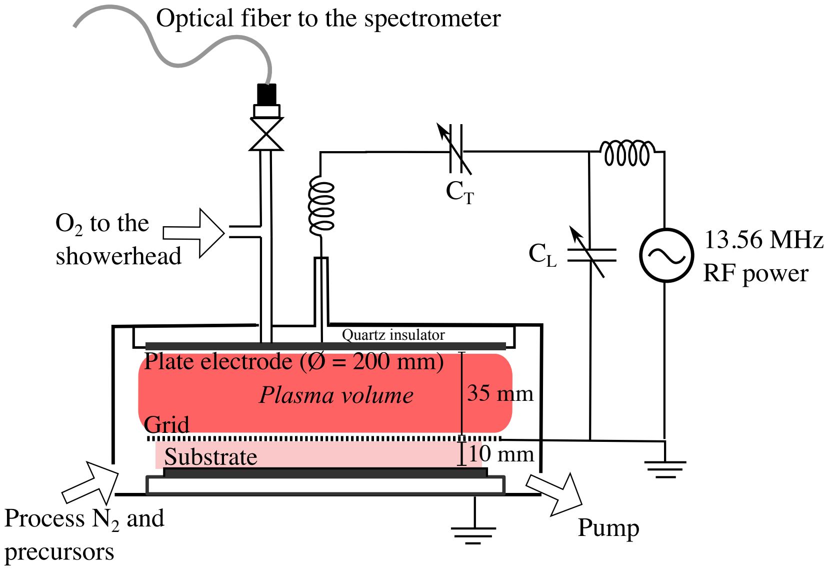

FIGURE 7 A schematic of a showerhead-type PEALD reactor with capacitively-coupled plasma configuration. Adapted from PIII with permission from IOP Publishing.

where R_0 is 50 Ω and ω is the RF (angular) frequency. Thus, as the C_L and C_T depend on the plasma resistance R, the capacitor values of the impedance matching network can be used to monitor the plasma conditions when the RF characteristics of the plasma generator cannot be directly measured. This was utilized in the paper PIII in the determination of the plasma resistance changes related to a mode transition in the CCP.

Inductively-coupled plasma PEALD

In inductively-coupled plasma (ICP) the discharge is generated by applying RF, typically 27.12 MHz, 13.56 MHz or below, power to a (non-resonant) inductive coil, which can be either planar or cylindrical . The power is transferred through oscillating electric field to the heating of the electrons. The power dissipation occurs by collisionless heating and collisional (Ohmic) heating, the dominant dissipation mechanism being governed by the gas pressure [6][109]. Typically a capacitive coupling between the coil segments also contributes to the heating. The electron densities n_e in the ICP are generally higher than in CCP, being in the

---

[6] The RF power frequency affects the local ion energy distribution (IED) in the plasma sheath, the IED being dependent on the ratio of the RF frequency ω_{RF} and the plasma ion frequency $\omega_{pi} = \left(Z^2e^2n_e/\varepsilon_0 m_i\right)^{1/2}$ [165]. However, the RF frequency has less effect on the EEDF. Especially at pressures $> 10^{-2}$ mbar and high applied powers the plasma parameters T_e and n_e can be considered to be practically frequency independent, and the EEDF follows the Maxwellian distribution [166].

order of 10^{10}–10^{12} cm^{-3}, while T_e is in the order of 1–5 eV. The operation pressure range of the ICP systems for thin film processing is typically in the order of 10^{-3}–10^{-1} mbar, but also higher pressures are used in PEALD processing [109, 167].

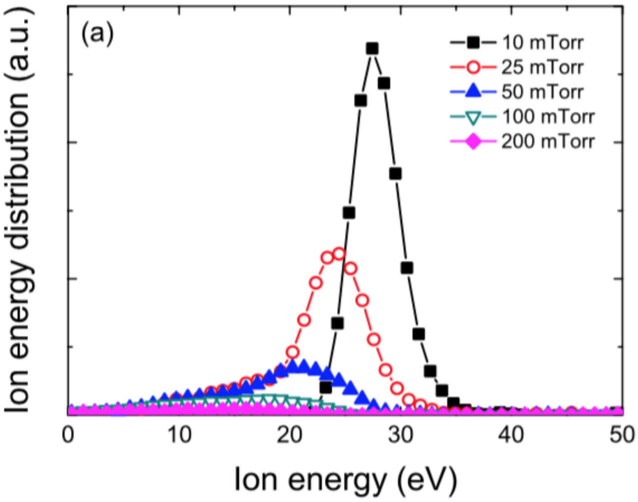

FIGURE 8 Ion energy distributions at the substrate level for an inductively-coupled Ar plasma at different gas pressures. Reprinted from [168] with permission from the Electrochemical Society.

Inductively coupled plasma is commonly used in the remote PEALD configurations. There, as mentioned in Section 3.4.2 the flux of different plasma species to the substrate is governed by the operation pressure of the system. Figure 8 by Profijt et al. [168] shows the ion energy distributions at the substrate level measured from a remote ICP-PEALD reactor operated at pressures from 10 to 200 mTorr ($1.3 \cdot 10^{-2}$– 0.27 mbar). It can be seen that both the ion energy and flux decrease significantly as the pressure is increased. The pressure increase also causes a decrease of T_e. The ICP systems are less scalable that the setups using capacitively coupled plasma, but as an advantage the substrate conditions, e. g. bias voltage, can be varied independently on the plasma operation.

A schematic of a ICP-PEALD reactor is presented in Figure 9, corresponding to the commercial reactor (Picosun R-200 Advanced) which was used in the work presented in Chapters 6 and 7. In this configuration the plasma is generated within a quartz tube surrounded by a cylindrical coil, at a distance of ca. 50 cm from the substrate. The low-frequency RF power system has a maximum output of 3000 W, and the impedance matching is realized by automatic frequency tuning (1.7–3.0 MHz). The operation pressure of this specific reactor is in the order of 5 mbar, and is sustained by continuous N_2 flow. At this pressure it is justified to assume that the ions do not contribute to the surface reactions.

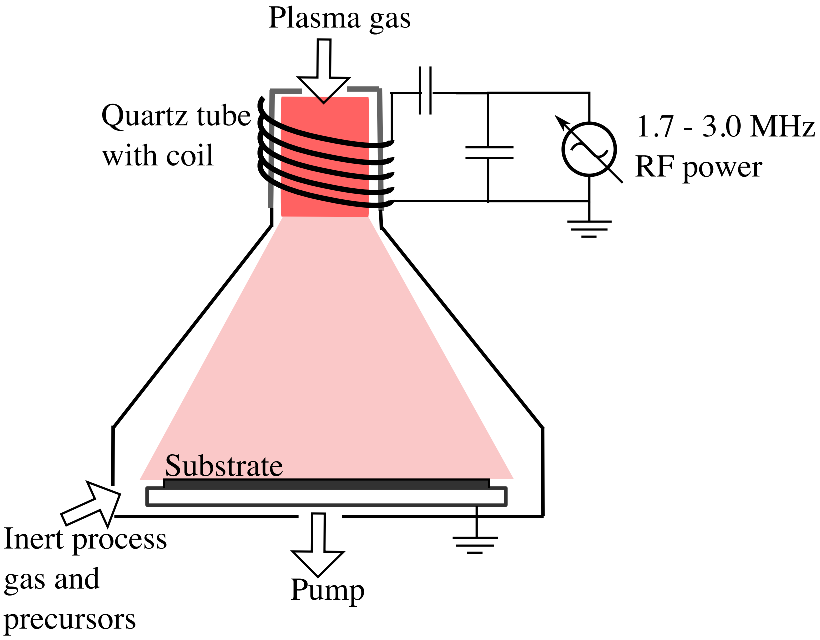

FIGURE 9 A schematic of the remote PEALD configuration with an low-frequency inductively-coupled plasma generator.

4 THIN FILM CHARACTERIZATION AND PLASMA DIAGNOSTICS

This chapter introduces briefly the main experimental characterization methods used in this thesis. The techniques are roughly divided into two categories, compositional and structural analysis of thin films. In addition, the plasma diagnostics with optical emission spectroscopy and rate coefficient analysis are presented.

4.1 Thin film characterization

4.1.1 Compositional analysis

Ion beam analysis techniques; *Rutherford Backscattering spectrometry (RBS)* and *Time-of-Flight Elastic Recoil Detection Analysis (ToF-ERDA)* are methods for quantitative determination of the elemental composition of the samples. Both of the techniques require an accelerator providing an ion beam with energy in the MeV range, and rely in the elastic scattering of the incident ion and sample material atoms. In RBS only the backscattered ions are detected while in the ToF-ERDA mainly atoms recoiling from the sample are measured. For a standard RBS measurement He ions with 1.0–2.5 MeV are used, and the film elements can be identified from the energy of the backscattered ions. The atomic concentrations can be calculated from the backscattering yields with known scattering and stopping cross sections [169].

In ToF-ERDA a heavier incident ion, in the used setup typically ^{35}Cl, ^{63}Cu, or ^{75}Br with energy from 8 to 15 MeV is used [170]. The ion collision in the target material results to energetic recoils, that are ejected from the sample and detected. In the ToF-ERDA both the velocity (time-of-flight) and the energy of the recoiled atoms are measured and can be converted to an elemental depth profile of the analysed sample [171]. An example of a time-of-flight–energy histogram and the corresponding depth profile are shown in Fig. 10.

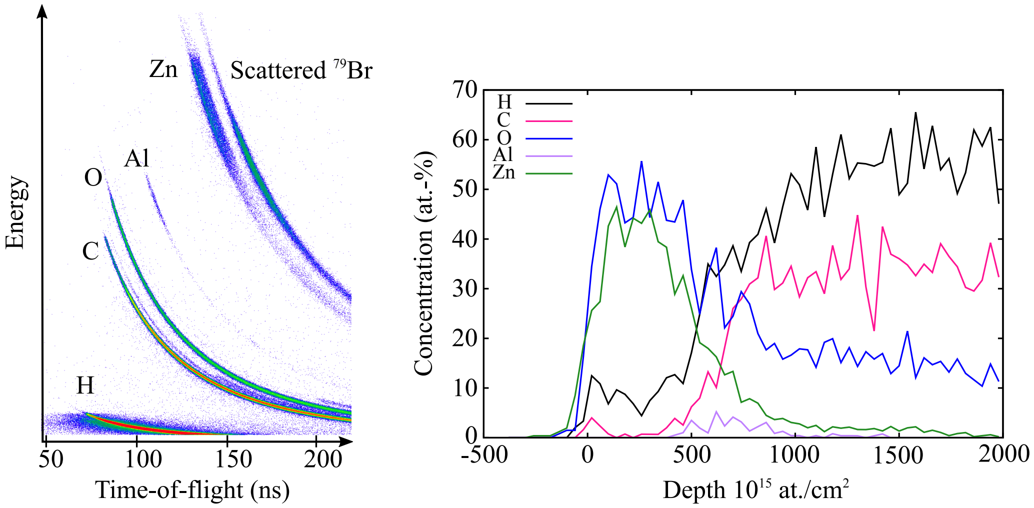

FIGURE 10 Left: Time-of-flight–energy histogram of ALD ZnO on PMMA with Al_2O_3 intermediate layer. The sample is measured with 13.6 MeV $^{79}Br^{7+}$ beam with mirror geometry. The x-axis is the time-of-flight between the timing detectors and the y-axis presents the energy of the recoils in the energy detector. Right: The corresponding depth profile, adapted from PI with permission from the American Vacuum Society.

For complementary compositional analysis providing information about the chemical environment of the films both X-ray and infrared based methods were used. In *X-ray photoelectron spectroscopy (XPS)* the sample is exposed to a monochromatic X-ray beam, typically Al K_α with E_{photon}=1.487 keV, which detaches surface electrons via the photoelectric effect. The kinetic energy of the electrons (E_{kin}) are measured and the binding energy of the electron (E_{bind}) can be determined as: $E_{\mathrm{bind}} = E_{\mathrm{photon}} - E_{\mathrm{kin}} - \phi$, where ϕ is the work function that is dependent on both the material and electron spectrometer. As the binding energies of the electrons differ based on the chemical environment, XPS can give valuable information especially about the composition of the light element impurity content in the films [172]. As a drawback, XPS is a surface-sensitive method thus giving information only for the first 1-2 nm of the film surface, that commonly contains an increased amount of impurities. Therefore a cleaning by heavy ion sputtering (typically Ar with few keV energy) is often needed. This, however, may cause changes in the surface composition and therefore complicate the quantitative analysis of the spectra [173].

Another tool for qualitative chemical analysis is *attenuated total reflection Fourier* *transform infrared spectroscopy (ATR-FTIR)*, which is a technique for identifying the chemical bonds and structure. The FTIR-method is based on the selective absorption of the infrared wavelengths by different molecular compounds thus producing a unique absorption pattern of the studied sample. In ATR-FTIR an internal reflection element, such as a Ge, ZnSe, or diamond crystal, is used in conjunction with the FTIR-spectrometer. In this approach the sample is in contact with the crystal, and a beam of infrared light passes through the crystal and undergoes multiple internal reflections in the crystal and in the sample while probing the sample surface [174] The depth of penetration d_p of the infrared beam is defined as the depth at which the intensity decreases to 36.8% (which corresponds to $1/e$, where e is the base of natural logarithm), of the initial intensity. The d_p depends on the IR wavelength and angle of incidence, as well as on the refractive indices of the crystal and sample materials, and is typically in the order of 1 µm [175].

4.1.2 Structural analysis

The surface structure characterization of the samples was perfomed using microscopy techniques. In *scanning electron microscopy (SEM)* the sample surface is scanned in a raster pattern with a focused electron beam with an energy of $\leq$30 keV. The imaging is based on the detection of the low-energy secondary electrons generated in the beam interaction with the sample atoms. The resolution of the SEM is limited by the beam focus, and to some extent by the sample material that defines the beam interaction volume. Depending on the instrument the resolution is typically 1–5 nm, though resolution of less than 0.5 nm is also achievable. The drawback of the traditional SEM is the charging of the non-conducting samples, including also thin films on electrically insulating substrates, such as polymers. To overcome the charging, graphite or metal coatings are needed, but the coating may change the fine surface structure of the imaged material [172].

Helium ion microscopy (HIM) is based on similar technology as SEM, but instead of using incident electrons, in HIM the sample surface is scanned by focused helium ion beam with energy of few tens of keV. The high yield of secondary electrons from the ion beam interaction with the sample atoms enable the use of low beam currents, typically less than 1 pA. The charging effects can be compensated by using an electron flood gun between the scans. The resolution of HIM is slightly better than in SEMs, ca. 0.5 nm [176].

Atomic force microscopy (AFM) is used to study the topography of the sample surfaces. In AFM a probe consisting of a cantilever and an oscillating nanometer-sized tip tracks the surface. The probe movement is translated into the surface topography map via the deflection of the laser beam from the cantilever to a position-sensitive photodetector.

The crystal structure of the samples was investigated by means of *X-ray diffractometry (XRD)*. XRD is based on the detection of X-rays scattering from parallel planes. The X-rays, typically Cu K_α with E_{photon}=8.047 keV, interfere constructively when the Bragg condition $n\lambda = 2d \sin\theta$, where n is an integer, and λ is the X-ray wavelength and d is the interatomic distance between the planes, is satisfied. Samples with crystalline structure have characteristic lattice parameters that can be detected and identified with XRD by probing the sample with the X-ray beam over a range of 2θ angles. If the studied sample is a very thin film, a *grazing-incidence XRD (GIXRD)* is preferred. GIXRD utilizes a small incidence angles and penetration depths, which enhances the sensitivity [172, 173].

4.2 Plasma diagnostics

There are several different methods for characterization of the plasma properties and species. For example, mass spectroscopy can be used to analyze the species extracted from the plasma and Langmuir probe measurements give information of the plasma parameters i. e. n_e and T_e. Optical diagnostics methods, such as emission and absorption spectroscopy, and laser induced fluorescence, can provide information about the concentrations of different species and their temperatures without perturbing the plasma [162]. In this work optical emission spectroscopy was used.

4.2.1 Optical emission spectroscopy

In PEALD optical emission spectroscopy (OES) can be used to non-invasively characterize the discharge properties by recording the light emitted from the plasma [177]. The electron-impact processes in the plasma cause excitation of the particles from the initial (q) to a higher level (p), from which they decay to another level (k) with the transition probability A_{pk}, resulting in a photon line emission. The wavelength of the emission is given by

$$\lambda = hc/\left(E_p - E_k\right) \ , \tag{27}$$

where h is the Planck constant, c is the speed of light and E_p and E_k are the energies of the higher p and lower k levels, respectively. The intensity of the emission line depends on the population density of the excited state $n(p)$ and the transition probability

$$I_{pk} = n(p)A_{pk} \ . \tag{28}$$

The spontaneous transition probability A_{pk} between the states p and k is proportional to the overlap of the wave functions and the transition moment. A_{pk}

also classifies the transitions to allowed and forbidden transitions. If the transition to the lower state is not allowed i.e. $A_{pk} = 0$, the state is called metastable. The metastable states have orders of magnitude longer lifetimes than the excited states from which transitions to the lower states are allowed i. e. $A_{pk} > 0$. The allowed transitions are defined by the wave functions and can be concluded from the quantum numbers of the energy levels[1] [178].

The structures of atoms can be presented with energy level diagrams. The transitions linked to the ground state are called resonant transitions and their high probability makes the corresponding radiation intense. The energy gap between the ground state and the excited states is commonly large, hence making the transitions emit in the ultraviolet (UV) or vacuum ultraviolet (VUV) range. Optical emission in the visible spectral range is typically originated from transitions between excited states. Figure 11 shows the energy level diagram of atomic oxygen and the most probable transitions.

As an example, the spectrum of PEALD O_2 plasma, with pressure in the order of few mbar, is typically dominated by the O emission lines at 777 nm and 854 nm. These lines originate from transitions $2p^3\ {}^3P \rightarrow 2p^3\ {}^3S$ and $2p^3\ {}^5P \rightarrow 2p^3\ {}^5S$ with $A_{pk} \approx 10^7$ s^{-1} (denoted as (b) and (a) in Fig. 11, respectively). The $2p^3\ {}^3S$ state has a lifetime of $\sim$2 ns [180], and the following spontaneous decay to the ground state corresponds to the emission line at 130 nm with transition probability of $A_{pk} \approx 10^8$ s^{-1}, and is the major contributor to the UV/VUV-irradiation in the O_2 plasma. Correspondingly to the decay of $2p^3\ {}^5S$ state, the transition probability is several orders of magnitude lower ($A_{pk} \approx 10^3$ s^{-1}), and hence it has a longer (radiative) lifetime of 200 µs [179, 180]. In comparison, the metastable O (^1D) state (at 1.97 eV) has a lifetime of 147 s [109], the transition probability being $A_{pk} \approx 10^{-5}$ s^{-1} [179].

For molecules the transitions are more complex, due to the orbital interaction, electron spin, and the vibrational and rotational motion of the molecule. Like in the case of transitions between atomic levels, the quantum numbers of the initial and final states define if the transition is allowed[2]. For example, the $O_2(a^1\Delta_g)$ state (at 0.98 eV) cannot decay into the ground state $O_2(X^3\Sigma_g^-)$ as the total spin of these states differ i. e. $\Delta S \neq 0$, which makes the $O_2(a^1\Delta_g)$ state metastable with a lifetime of 4400 s.

Instead of the energy level diagram, the structures of the (diatomic) molecules

---

[1] The quantum numbers of the atom are: main quantum number n, angular momentum l, and m, which describes the vector component of the angular momentum. For the allowed transitions Δn is unrestricted and $\Delta l = \pm 1$.

[2] In addition to the atomic quantum numbers the quantum numbers of molecule include the total spin S and angular momentum Λ of the molecule, parity of the state (+ or -), and symmetry (g or u). For the allowed transitions $g \leftrightarrow u$, $\Delta S = 0$, and $\Delta\Lambda = 0, \pm 1$.

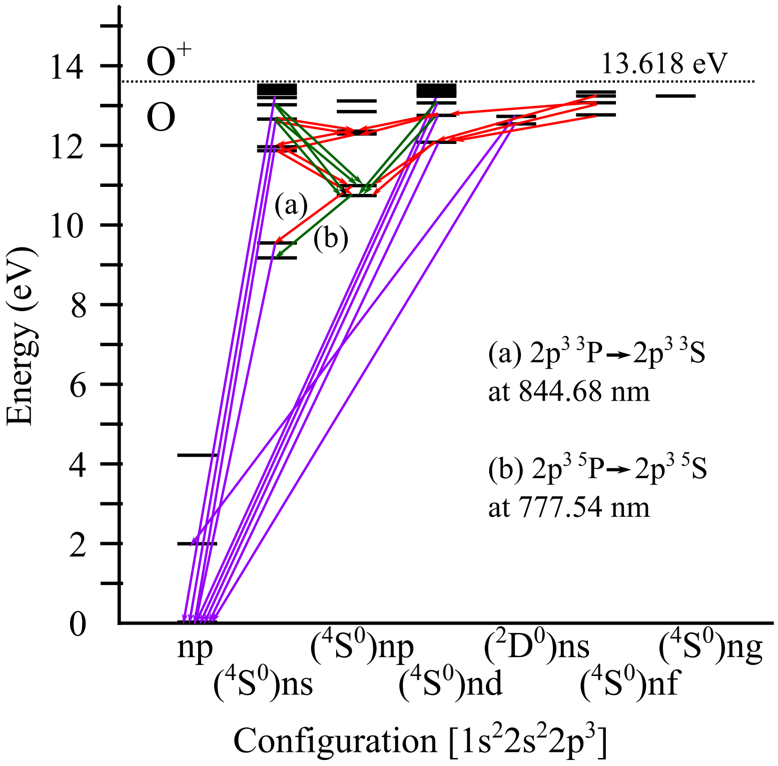

FIGURE 11 Energy level diagram of atomic oxygen with the most intense allowed optical transitions. The transitions in the UV, VIS, and IR-regions are denoted as purple, green, and red arrows, respectively. Horizontal axis denotes the electronic configuration of each level in addition to the $1s^2 2s^2 2p^3$ basis. The transitions (a) and (b) denote the two emission lines typically observed in the spectra of low-temperature O_2 plasmas. The energy levels and transitions are from NIST atomic spectra database [179].

are typically represented as potential energy curves, where the x-axis assigns the internuclear distance between the atoms of the molecule thus defining the energy levels. Each electronic state has vibrational levels (denoted with ν) and each vibrational level has rotational levels J.

The transitions follow the so called Frank-Condon principle, which assumes that the vibrational motion of the molecule is slow compared to the time-scale of the electronic transitions, and therefore the internuclear distance does not change in the excitation or decay processes. Thus the excitations and decays follow a vertical line, as shown in the examples of the selected observable transitions in Fig. 12. Based on the principle a change from one vibrational energy level to another is more probable if the wave functions of the vibrational levels overlap. The probability of the transitions are thus defined by their Frank-Condon factors [181].

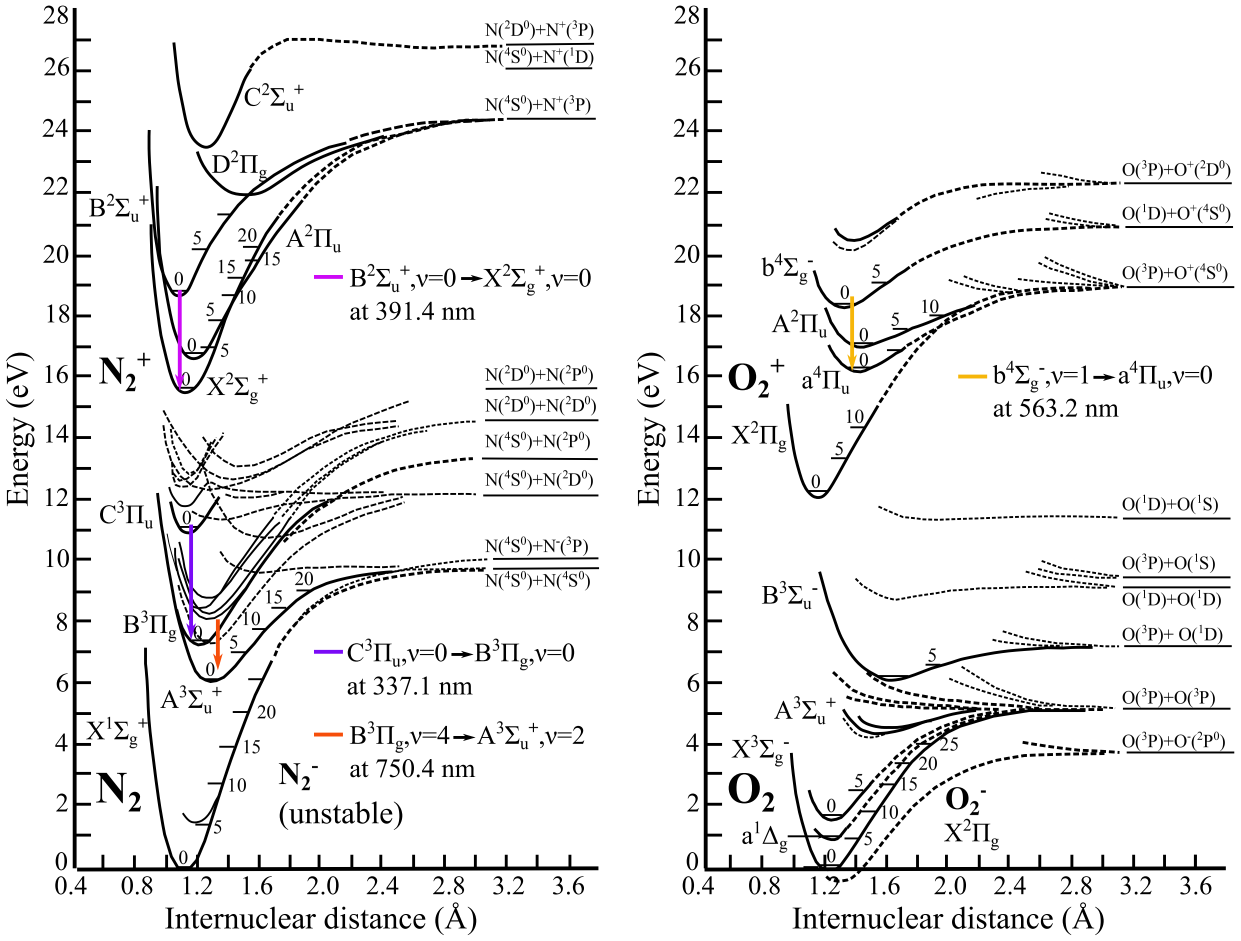

FIGURE 12 The potential energy curves for N_2, N_2^+ and O_2, O_2^+. The potential energy curves for N_2 and O_2 are adapted from Refs. [181] and [182], reprinted with permissions from AIP Publishing and Elsevier, respectively. Examples of transitions in the 1st and 2nd positive system of N_2 ($C^3\Pi_u \rightarrow B^3\Pi_g$ and $B^3\Pi_g \rightarrow A^3\Sigma_u^+$, respectively), N_2^+ 1st negative system ($B^2\Sigma_u^+ \rightarrow X^2\Sigma_g^+$) and O_2^+ 1st negative system ($b^4\Sigma_g^- \rightarrow a^4\Pi_u$) are denoted in the figures.

With OES it is possible to identify different species and processes in the plasma, based on the unique energies of each optical transition. However, in practice the technique is limited by the wavelength range and the resolution of the spectrometer. Figure 13 shows an example of the optical emission spectrum measured from an inductively coupled PEALD device with Ar/NH_3 mixture plasma with N_2 process gas background. From the emission of the excited atomic hydrogen and notable fraction of excited N_2 one can, for example, conclude a significant dissociation of the NH_3 molecules in the plasma during the PEALD operation. The OES gives also information useful for the PEALD process optimization, as the optical emission is sensitive to the changes in the plasma parameters, such as n_e and T_e. However, these parameters cannot be directly determined with OES, but can be deduced from the spectra by analyzing the probabilities of different processes as a function of the plasma parameters.

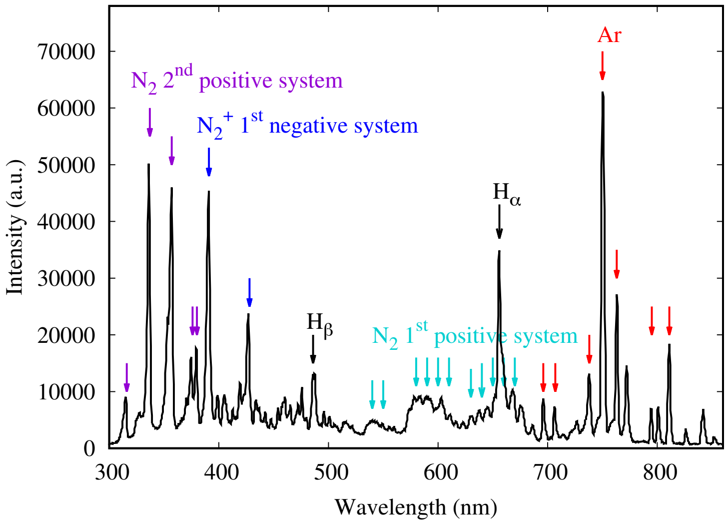

FIGURE 13 An example of plasma optical emission spectrum in the VIS-range. The spectrum is measured from a $Ar/NH_3/N_2$ plasma in a commercial inductively coupled PEALD device. The sources of most intense atomic emission lines and molecular bands are denoted in the figure.

4.2.2 Rate coefficient analysis

The relative probabilities of different electron impact processes can be assessed by comparing their reaction rates. The volumetric reaction rate R depends on the densities and velocities of the colliding particles, and the process cross section. As mentioned in the previous Chapter, processing plasmas are generally weakly ionized, which means that the dominant impact processes are electron–neutral collisions. For an electron–neutral collision R can be written as:

$$R = n_e n_n \int f_e(v)\, v\, \sigma(v)\, dv = n_e n_n \langle \sigma v \rangle \ , \tag{29}$$

where n_e and n_n are the densities of the electrons and neutrals in the plasma, respectively, $v = v_e$ is the electron velocity, $f_e(v)$ is the electron energy distribution function (EEDF) written in the terms of the electron velocity i. e. the electron velocity distribution function (EVDF) (see Section 3.2.2). $\sigma(v)$ is the process cross section, which is the measure of probability for the given process. It is assumed here that the neutrals are stationary ($v_\mathrm{e} >> v_\mathrm{n}$). The term $\langle \sigma v \rangle$ is the *rate coefficient*, that can be used to determine the relative importance of various electron–neutral collision processes.

When assuming the Maxwell-Boltzmann EVDF, the rate coefficient can be written using Eqs. (12) and (29):

$$\langle \sigma v \rangle = 4\pi \left(\frac{m_e}{2\pi k T_e} \right)^{3/2} \int v^3 \sigma(v) \exp\left(-\frac{m_e v^2}{2kT_e} \right) dv \ . \tag{30}$$

The rate coefficients for different electron impact processes can be solved numerically from equation (30) using cross sections (σv) reported in the literature. As an example, Fig. 14(left) shows the cross sections of the electron impact ionization of ground state $O_2(X^3\Sigma_g^-)$ ($e^- + O_2(\nu) \rightarrow {O_2}^+ + e^- + e^-$) from initial vibrational levels $\nu = 0$ and $\nu = 10$ to all possible vibrational levels of the final ${O_2}^+(X^2\Pi_g)$ ion [183]. The corresponding rate coefficients are presented in Fig. 14(right), which shows the contribution of the high-energy tail of the electron distribution to the ionization process rate even at low T_e.

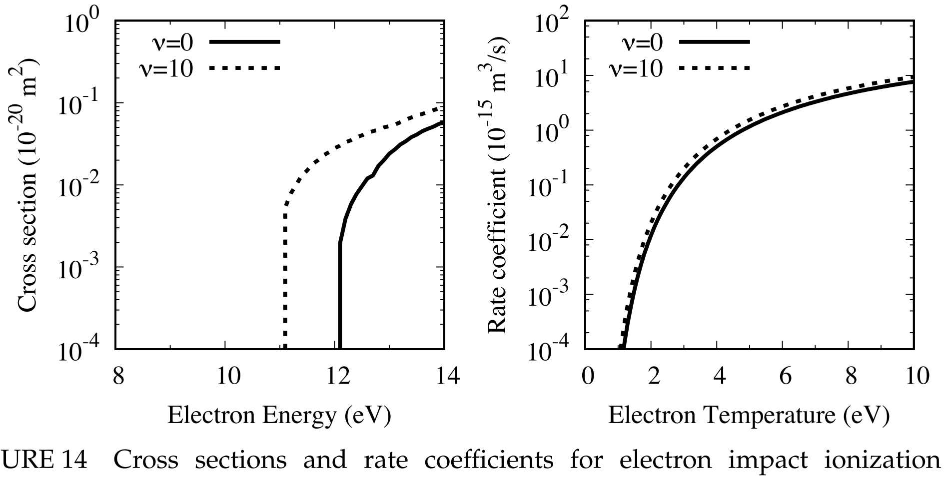

FIGURE 14 Cross sections and rate coefficients for electron impact ionization of $O_2(X^3\Sigma_g^-,\ \nu)$ from initial vibrational levels of $\nu = 0$ and $\nu = 10$.

5 LOW-TEMPERATURE ALD OF ZnO ON PMMA

5.1 ALD growth on polymers

In comparison to the traditional inorganic substrate materials, such as silicon and glass, polymer surfaces have distinctive characteristics which inflect the ALD processing. Many polymers lack functional surface groups such as $-OH$, which hampers the precursor adsorption during the fist ALD cycles. The polymer materials are also permeable to small molecules due to large interstitial space between the polymer chains, enabling the penetration of the ALD precursors to the sub-surface region of the polymer and even into the polymer bulk [43].

Additionally, the ALD reaction mechanisms between the precursor and the polymer surface can differ from reactions on inorganic substrates. For example, Parson et al. [184] introduced a mechanism for TMA reaction with poly(methyl methacrylate) (PMMA). According to their studies the Lewis-acidic TMA reacts with the Lewis-basic carbonyl groups on PMMA side-chains. This reaction leads to a degradation of the PMMA surface polymer chains and can further promote the precursor diffusion to the polymer sub-surface. Moreover, the precursor interaction with the polymer may not be self-limiting, which can lead to polymer/film mixed interface[1], depending on the polymer material, the ALD precursors, as well as the deposition conditions. The combination of these features can lead to a very dissimilar film growth compared to the inorganic substrate materials.

According to a generic model of ALD on polymers by Wilson et al. [187] the ALD film growth on the polymer substrate is initialized through the following steps:

---

[1] This feature is exploited in the ALD-derived method called sequential vapour infiltration, which can be used to modify properties of biomaterials and polymers as well as to produce organic–inorganic hybrids and porous structures by using polymer templates [185, 186].

1. Diffusion/penetration of the metal precursor into the sub-surface region of the polymer.
2. Nucleation of the ALD material clusters through the ALD precursor reactions.
3. The growth of the nucleation clusters and coalescence.
4. Continuous film growth on the clusters, preventing further precursor diffusion.
5. Linear ALD film growth.

The number of ALD cycles needed to complete each step depends on the type of the polymer substrate, the choice of the ALD material and precursors and the deposition temperature. The schematic illustration of the model is presented in Fig. 15.

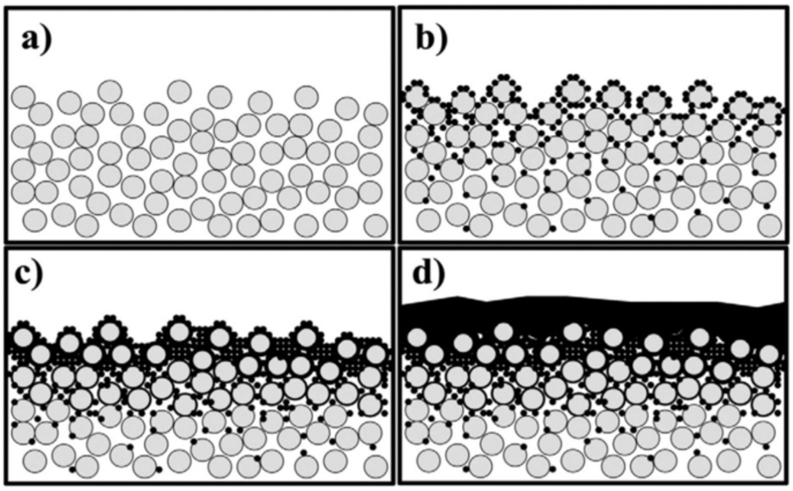

FIGURE 15 Model of ALD growth on polymer. (a) cross section of polymer surface represented by loosely packed circles, (b) nucleation clusters forming at the surface and sub-surface region, (c) coalescence of the clusters, and (d) formation of a dense film and linear growth. Reprinted with permission from Ref. [187], Copyright 2005 American Chemical Society.

5.2 ZnO deposition on PMMA

PMMA was chosen as a case study material as it is one of the most applicable of amorphous polymers. PMMA is a synthetic thermoplastic and is commonly used in optical and optoelectronic applications due to its transparency [188]. It is a biocompatible material and can therefore be used in medical applications such as tissue engineering and microfluidic lab-on-chip devices [57]. PMMA is also used in MEMS technology, and it is a common electron beam lithography resist in semiconductor industry [189].

To investigate the deposition of the ZnO films with DEZ–water ALD process on PMMA and the suitability of the process to different applications, two grades of PMMA were used as substrates: a commercial grade PMMA (also known as PLEXIGAS®), referred hereafter as 'bulk'(b) PMMA, and electronic-grade from PMMA e-beam resist, spin coated as smooth layers on silicon (Si) wafers and referred here as 'spin' (s). Uncoated Si wafers were used as references to compare the ZnO growth on inorganic and polymer substrates. PMMA has a glass transition temperature $T_g = 105$ °C, but due to its high thermal expansion coefficient (ca. 70 ppm K^{-1}) [57] the deposition temperature was limited to 35 °C.

The GPC of ZnO films on Si was determined with ellipsometry, being ca. 0.8 Å /cycle. Figure 16 shows the RBS-measured Zn areal density of the films on different substrates as a function of the applied ALD cycles. As shown, the amount of Zn is smaller on polymer substrates than on Si, and a notable difference between the PMMA substrates of different grades can be detected.

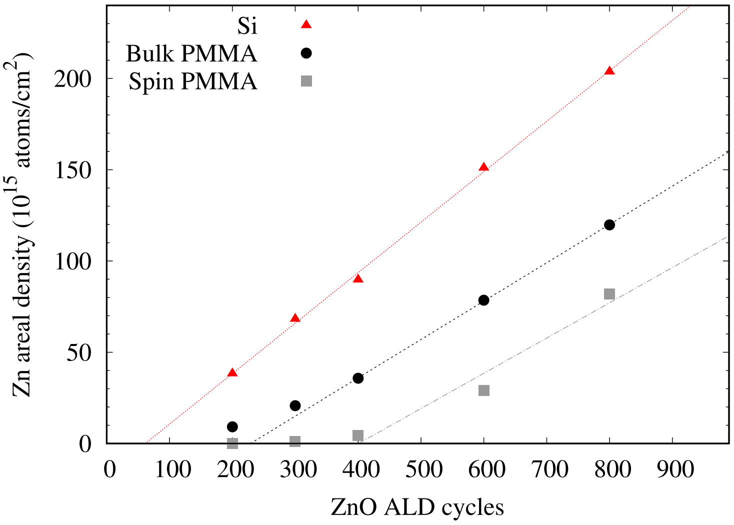

FIGURE 16 The growth of ZnO on Si, and bulk and spin-coated PMMA substrates as a function of ALD cycles. Determined from the RBS data. The lines are to guide the eye.

Based on the RBS results the ZnO growth is significantly delayed especially on the spin coated PMMA. The samples were imaged with AFM to investigate the reasons behind the slow growth initiation. Figures 17(b)-(f) shows the AFM images of the different ZnO growth stages on the spin coated PMMA substrates.

As seen in Fig. 17, a 200 ALD cycle ZnO deposition results in few visible nucleation clusters, seen as white spots. The amount of the clusters and their and size increase until full surface coverage after 400 ALD cycles is reached (Fig. 17). Thereafter the ZnO grain size remains approximately constant being ca. 30 nm.

The differences in the ZnO growth can also be seen by studying the original RBS spectra. Figure 18(a) shows the Zn peaks in the RBS spectra of the 300 ALD cycles of ZnO. The widening of the Zn peak of the film on the bulk PMMA substrate indicates the penetration of the Zn on the more porous polymer sub-surface. After 800 ALD cycles (Fig. 18(b)) the peak shape changes as a sign of linear surface-limited film growth.

The results show that the ZnO growth is strongly dependent on the choice of substrate material, and is influenced also by the grade of polymer substrates being identical in the chemical composition. On the spin-coated PMMA surface the initial nucleation steps take several hundred ALD cycles, and the growth is limited by the lack of reactive sites on the polymer surface. However, when deposited on the bulk PMMA material the ZnO growth seems to follow the generic model, according to which the nucleation clusters are formed in the polymer sub-surface via infiltration or diffusion to interstitial space between the polymer chains of the less dense commercial grade PMMA or by precursor penetration to the nanoscale features, where the adsorbed or kinetically trapped precursor molecule is able to further react and start the nucleation. The low deposition temperature did not lead to reduced film quality. The composition, determined with ToF-ERDA, was close to stoichiometric ZnO, with small amount of hydrogen and carbon impurities (6 ± 1 at. %, and < 0.5 at. %, respectively).

To study if the growth of ZnO on PMMA could be enhanced, intermediate layers of ALD Al_2O_3 were grown on PMMA prior to the ZnO deposition. The linear growth of Al_2O_3 with low-temperature TMA-water ALD process is observed to initiate on several polymers within the first tens of ALD cycles [48, 190]. The linear growth after ca. 20 ALD cycles was observed with both the bulk and spin coated PMMA, as shown in Fig. 19. The same trend of higher Al content on the bulk PMMA, as seen with the ZnO films, was also detected.

The addition of the intermediate Al_2O_3 layer had a significant impact on the ZnO growth. Figures 18(c) and 18(d) show the Zn RBS spectra of 200 ALD cycles of ZnO deposited on the Al_2O_3 layers. As seen in Fig. 18(c), the intermediate layer completely prevents the Zn penetration/infiltration on the bulk PMMA already after 20 ALD cycles of Al_2O_3. It also enables faster ZnO growth on the spin coated PMMA. In addition, it was observed that the ZnO film structure changes when the intermediate layer is applied. Figure 17(a) shows the AFM image of the 200 cycles of ZnO deposited on spin coated PMMA with 50 ALD cycle thick Al_2O_3 layer. The ZnO film structure on Al_2O_3 is smooth with small grain size, simi-

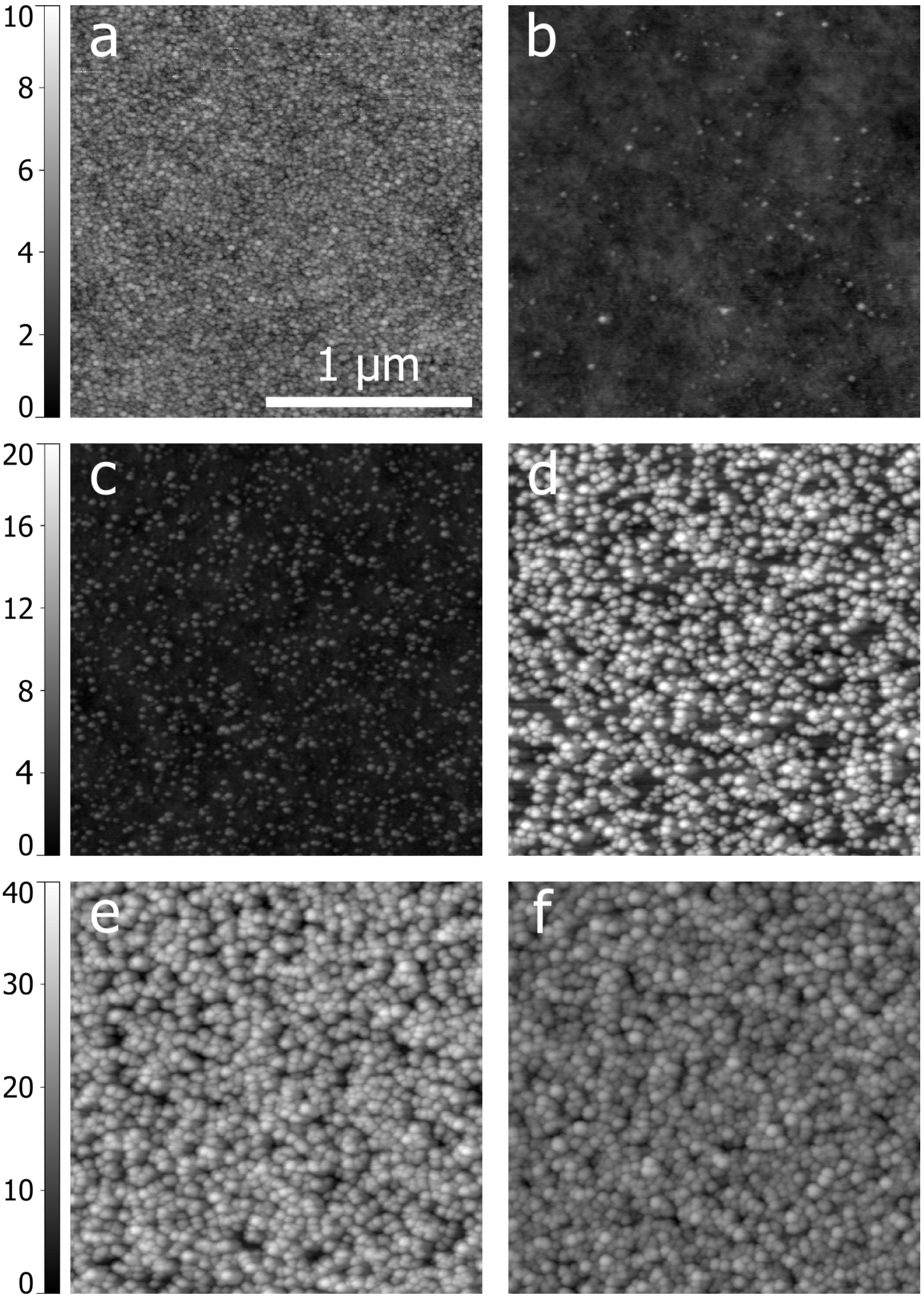

FIGURE 17 AFM images of ALD ZnO films deposited on spin-coated PMMA substrates. (a) 200 ALD cycles of ZnO on 50 ALD cycles Al_2O_3; (b) 200, (c) 300, (d) 400, (e) 600, and (e) 800 ALD ZnO cycles. Image area in each panel is 2 µm × 2 µm. Reprinted from PI with permission from the American Vacuum Society.

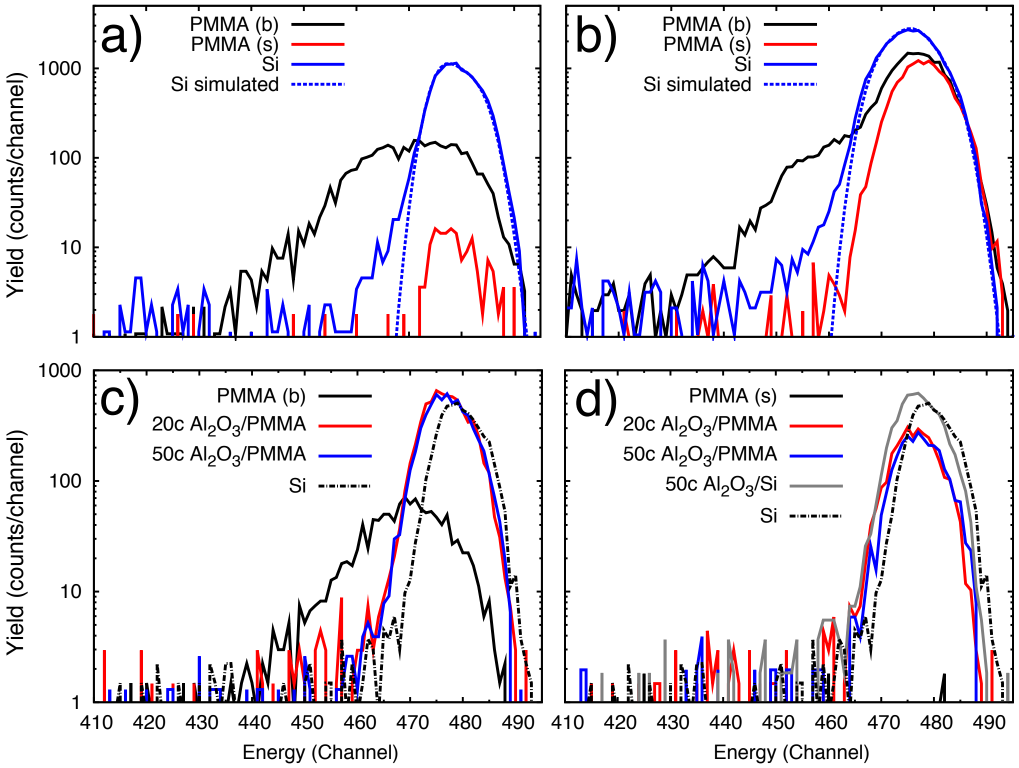

FIGURE 18 Zn peaks on the RBS spectra. (a) and (b) ZnO deposited directly on Si, bulk PMMA, and spin-coated PMMA with 300 ALD cycles in (a) and 800 ALD cycles in (b). In (c) 200 ALD ZnO cycles deposited on bulk PMMA without Al_2O_3 seed layer, and with seed layers of 20 and 50 ALD cycles of Al_2O_3. In (d) 200 ALD ZnO cycles deposited on spin-coated PMMA without and with Al_2O_3 seed layers. In (c) and (d) the Zn peaks from ZnO films on Si are shown as references. Reprinted from PI with permission from the American Vacuum Society.

larly to the ZnO films deposited on the Si substrates. The *c*-plane oriented (002) crystalline structure was also observed with XRD measurements of the films deposited on the Al_2O_3 layer after 800 ALD cycles of ZnO, while without the intermediate layer the same number of cycles results in more amorphous films.

The suitability of the deposited ZnO layers for polymer surface modification purposes was demonstrated by water contact angle measurements. Due to the semiconducting nature of the ZnO, its surface wettability can be controlled by exposure to UV light. It is assumed that the UV illumination generates electron-hole pairs leading to oxygen-deficient surface sites receptive to hydroxyl group adsorption. This phenomenon is reversible, and can be exploited in applications such as self-cleaning surfaces and liquid transport in microfluidic devices [108, 191, 192].

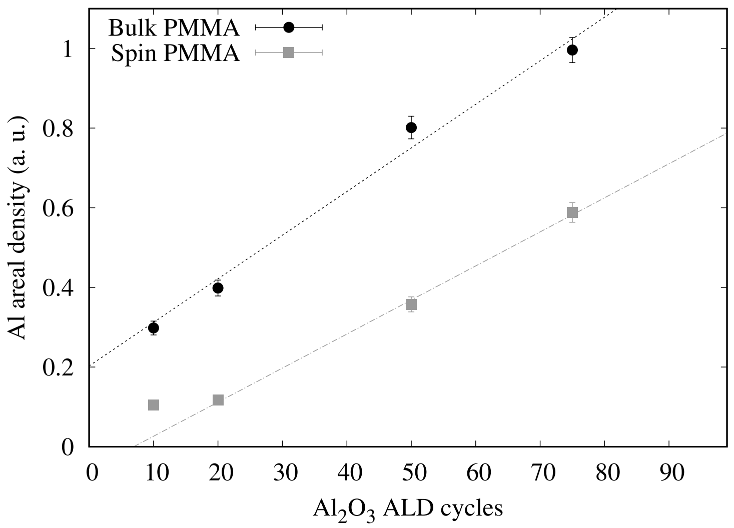

FIGURE 19 The growth of Al_2O_3 on the bulk and spin-coated PMMA substrates as a function of ALD cycles. Determined from the ToF-ERDA data. The lines are to guide the eye.

Figure 20 shows the measured water contact angle values of the ZnO films on different substrates after 15 min exposure to UV-light from a mercury lamp. It can be seen that the contact angle of the films on the PMMA substrates depend strongly on the film surface coverage, as well as the surface roughness. When the Al_2O_3 intermediate layer is applied, the illuminated ZnO surface is hydrophilic, the contact angle being somewhat independent on the substrate.

The UV-induced changes in the wettability of semiconducting oxides has been connected to the single- or polycrystalline structure of the films. For example with TiO_2 films the hydrophilicity cannot be induced on amorphous surfaces, but the crystalline anatase phase is needed [87]. In ALD, a temperature of 150 °C is typically considered as the lower limit for crystal agglomeration of TiO_2 [27], thus making the process incompatible with most of the polymers. ALD ZnO, however, shows the same characteristics when deposited at much lower temperatures, which makes it a potential candidate for polymer surface functionalization for applications relying on the UV-induced changes in the surface properties.

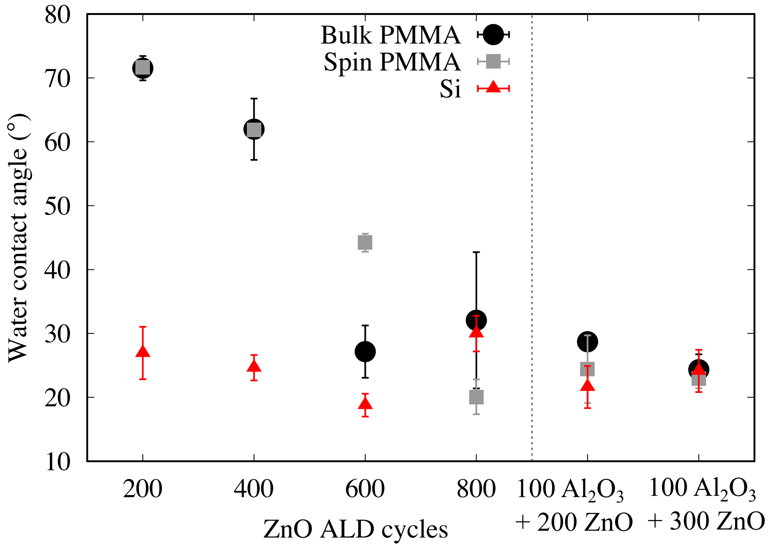

FIGURE 20 Water contact angles of UV-illuminated ZnO, deposited on bulk and spin coated PMMA, and on Si substrates. Two rightmost datasets represent the ZnO films deposited on the Al_2O_3 intermediate layers.

6 ROOM-TEMPERATURE PEALD

Reduction in the processing temperature is commonly mentioned as one of the most prominent advantages of the PEALD. Low deposition temperatures are especially appreciated in applications where temperature-sensitive substrates such as polymers and other organic materials are used. In some cases the reduction of the temperature down to room temperature can be highly beneficial, for example when the high thermal expansion coefficient of the polymers can degrade the film quality by inducing stress in the films. The use of plasma can overcome some of the issues of the ALD on polymers, such as the slow nucleation presented in Chapter 5. Room-temperature (RT) PEALD has been used successfully to grow films of several materials. For example metal oxides such as Al_2O_3 [137, 160, 193, 194], TiO_2 [193, 195–197], SiO_2 [193], Hf_2O [198] and ZrO_2 [199] have been deposited using O_2 or H_2O plasmas, and even the RT-PEALD of pure metal films (Ti, Ta [110], and Pt [200]) has been demonstrated.

As discussed in Chapter 3, the plasma properties and the flux of different plasma species depend strongly on the plasma source- and PEALD reactor configuration. This Chapter presents the growth and properties of the ZnO films deposited at room-temperature when different reactor configurations utilizing a remote inductively-coupled plasma (ICP) (see Section 3.4.2), and a remote and a direct capacitively-coupled plasma (CCP) (see Section 3.4.2) were used, and the applied plasma powers and O_2 plasma pulse lengths were varied. To investigate the viability of RT-PEALD to polymer materials, the depositions were also made on commercial poly(methyl methacrylate)(PMMA) and polycarbonate (PC) substrates, in addition to Si wafers.

6.1 RT-PEALD of ZnO

6.1.1 Film growth and properties

The GPC of the ZnO films deposited from DEZ and O_2 plasma using the remote ICP-PEALD, and the remote and direct CCP-PEALD are presented in Fig. 21. In all the cases the GPC values increase when longer plasma pulses are applied, which indicates incomplete surface saturation during the O_2 plasma pulses. In general, the growth is lowest when the ICP-PEALD is used, in which case the highest GPC value of ca. 0.73 Å was achieved when the plasma power of 1000 W was applied. Slightly higher GPC values were measured from the films deposited with remote CCP-PEALD, however, when the plasma power was increased to 200 W a significant non-uniformity over the deposition area was detected, especially with long plasma pulses. This effect was even more significant when the gas feed distribution was altered. In the alternative gas feed procedure the plasma was ignited with N_2 flow through the reactor showerhead, while O_2 was fed to the system via precursor inlet. The highest GPC values were measured from the films deposited using the direct CCP-PEALD configuration.

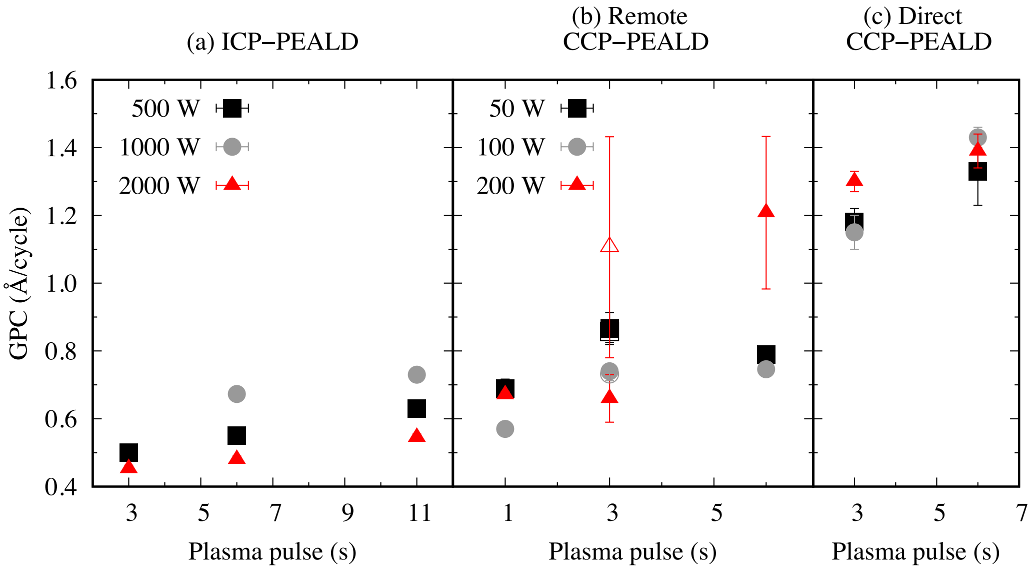

FIGURE 21 The GPC of the ZnO deposited on Si substrates using (a) ICP-PEALD, (b) remote CCP-PEALD, and (c) direct CCP-PEALD. Empty symbols in (b) denote the films deposited with alternative gas feed distribution. Error bars correspond to the variation in the measured film thickness over the deposition area. Adapted from PII.

The effect of the PEALD configuration to the composition of the films was measured by means of ToF-ERDA and ATR-FTIR. Table 2 shows the elemental composition of the selected ZnO films deposited with different reactor configurations[1]. RT-PEALD results in oxygen rich ZnO films, especially when remote plasma configurations were used. With direct plasma the O/Zn ratios are closer to stoichiometric and the contents of the light impurities are lower. High amounts of hydrogen and carbon, up to 26 and 12 %, respectively, were measured from the remote PEALD films deposited with low plasma powers and short plasma pulses. The high concentrations of H and C are commonly measured in the RT-PEALD films [160, 193, 201], as the reactivity of precursors is generally lower and the reactivity of the plasma species is not sufficient to compensate the absence of the thermally driven surface reactions .

TABLE 2 Elemental compositions of the RT-PEALD ZnO films deposited with different reactor configurations using long plasma pulses, measured using ToF-ERDA.

P (W)	t (s)	H (at.-%)	C (at.-%)	N (at.-%)	O (at.-%)	Zn (at.-%)	O/Zn(at.-%)
a) Remote ICP-PEALD							
500	11	16 ± 1	9 ± 0.5	0.7 ± 0.1	51 ± 2	22 ± 2	2.3 ± 0.4
1000[†]	11	16 ± 1	8 ± 0.5	0.3 ± 0.05	51 ± 2	24 ± 2	2.1 ± 0.2
2000	11	13 ± 1	6 ± 0.5	0.2 ± 0.05	53 ± 2	27 ± 2	2.0 ± 0.2
b) Remote CCP-PEALD							
50	6	15 ± 1	6 ± 0.5	1 ± 0.2	48 ± 2	29 ± 2	1.7 ± 0.2
100	6	15 ± 1	6 ± 0.5	2 ± 0.2	48 ± 2	30 ± 2	1.6 ± 0.2
200	6	6 ± 0.5	2 ± 0.2	1 ± 0.2	51 ± 2	41 ± 2	1.2 ± 0.2
b) Direct CCP-PEALD							
50	6	8 ± 0.5	2 ± 0.2	0.5 ± 0.1	51 ± 2	38 ± 2	1.5 ± 0.2
100	6	5 ± 10.5	0.7 ± 0.1	0.4 ± 0.1	52 ± 2	42 ± 2	1.2 ± 0.2
200	6	5 ± 0.5	0.5 ± 0.1	0.5 ± 0.1	52 ± 2	42 ± 2	1.2 ± 0.2

[†] This sample also contained a trace amount of fluorine (0.1 ± 0.05 at.-%).

Based on the ATR-FTIR measurements, the PEALD of ZnO from DEZ and O_2 plasma corresponds to the combustion-like reaction mechanism discussed in Section 3.4.1. The presence of the OH groups can be seen in Fig. 22 as broad absorption appearing at the range 3000–3600 cm^{-1}, while the contribution of the carbonate C=O, COO$^-$, and C−O is associated to the absorbance in the range 1650–1300 cm^{-1}. Though the absolute absorbance is dependent on IR-activity of the specific bond, as well as the film thickness, the relative intensities imply that in the films deposited with ICP-PEALD the residues of the carbonate species dominate over OH, while the opposite prevails in the remote CCP-PEALD films. This assumption is also in accordance with the measured atomic concentrations. The nitrogen incorporation in both remote and direct CCP-PEALD films is seen

---

[1] In Table 2 the compositions of the films deposited with longest plasma pulse lengths with each applied power are presented, the more comprehensive tables can be found in PII.

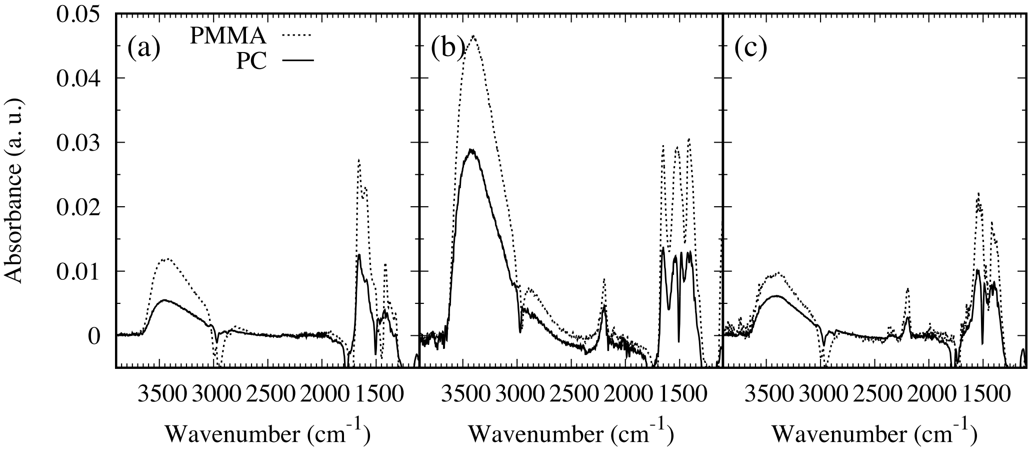

FIGURE 22 ATR-FTIR absorption spectra of the ZnO films on PC (solid lines) and PMMA (dashed lines) after substrate signal subtraction. Films deposited using (a) ICP-PEALD (500 W, 6 s), (b) remote CCP-PEALD (50 W, 3 s), and (c) direct CCP-PEALD (50 W, 3 s).

as a sharp peak at 2200 cm^{-1}, attributed to nitrile C≡N bond, which indicates generation of reactive N species during the CCP-PEALD operation.

Figure 23 shows the XRD patterns of the ZnO films. The films deposited with ICP-PEALD are mostly amorphous, with only a slight indication of a polycrystalline structure seen in the film deposited with highest plasma power. Similarly amorphous are the films deposited with remote CCP-PEALD, with the exception of the film deposited with 200 W, exhibiting hexagonal wurtzite structure corresponding to the direct CCP-PEALD grown films. These show strong *a*- and *c*-plane orientation, corresponding to the high intensity (100) and (002) peaks, respectively. In Fig. 23(c) the peak shift towards smaller angles indicates an increase in the lattice constant, which may imply the change in the residual stress of the films when higher plasma power is applied. It has been reported by Samal et al. [146], that the increase in the plasma power in direct plasma depositions leads to lower compressive stress in the films due to the disordering of the lattice structure under the ion bombardment.

6.1.2 Effect of PEALD reactor configuration

In the RT-PEALD the effect of the plasma species to the film growth and properties is substantial, as no additional thermal energy is provided to the surface reactions. As shown, the growth and characteristics of the ZnO depend on the used PEALD reactor configuration. The observed differences in the ZnO films highlight the role of energetic ions. According to the results, good quality films

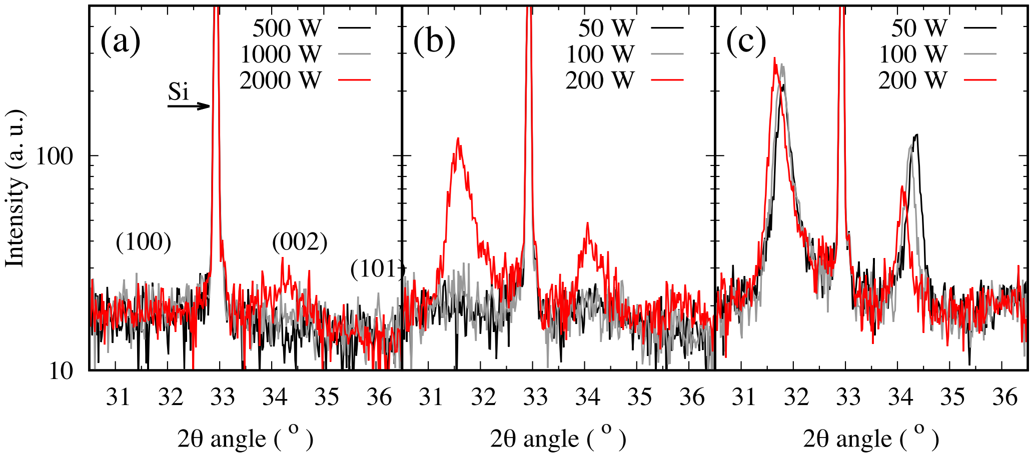

FIGURE 23 XRD patterns of the ZnO films deposited with (a) ICP-PEALD with 11 s plasma pulses, (b) remote CCP-PEALD, and (c) direct CCP-PEALD, both with 6 s plasma pulses.

with polycrystalline structure were accessible only by means of direct plasma exposure[2]. The GPC values, high impurity content and the amorphous structure of the films deposited by using remote plasma can all be considered to be caused by the insufficient energy deposition, that cannot be fully compensated by increasing the plasma power nor the plasma pulse length.

Due to high operation pressure (5 mbar) in the remote ICP-PEALD the ion flux to the substrate can be considered to be negligible, and hence the film growth is governed solely by the radical species, including the ground state O and the atomic and molecular metastables. The elimination of the ions in the remote ICP-PEALD system is supported by the observations of the remote CCP-PEALD deposited films. Here only a 1 cm of gas between the grid and the substrate is enough to reduce the ion flux and energy significantly, if not completely. However, the slightly improved composition is contributed, if not by ions, the higher flux of reactive plasma radicals to the substrate.

The effect of the distance x between the active plasma and the substrate to the number of specific species arriving at the substrate (N_s) can be approximated as:

$$N_s = N_0 e^{-(\Sigma n_j \sigma_j)x} , \tag{31}$$

---

[2] Though no significant increase in the substrate temperature was observed during the PEALD processing, the effect of heating of the surfaces by the direct plasma exposure cannot be excluded. The temporary increase in the temperature during the plasma pulses can contribute to the surface reactions and thus partially explain the observed differences between the remote and direct plasma deposited films. However, as will be shown in Section 6.2, the increase in temperature cannot be considered as the main contributor to the film growth as the plasma-induced changes in the substrates cannot be explained solely by the local temperature increase.

where N_0 is the initial amount of these species created in the plasma and it is proportional to the plasma density n_e and the production process rate coefficient $\langle \sigma v \rangle$. The amount of species consumed by processes such as de-excitation is described with the exponential function consisting of the density of the colliding species nj and the cross sections σ_j of the processes. For both the ICP and CCP the electron temperature T_e is similar and in the order of 1–3 eV, which makes the N_0 to be dependent only on the plasma density, which can be estimated to be an order of magnitude higher for the ICP than for the CCP. As the majority of species interactions in this case take place in the neutral gas volume $n_{j,\mathrm{ICP}}$ can be considered to be equal to $n_{j,\mathrm{CCP}}$ at the same pressure. Due to the exponential nature of the species consumption, the distance x becomes the dominant factor. Thus, in this case the long distance ($\sim$50 cm) between the ICP source and the substrate results in lower fluence of energetic species to the substrate despite the higher initial plasma density.

In the case of remote CCP-PEALD it was observed that high applied power resulted in non-uniform film growth and properties deviating from the other remote PEALD films. This discrepancy can be explained by a presence of a ′parasitic′ plasma component between the grid and the substrate, which is a result of a mode transition in the capacitively-coupled discharge. The mode transition phenomenon will be discussed in detail in Chapter 7.

6.2 PEALD on polymers

Like the thermal ALD, also PEALD is -in principle- applicable to polymer substrates. As the effects of temperature-dependent properties of the polymers can be avoided in room-temperature processing, RT-PEALD films can be considered as potential candidates for barrier applications and other surface modification purposes [44, 202]. However, besides the beneficial plasma species, in PEALD the substrate material will be exposed also to UV radiation emitted by the plasma, as well as to ion bombardment in the cases where ionizing plasma is present at the substrate.

To investigate the viability of the remote and direct plasma PEALD processing on polymer substrates, the films discussed above were deposited also on PMMA and PC substrates. It was observed, that unlike in thermal ALD, in PEALD the film growth is not delayed on polymers. This can be considered to be a consequence of the polymer surface activation by the plasma species creating additional $-\mathrm{OH}$ surface groups enabling more efficient precursor adsorption. Additionally, no signs of precursor infiltration to the polymer subsurface was observed in the measured RBS spectra of the films, which indicates that the nucleation coalescence of the ZnO takes place already within the first cycles due to the high reactivity of the oxygen species.

Figures 24 and 25 show AFM images of the ZnO films deposited on the PMMA and PC substrates, respectively. The film surfaces on polymers are similar to films on Si substrates (see PII) and no indication of significant polymer degradation can be seen in the cases of remote PEALD, both with ICP and CCP configurations. However, in the case of direct CCP-PEALD an increase in the surface roughness of PMMA can be observed (Fig. 24(d)).

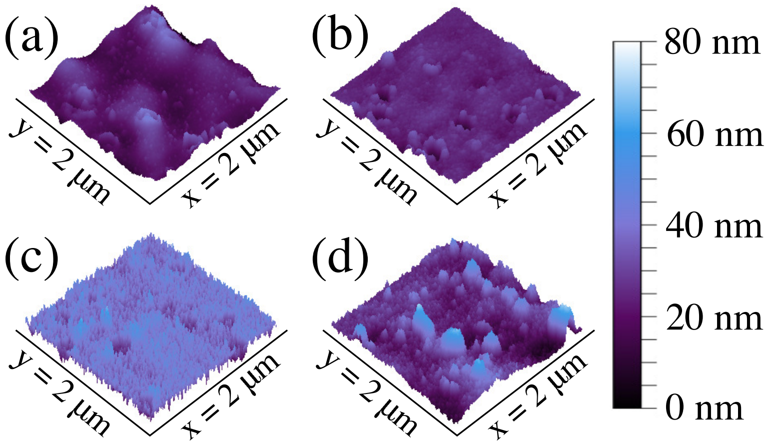

FIGURE 24 AFM images of the ZnO films on the PMMA substrate, (a) uncoated PMMA reference, ZnO deposited with (b) ICP-PEALD (1000 W, 11 s), (c) remote CCP-PEALD (100 W, 6 s), and (d) direct CCP-PEALD (100 W, 6 s). Reprinted from PII.

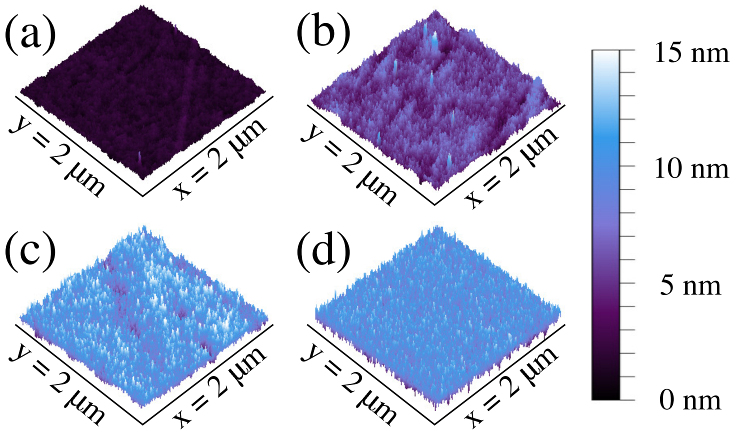

FIGURE 25 AFM images of the ZnO films on the PC substrate, (a) uncoated PMMA reference, ZnO deposited with (b) ICP-PEALD (1000 W, 11 s), (c) remote CCP-PEALD (100 W, 6 s), and (d) direct CCP-PEALD (100 W, 6 s). Reprinted from PII.

As no surface changes were observed with remote PEALD, the results indicate that the surface damage is mainly attributed to the ion bombardment during the deposition, while the polymer photodegradation under the plasma UV irradiation cannot be concluded. To further study the effect of both the damaging mechanism, the polymer substrates were exposed to the direct CCP plasma conditions without film deposition. To isolate the effect of plasma UV, a MgF_2 window (cut-off wavelength ca. 113 nm) was used.

The effect of the direct plasma to the PMMA surface was presented in Fig. 5 in Section 3.4.1 as an example of significant plasma-induced damage. It was observed that the RMS surface roughness increased drastically from initial 5 nm to 35 nm after (pulsed) 15 min plasma exposure. Less severe changes were observed on PC, where the surface roughness increased from the initial 0.5 nm to ca. 1.3 nm after similar treatment (Fig. 26(b)). However, no surface changes were detected in the samples exposed to the UV irradiation. The possibility of the photochemical degradation was also studied by measuring the UV-irradiated samples with ATR-FTIR.

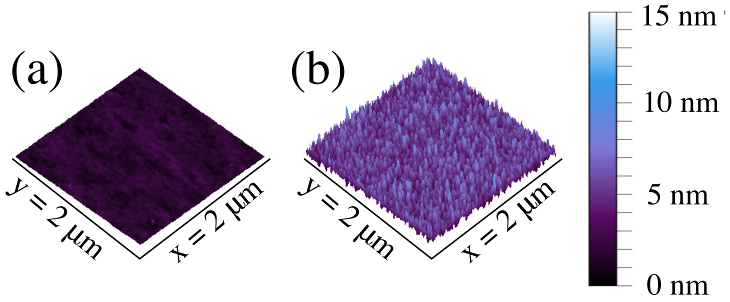

FIGURE 26 AFM images of the PC surfaces after 15 min exposure to (a) UV irradiation of the O_2 plasma through MgF_2 window, and (b) direct plasma. Reprinted from PII.

The photodegradation mechanisms in PMMA are related to the chain scission of the (methyl and ester) side groups [203, 204], which have dissociation-energies ranging from 3.4 eV for $C-CH_3$ and 4.4 eV for $O-C(=O)$ to 8.4 eV for the $C=O$ [205, 206], thus being in the order of the energy of the plasma ions at the substrate as well as the energetic plasma UV photons. Therefore, the degradation should be visible in the infrared absorption spectrum as a reduced absorbance in the corresponding regions, at ca. 3000–2900 cm^{-1} for the CH_3 groups and 1750–1100 cm^{-1} for the different $C=O$ and $C-O$ containing groups [152]. Based on the decreased absorbance, presented in in Fig. 27(left), the above-mentioned degradation of the PMMA under UV irradiation takes place. Instead in the PC the similar decrease in the absorbance was not observed (Fig: 27(right)), which indicates that the PC is more resilient also to the UV irradiation under PEALD conditions. These results

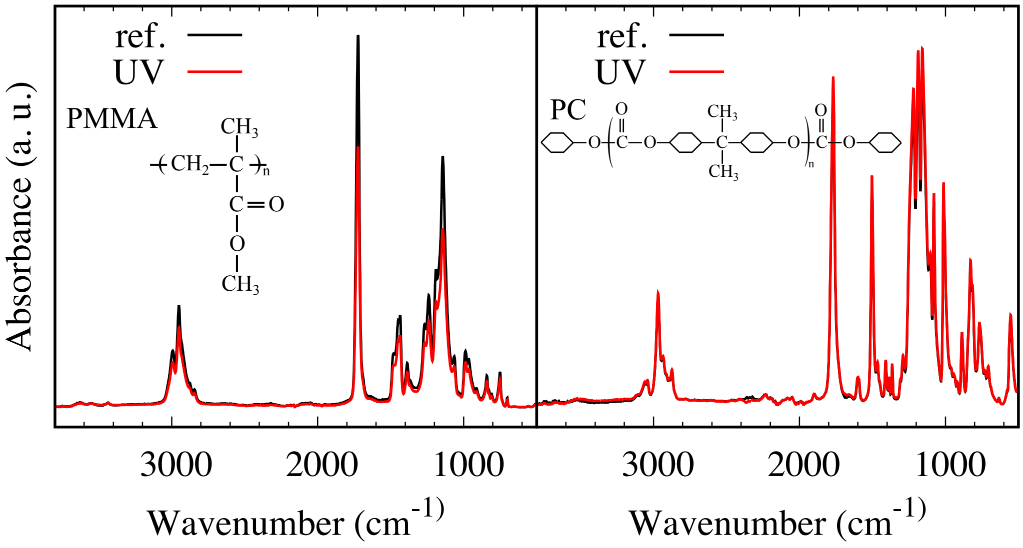

FIGURE 27 Infrared absorption spectra of the PMMA (left) and PC (right) before and after 15 min exposure to the plasma UV irradiation

are in accordance with reports on the plasma-induced effects of the PMMA and PC [207–210].

Though in PEALD the growing film will protect the substrate from further plasma damage after a certain thickness, the ion bombardment and UV irradiation may still cause substrate surface degradation during the deposition. This needs to be taken into account when the deposition method is chosen. It can be concluded that the PEALD is a viable method for ZnO thin film deposition at room-temperature, but the impurity-free polycrystalline films were produced only with direct plasma, which -on the other hand- was shown to be detrimental for the polymer substrates, the severeness of the degradation being dependent on the polymer composition.

7 PLASMA MODE TRANSITIONS IN PEALD

This chapter presents the features of the plasma modes and transitions between them. Mode transitions are fundamental characteristics of most discharges within a wide parameter range. First, the mode transitions in the capacitively-coupled plasmas are discussed, with the focus on the α–γ transition. The effect of the plasma modes to the PEALD with remote CCP configuration are presented together with the results published in PIII. To emphasize the universal nature of the mode transitions, another section is dedicated to the E–H transition in the inductively-coupled plasmas under typical PEALD processing conditions, with some preliminary unpublished data.

7.1 Capacitively-coupled discharges

7.1.1 α and γ plasma modes

The RF capacitive discharge can exist in several different modes. For example, at low pressures the stochastic heating mode prevails, i. e. the electrons in the plasma bulk gain energy from the alternating electric field between the electrodes [211]. Increase in the pressure causes a transition into a regime where the ohmic (collisional) heating sustains the plasma [212]. Power is dissipated via Ohmic heating in the plasma bulk whereas the electrons acquire energy in the oscillations of the near-electrode sheath boundary [213]. This mode is typically called the α mode or the low-current mode.

Transition from the α mode to the γ mode can be induced by increasing the RF voltage. The specific onset of the transition is determined by the pressure and composition of the plasma gas, the driving frequency, and the interelectrode distance. The transition to the γ mode is preceded by a drastic reduction of the sheath thickness or, at higher pressures, even a sheath breakdown [214–216]. The sheath breakdown enables secondary electron emission from the electrode surfaces by primary electron, ion, photon and metastable neutral bombardment [217]. These secondary electrons, having energies up to tens of eV, sustain the γ mode discharge by creating ionization cascades in the sheath region.

The α –γ transition has been reported for several plasmas with different composition at pressures from 10^{-2} mbar up to atmospheric pressure [215, 218–220]. A distinctive feature of the γ mode discharge sustained between planar electrodes is the contraction of the plasma column. Studies have shown that the spatial distribution of the plasma changes during the α –γ transition [214, 219, 220]. In the γ mode the plasma volume contracts and the bright sheath regions cover the electrodes only partially. This contraction is also accompanied by up to orders of magnitude surge in the power- and current densities, and hence the γ mode is also called as a high current mode.

In addition to α and γ modes, also a so called δ mode has been observed in molecular gases. This mode can serve as an intermediate transition mode between the α and γ modes in plasmas, where the dissociation products of the plasma gas possess lower ionization potential than the initial molecules [221, 222].

7.1.2 Plasma mode characterization

The plasma mode investigations and the thin film depositions were carrier out in a commercial PEALD reactor (see Fig. 7 in Section 3.4.2) equipped with capacitively coupled plasma generator using a 13.56 MHz power source. The system was operated in a remote configuration with a grid (aperture diameter 1.5 mm, spacing 2.0 mm, transparency ca. 50 %) positioned 10 mm above the deposition surface. The plasma gas composition was typical for the PEALD processing of metal oxide films, consisting of O_2 flow during the plasma pulses and the process background N_2, that was used to maintain the reactor pressure at ca. 4.5 mbar. For the OES measurements the optical fiber was positioned to view the plasma perpendicularly through the powered electrode.

The α mode was primarily observed with low RF power of 50–150 W, while the γ mode began to dominate when the applied power was increased above 200 W. Adjusting the capacitors of the matching circuit (see Section 3.4.2) enabled choosing between the α and γ modes at powers $\geq$150 W. When the automatic tune of the capacitors was used, a hysteresis effect was observed i. e. once the plasma was ignited in the γ mode with the higher applied power, it remained in the same mode also when the power was reduced below the typical observed onset of the α–γ transition.

The differences between the modes are clearly visible in the optical emission spectra. Figure 28 shows the normalized spectra recorded from the α and γ mode discharge. In the α mode the spectrum is dominated by the $2p^3\ ^5P \rightarrow 2p^3\ ^5S$ and $2p^3\ ^3P \rightarrow 2p^3\ ^5S$ transitions of atomic oxygen at 777 nm and 845 nm, respectively, whereas in the γ mode the specrum is dominated by the optical emission of the electronically excited N_2 molecules. Besides the changes in the species occupying the OES spectra, also the total intensity of the γ mode discharge was significantly higher than that of α mode.

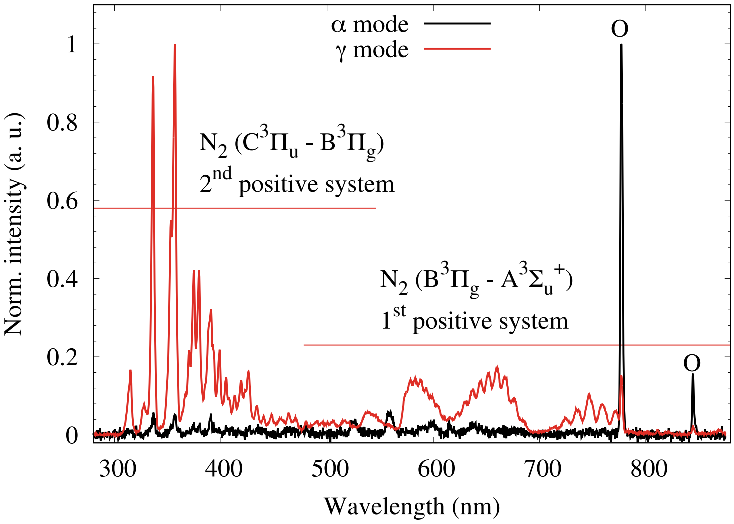

FIGURE 28 The normalized optical emission spectra of the O_2–N_2 in the α and γ modes. The transitions corresponding the most intense atomic lines of O and molecular bands of N_2 are labeled. Adapted from PIII with permission from IOP Publishing.

The changes in the OES spectra were also accompanied by a significant increase in the measured self-bias voltage, shown in Fig. 29, that builds up to compensate the different mobilities of the negative and positive charge carriers i. e. electrons and negative ions, and positive ions, collected by the powered electrode over each RF period half-cycle. Like the increase in the total optical intensity, the increase in the self-bias can also imply a surge in the plasma density n_e or an increase in T_e. However, in the case of electronegative discharge this cannot be directly concluded. A difference in the fraction of the negative O^- ions in the two modes can also cause the detected changes in the bias-voltage values, as the mobility of the negative ions is less than the mobility of the electrons.

It is noteworthy to mention that the mode transition could only be detected in the remote plasma configuration i. e. with the grid, as seen in the example spectra in Fig. 30. In the direct plasma setup the discharge transition to the γ mode

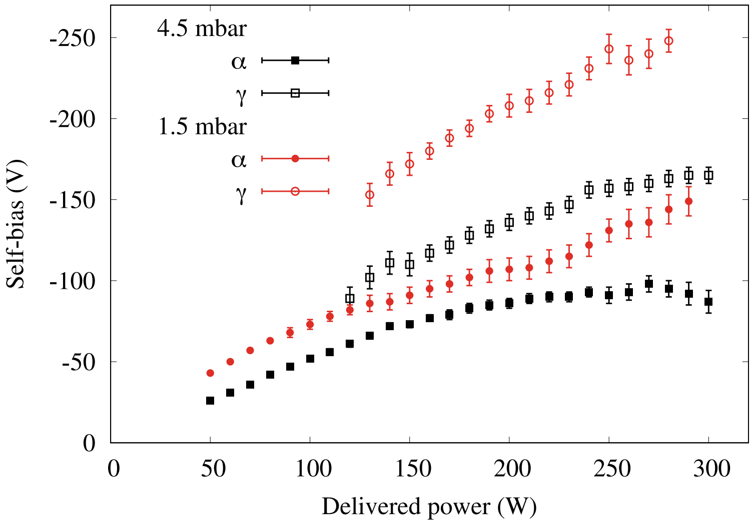

FIGURE 29 The self-bias voltage of the powered electrode as a function of the applied power with the α and γ mode plasmas at pressures of 1.5 and 4.5 mbar. Error bars correspond to pulso-to-pulse variation. Adapted from PIII with permission from IOP Publishing.

could not be triggered within the available power range under typical deposition conditions, despite the matching network tuning. A plausible explanation for the absence of the γ mode discharge are the surface properties of the Si substrate[1], that did not allow generation of the sufficient secondary electron yield required for the γ mode discharge development at the grounded electrode.

To understand the plasma processes behind the observed differences in the OES spectra, rate coefficient analysis was used to estimate how the plasma parameters, namely T_e changes in the mode transition. For the α mode the dissociation processes of O_2 were compared, as the spectrum was dominated by transitions from high energy levels of O. As presented in the Section 3.3, the two major dissociation processes are the direct electron impact dissociation and the dissociative electron attachment, referred hereafter as EID and DEA, respectively. As seen in the Fig. 31, the DEA process dominates over the EID.

To estimate the magnitude of the rate coefficient, the vibrational excitation of the initial O_2 molecule was also taken into account. When the rate coefficients of the resonant vibrational excitation were compared to the DEA process from the corresponding vibrational level v, it could be estimated that the O_2 vibrational levels up to $v = 10$ are heavily populated. When the vibrational excitation is taken into account it can be seen in the Fig. 31, that at low T_e the difference

---

[1] To mimic the actual deposition conditions, all the plasma mode studies were performed with a Si wafer placed on the sample stage.

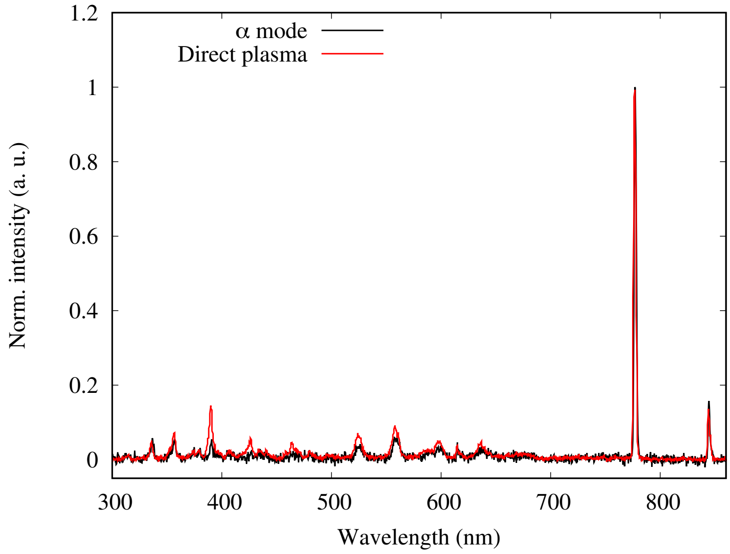

FIGURE 30 The normalized optical emission spectra of the remote α mode plasma and direct plasma with delivered power of 150 W.

between the rate coefficients of the DEA and EID can be almost two orders of magnitude.

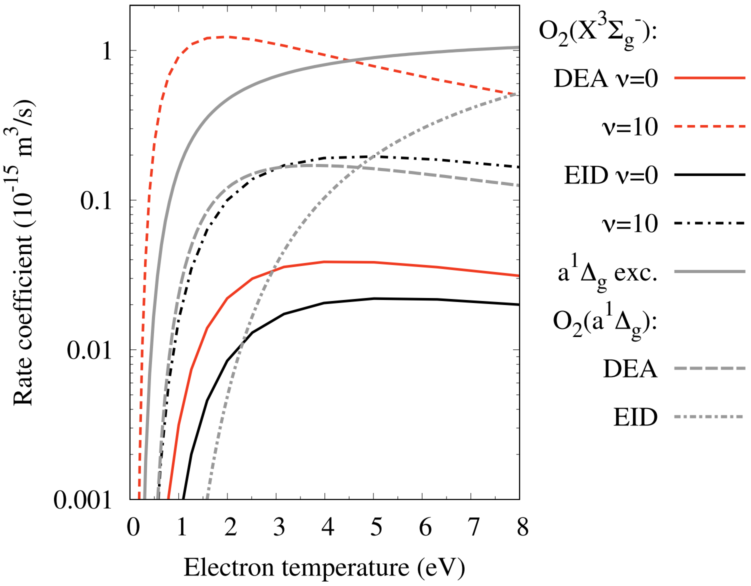

FIGURE 31 Rate coefficients for DEA and EID of $O_2(X^3\Sigma_g^-, \nu)$ with ν=0, 5, and 10, the electron-impact excitation of $O_2(X^3\Sigma_g^-)$ to $O_2(a^1\Sigma\Delta_g)$ state and the DEA and EID from the $O_2(a^1\Sigma\Delta_g)$ state. Adapted from PIII with permission from IOP Publishing.

Next, the rate coefficients of the O_2 DEA were compared to the rate coefficients of the electronic excitation of the N_2 molecules. The observed 1st and 2nd positive systems correspond to the transitions from $N_2(B^3\Pi_g)$ and $N_2(C^3\Pi_u)$ states (See Fig. 12). Hence, the rate coefficients were calculated from the cross sections to the electron impact excitation processes $e^- + N_2(X^1\Sigma_g^+) \rightarrow N_2(B^3\Pi_g) + e^-$ and $e^- + N_2(X^1\Sigma_g^+) \rightarrow N_2(C^3\Pi_u) + e^-$ [223]. As shown in Fig. 32 the DEA from high vibrational levels dominates over the N_2 excitations at low electron temperatures. In order to obtain the spectrum observed in the γ mode it can thus be concluded that the plasma must contain a significant fraction of high-energy electrons i.e. the effective temperature T_{eff} increases.

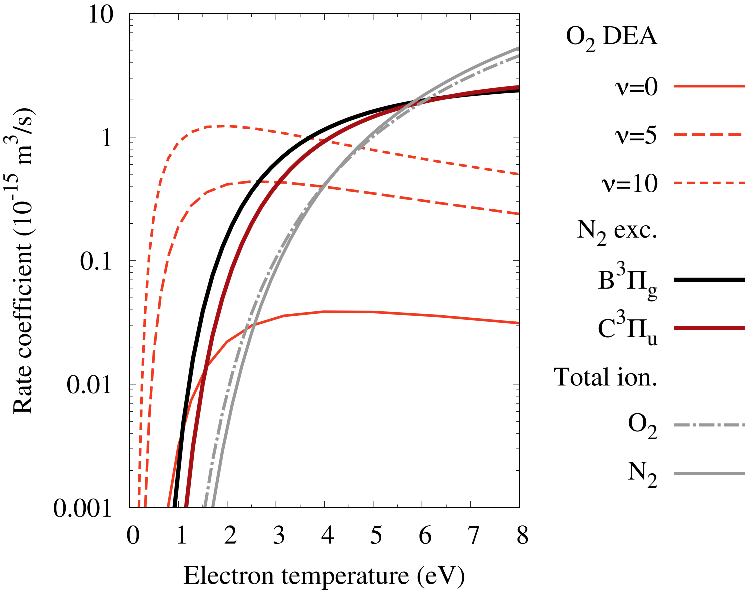

FIGURE 32 Rate coefficients for O_2 DEA, N_2 excitation to $B^3\Pi_g$ and $C^3\Pi_u$ states, and total ionization of O_2 and N_2. Adapted from PIII with permission from IOP Publishing.

These results are in accordance with reports of capacitive discharges in α and γ modes. The drastic increase in the overall emission intensity accompanying the α–γ transition has been reported also by Moon et al. [214, 224] who also showed that the sheath region is the source of the bright emission.

The rate coefficient analysis shows that the line-integrated T_e increases in the γ mode. This is presumably due to the change in the EEDF towards a bi-Maxwellian form, consisting of a distribution of low-energy electrons created in the ionization cascades and an enhanced tail of hot (secondary) electrons in the plasma sheath. The bi-Maxwellian EEDF of the γ mode in capacitive discharge with molecular plasma gases has been measured directly, for example by Abdel-Fattah et al. [225].

7.1.3 Thin film growth

To investigate how the detected α and γ modes affect the PEALD film growth, ZnO and TiO_2 films were deposited using DEZ and TiO_2 precursors, respectively. Low deposition temperatures, 50 °C for ZnO and 150 °C for TiO_2, were chosen to enhance the effects of the plasma over the thermally driven surface reactions. Three films of both materials were deposited using different plasma conditions: with α mode, with γ mode, and with direct plasma, and each deposition consisted of 1000 PEALD cycles. The most representative examples of the plasma-mode induced effects of the deposited films are collected into the following sections, while the more thorough analysis is presented in PIII.

ZnO

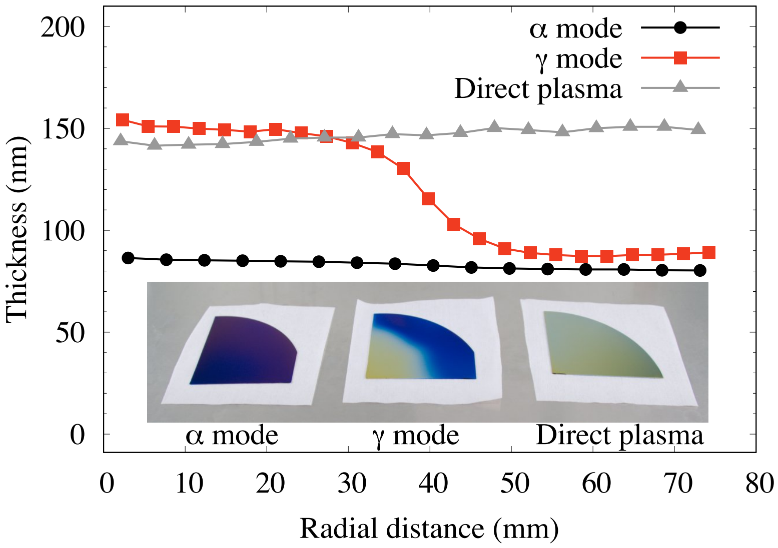

FIGURE 33 Thicknesses of the PEALD ZnO films deposited with remote α and γ mode plasma, and with direct plasma. Measured as a function of the distance from the reactor center. Inset: a photograph of the corresponding films. Adapted from PIII, with permission from IOP Publishing.

Figure 33 shows the thicknesses of the ZnO films as a function of the radial distance from the wafer/reactor center. The α mode films, both with remote and direct plasma, exhibit uniform thicknesses throughout the deposition area. However, the direct plasma deposited film is thicker, corresponding to a GPC value of ca. 1.45 Å, while for the film deposited in the remote α the GPC value was measured to be ca. 0.85 Å. A substantial radial thickness non-uniformity can be observed in the film deposited with the remote γ mode plasma. In the region close to the electrode center the film thickness corresponds to the direct plasma deposited film, and the thickness decreases abruptly towards the wafer edge. This is also visibly observable in the photograph in the inset of Fig. 33.

The elemental compositions of the films, measured with ToF-ERDA, are presented in Table 3. Similarly to the thickness measurements, the correspondences between the film deposited using direct plasma and the central region of the γ mode deposited film can be detected. Same applies to the film grown with remote α mode and the edges of the γ mode deposited film.

TABLE 3 Elemental composition of the ZnO films, measured using ToF-ERDA.

Sample	H (at.-%)	C (at.-%)	N (at.-%)	O (at.-%)	Zn (at.-%)	O/Zn ratio
α mode	13 ± 1	5.6 ± 0.5	1.4 ± 0.2	50 ± 2	30 ± 2	1.7 ± 0.2
γ mode (e.)	11 ± 1	4.3 ± 0.5	2.1 ± 0.2	49 ± 2	34 ± 2	1.5 ± 0.2
γ mode (c.)	3 ± 0.5	0.5 ± 0.2	0.2 ± 0.1	52 ± 2	45 ± 2	1.2 ± 0.2
Direct plasma	4 ± 0.5	0.5 ± 0.2	0.4 ± 0.1	51 ± 2	44 ± 2	1.2 ± 0.2

These results are also in accordance with the compositions of the PEALD ZnO films deposited using the same type of plasma conditions presented in Table 2 in Chapter 6. However, as it can be seen, the slight increase in the temperature, from RT to 50 °C results a reduction in the film impurity content and a corresponding improvement in the O/Zn ratio.

In addition, according to to the XRD measurements, all the films were polycrystalline with hexagonal wurtzite. The direct plasma deposited film, as well as the center of the γ mode deposited film appeared to be more crystalline, exhibiting a strong *a*- and *c*-axis orientation, shown as intense peaks at $\sim$31.6° and 34.2° 2θ angles (Fig. 34).

TiO_2

The dependence on the plasma mode was also observed in the TiO_2 films. As in the ZnO films, the non-uniform thickness over the deposition area was detected solely in the film deposited with γ mode plasma. The GPC values for the remote α mode deposited film and the film grown with direct plasma were ca. 0.57 Å and 0.87 Å, respectively . However, unlike in the case of the ZnO films, the elemental composition was independent on the plasma conditions. All the films were close to stoichiometric TiO_2, having O/Ti ratios within 2.1–2.2. The total (H+C+N+Cl) impurity concentration was measured to be less than 1.5 at.-%. The only notable difference was observed in the N content, which was slightly elevated in the direct plasma deposited films and at the thicker central regions of the γ mode film.

The XPS measurements revealed that this N incorporation is attributed to the

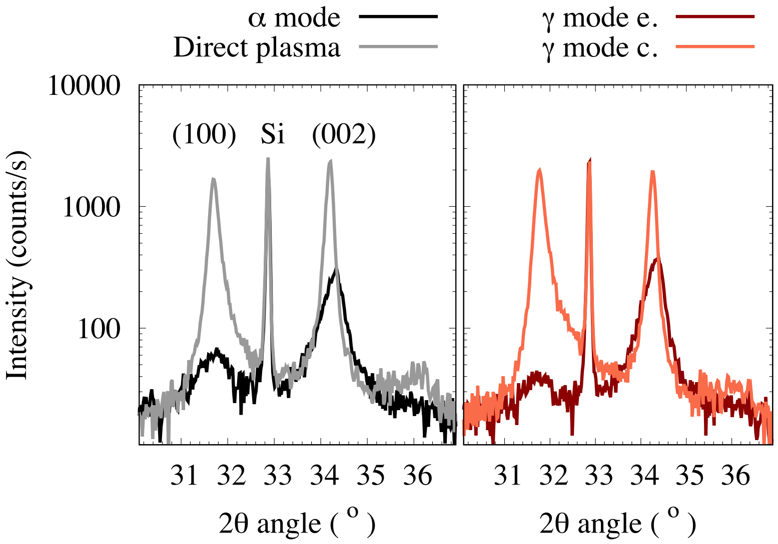

FIGURE 34 XRD patterns of the ZnO films. Adapted from PIII with permission from IOP Publishing.

presence of low TiO/TiN content in the films. Figure 35 shows the Ti 2p and N 1s spectra of the remote α and direct plasma deposited films. The N 1s peak is absent in the α mode deposited film, which was measured to have a negligible N content. A peak at ∼397 eV in the spectrum of direct plasma film indicates the formation of Ti-N bonds. Despite the low N content in the films, the difference can also be seen in the Ti 2p spectra, where the broadening of the peaks towards the lower binding energies is attributed to the TiON and TiN components in the direct plasma deposited film [146, 226].

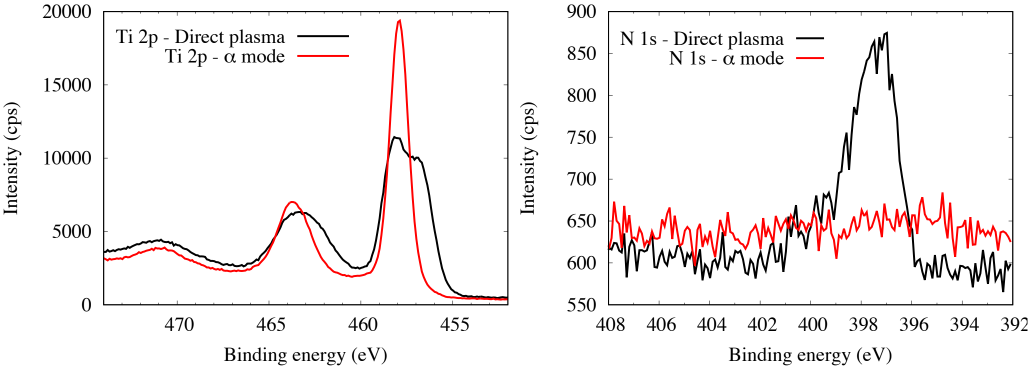

FIGURE 35 Left: XPS Ti 2p spectra of the direct plasma (black) and α mode (red) deposited TiO_2 films. Right: Corresponding N 1s spectra.

While the composition of the films was observed to be somewhat insensitive to the plasma conditions, the structure of the films showed strong dependence on the plasma mode. The GIXRD patters of the films are presented in the Fig.36, and the corresponding surface morphology is shown in the helium ion micrographs in Fig. 37. The film deposited with α mode appears smooth and amorphous, while the direct plasma TiO_2 film is fully crystalline with anatase phase. The edges of the γ mode deposited films appear amorphous in the GIXRD pattern, but the closer inspection of the surface structure reveals that the film consists of cone shaped crystallites in an amorphous matrix. The surface coverage of the crystallites is seen to increase towards the film center, which expresses anatase structure also in the GIXRD pattern.

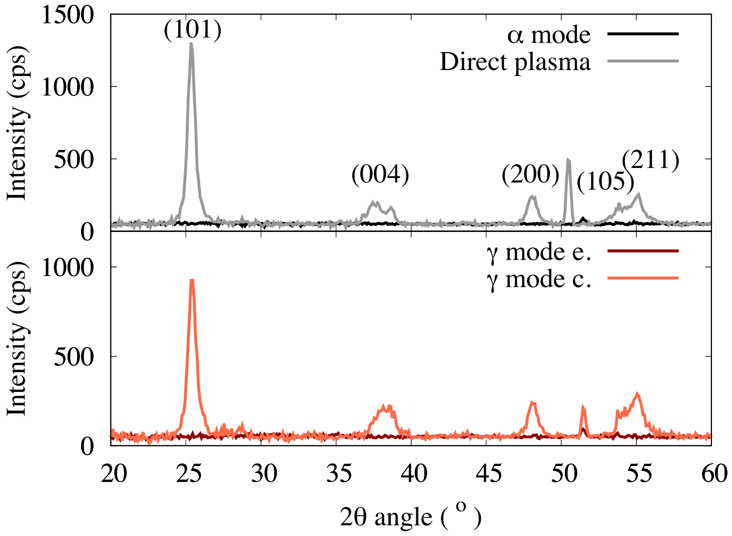

FIGURE 36 GIXRD patterns of the TiO_2 films. Diffraction peaks identifying the crystalline anatase structure are labelled.

7.1.4 Generation of a 'parasitic' discharge

The experimental results indicate that the γ mode is accompanied with direct plasma like conditions at the central region of the deposition area. The analysis of the ZnO film properties shows differences in the films that are in accordance with the results in PII, presented in Chapter 6. In the case of TiO_2, there are examples in the literature, showing the strong correlation between the TiO_2 crystallization and the ion energy and flux on the deposition surface. Thus, the mode-related differences in the PEALD ZnO and TiO_2 film properties can be considered to be a consequence of ion bombardment to the substrate during the deposition [143, 144, 147]. Figure 38 shows a sketch of the proposed ion energy distribution on the substrate, based on the observed changes in the films deposited under different plasma conditions.

In the case of direct plasma the ions are accelerated over the plasma sheath to

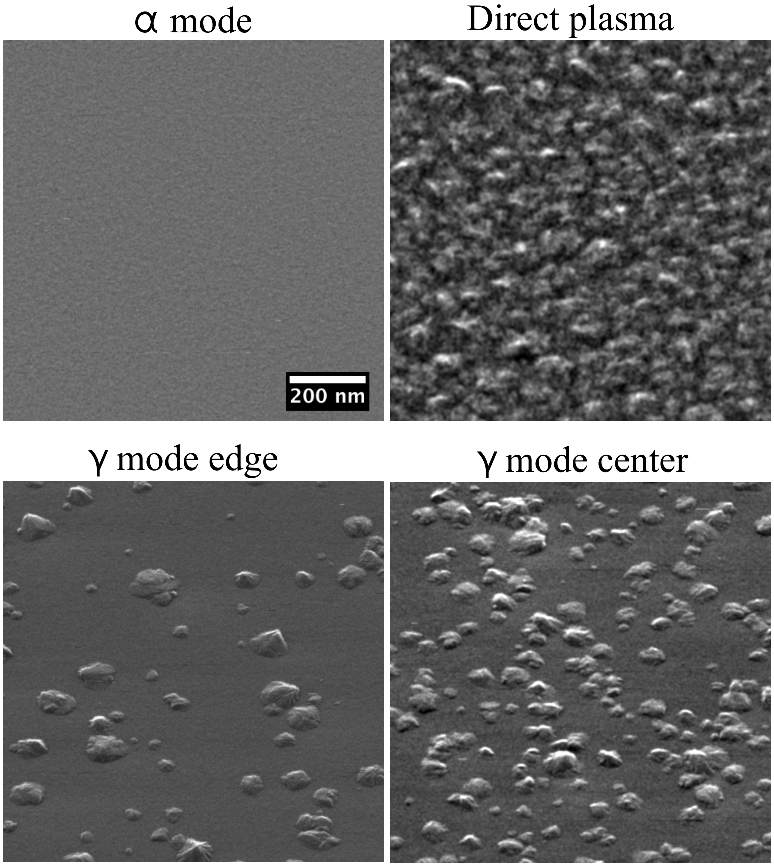

FIGURE 37 HIM images of the TiO_2 films. The samples are tilted to 45°. Adapted from PIII with permission from IOP Publishing.

an energy with the maximum being proportional to the plasma potential ($E \propto q \cdot V_p$)[2]. Despite the collisional sheath it can still be assumed that the ion flux and energy deposition at the substrate is substantial. In the remote α mode the ions with the same initial energy can still pass through the grid holes, their flux being restricted by the grid transparency, but these ions quickly recombine and lose their energy in the collisions in the gas volume between the grid and the substrate.

In the γ mode the high-energy secondary electrons can penetrate through the grid holes. The energy of the electrons is sufficient for electron-impact ionization of the neutral gas below the grid, thus causing a 'parasitic' plasma component between the grid and the substrate. As a result, ion bombardment at the substrate takes place. As discussed in Section 7.1.1, the plasma mode transition into the high-current γ mode is typically accompanied by a contraction of the discharge between the powered and grounded electrode. This contraction can be consid-

---

[2] In low-temperature processing plasmas ions are typically singly ionized i. e. q=1 and ion energy thus $E \propto e \cdot V_p$.

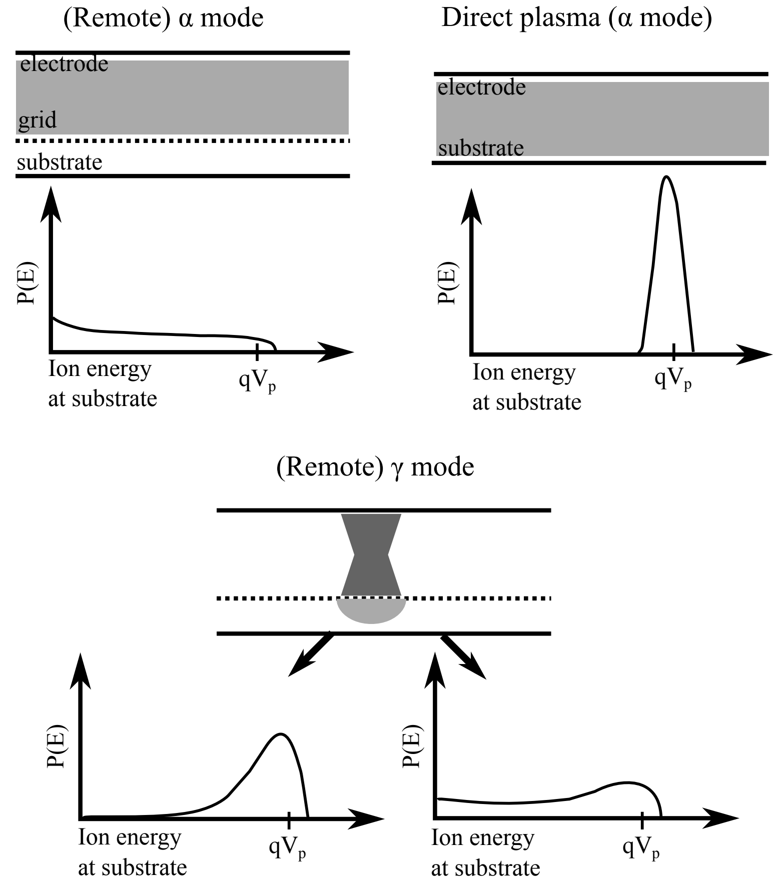

FIGURE 38 A sketch of proposed qualitative ion energy distributions at the substrate with remote α mode, direct plasma, and remote γ mode.

ered as a pinch effect caused by the current surge through the discharge. The current between the electrodes can generate an azimuthal magnetic field component, which causes the pinch effect and, thus, restricts the cross-sectional area of the plasma column. This presumably causes the locality of the ion-substrate interaction. The ion flux and energy distribution depends on the distance from the discharge. At the center of the discharge the ion bombardment to the substrate can be similar to the direct plasma, but the ion energy decreases as the distance is increased, and at a certain distance no energetic ions are able to reach the substrate.

The significance of the mode-dependent non-uniformities in the film properties depends on the reactor pressure as well as on the geometry, in particular the distance between the grid and the substrate. As the 'parasitic' component is sustained by the energetic electrons emitted from the grid surfaces, the path length of these electrons with sufficient energy for ionization is determined by the gas pressure. The system specific operation pressure of a PEALD reactor is typically limited within an order of magnitude. By increasing the grid-substrate distance it might be possible to reduce the local effects of this parasitic plasma component, but as was presented in Section 6.1.2 the longer distance leads to a reduction in the radical flux, being non-beneficial to the film growth. In addition, reducing the grid transparency, mainly the diameter of the individual holes, could mitigate the flux of the electrons with energy sufficient for ionization below the grid, and thus prevent the formation of the parasitic discharge [227]. However, this would also have a negative impact on the radical flux and the overall processing efficiency. Therefore, it can be concluded that the α-γ transition sets an upper limit to the applied RF power/voltage when uniform discharge is appreciated.

7.2 Inductively-coupled discharges

7.2.1 *E* and *H* plasma modes

The mode transitions are not restricted solely to the CCP discharges, and the presence of a mode transition was observed also in the inductively-coupled plasma used for the ICP-PEALD depositions presented in Chapter 6. In the following some preliminary data of the *E*–*H* mode transition under typical PEALD conditions with O_2–Ar and NH_3–Ar plasmas are presented.

In the electrostatic *E* mode, which is typically observed with low applied powers, the electric field is generated between the segments of the coil making the plasma coupling capacitive. Increasing the coil current i. e. by increasing the applied power over a specific critical value the plasma makes a relatively abrupt transition in to the high-density inductive mode, known also as the electromagnetic *H* mode [109, 167]. The onset of the transition is dependent on the plasma gas composition and the pressure [228–230]. In general, the mode transition from *E* to *H* mode is accompanied with an increase in n_e. Together with the weaker electric field in the *H* mode and the increased electron–neutral collision frequency this leads to a decrease in the plasma potential and T_e.

O_2–Ar plasma

A mixture of O_2 and Ar is typically used for the metal oxide film deposition in the ICP-PEALD. To investigate the characteristics of the plasma modes and the *E*–*H* mode transition, the OES measurements were done with varying plasma generator parameters. The spectra were recorded at a distance of ca. 5 cm below the plasma generator, the optical fiber viewing perpendicularly to the plasma. Figure 39 shows examples of optical emission spectra of the plasma with applied powers of 500, 1000, and 2000 W. The ratio of the dominant peak intensities does not change at the applied power range of 500–1000 W, and only a small increase in the total optical emission intensity can be observed. The low-power spectra consists of mainly lines of excited neutral Ar, with the most intense line being at 750–751 nm, the main contributor to this line being the Ar($2p_1 \rightarrow 1s_2$) transition [179]. The other intense line of Ar denoted in Fig. 39 at 811 nm is associated to the Ar($2p_9 \rightarrow 1s_5$) transition. In the spectrum recorded with the 2000 W plasma power the emission line at 777 nm, originating from atomic oxygen becomes dominant.

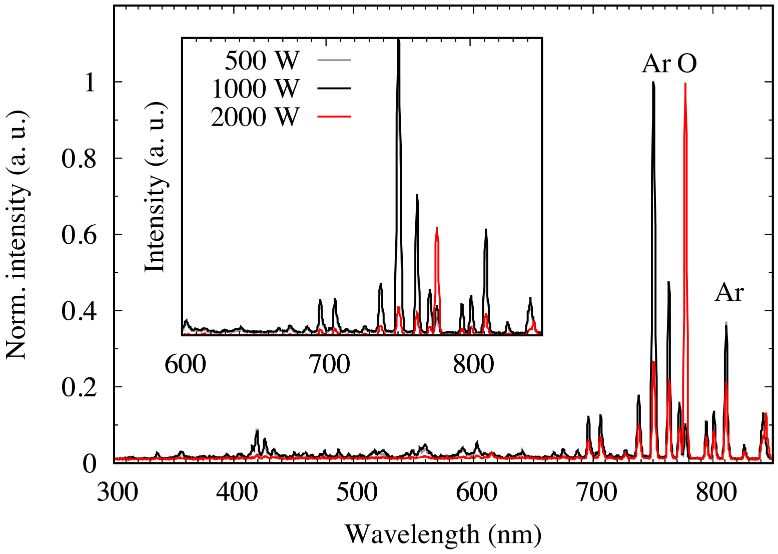

FIGURE 39 Optical emission spectra of the inductively-coupled O_2–Ar plasma with plasma powers of 500, 1000, and 2000 W. The spectra are normalized to the highest peak intensity of each spectrum. Inset: Corresponding integration time–normalized spectra at wavelength range 650–860 nm. Adapted from PII

When the spectral changes as a function of applied power are compared to the RF characteristics of the plasma generator, the region where *E*–*H* transition occurs can be defined. Figure 40(left) shows the output RF frequency, and the DC voltage and current of the ICP generator. It can be seen that the current rises linearly when the power is increased, until at 1000 W the current reaches the maximum, after which the DC voltage starts to increase. When the intensities of the selected peaks are compared, the intensities of the Ar lines decrease drastically at this applied power.

The selected Ar emission lines corresponds to the decays of Ar excited to high energy levels. These energy levels can be occupied either by direct electron-impact excitation of by ionization followed by recombination [231]. However, for both the excitation and ionization processes the threshold energies are above 13 eV [232], and the dominance of these lines in the spectrum at low powers (i. e. the

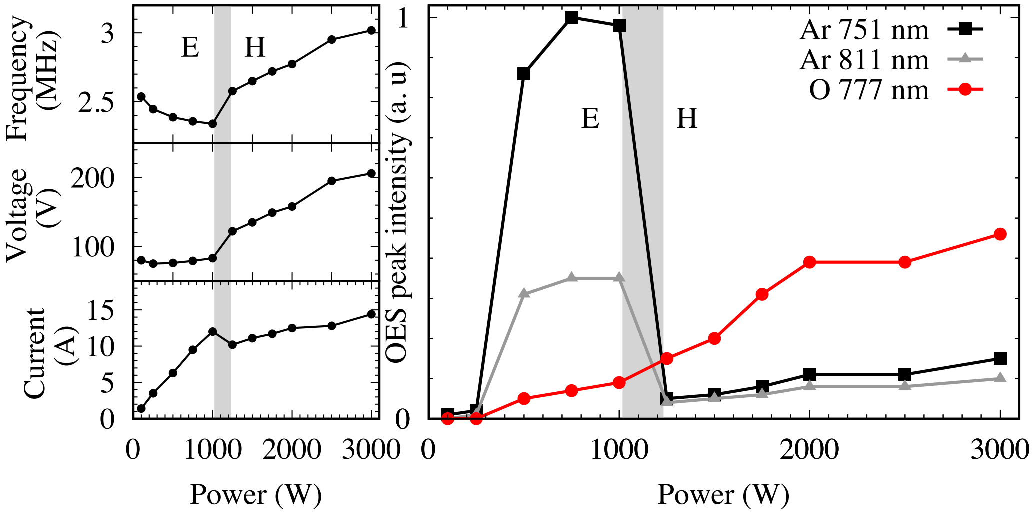

FIGURE 40 Left: ICP generator output frequency, DC voltage, and DC current as a function of the applied power. Right: Ar 751 nm, Ar 811 nm, and O 777 nm peak intensities of the recorded OES spectra as a function of the applied power, normalized to the highest Ar 751 nm intensity. The *E*–*H* transition region is highlighted with grey. Adapted from paper PII.

E mode), and the sudden decrease in the intensity corresponds to decrease in the effective electron temperature T_{eff} in the transition to *H* mode. Typically, especially at low pressures, the transition is accompanied by the increase in the total optical emission [229]. In this case the opposite was observed. A possible reason for this can be a change in the plasma spatial distribution associated to the transition. The plasma can be more restricted to the cylindrical volume within the inductive coil in the *H* mode, and thus the observed optical intensity in the near plasma afterglow region, where the OES measurements were performed, could be reduced. Another explanation is related to the properties of the oxygen discharge. This has been recently reported by Wegner et al. [233, 234], who discovered that the oxygen plasma transition to the *H* mode (at moderate pressures of $\sim$0.1 mbar) is accompanied by the increase in the metastable molecular oxygen, which leads to a decrease in the electronegativity of the discharge due to the loss of O^- ions in the detachment processes (see Section 3.3). In addition to the direct electron impact excitation, the O excitation to the emitting levels for 777 nm and 845 nm transitions are a result of the mutual neutralization process of O^- and O^+. Thus the decrease in the total O^- concentration compensates the intensity increase caused by the sudden increase in the plasma density. The increase in the n_e within the power increase in the *H* mode can, however, be observed as a slow increase in the total optical emission intensity of O 777 nm line.

Even when the high applied power is used the capacitive mode is typically present at the plasma ignition before the inductive plasma is formed [109]. This feature was also observed in the plasma generator used for the ICP-PEALD. Figure 41 shows the O_2–Ar plasma ignition with setpoint power of 1500 W. From the plasma generator output values and the corresponding time-resolved intensities of the OES spectra it can be seen that for the first 1 s after the ignition the plasma is in the capacitive mode before an abrupt transition to the inductive coupling.

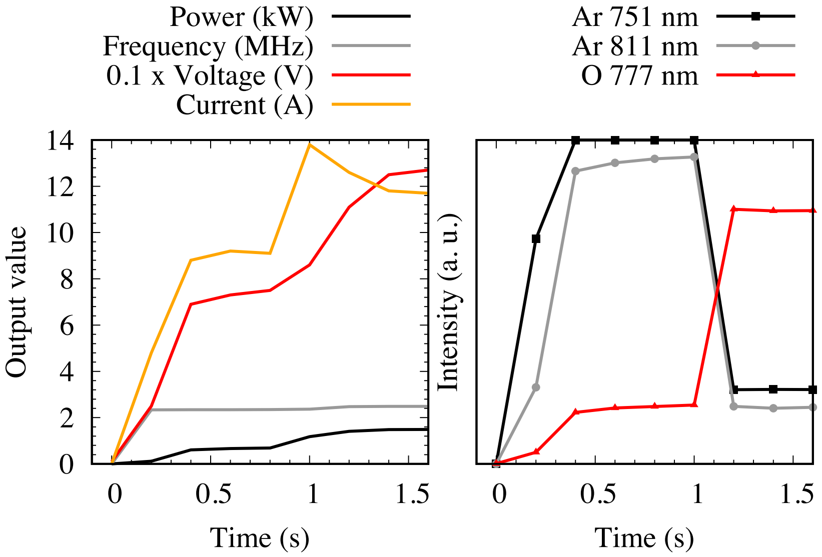

FIGURE 41 Left: ICP generator output power, frequency, DC voltage, and DC current as a function of the time. Data courtesy of Dr. Alexey Veselov. Right: Ar 751 nm, Ar 811 nm, and O 777 nm peak intensities of the recorded OES spectra as a function of time, normalized to the highest Ar 751 nm intensity. The recorded Ar 751 nm peaks are saturated at 0.2–1 s.

NH_3–Ar plasma

As a brief and final example, the *E*–*H* mode transition was also observed in the NH_3–Ar plasma, typically used in the PEALD of metal nitride films. As in the case of the O_2–Ar plasma, the transition changes the relative intensities of the different optical emission lines and bands observed in the OES spectra. Figure 42 shows the optical emission spectra of the plasma recorded with plasma powers of 1000, 2000, and 3000 W.

As in the previous example, the excited Ar dominates the spectrum at the low applied powers. The different dissociation processes[3] of the NH_3 can be seen as

---

[3] NH_3 being a complex molecule results in enormous amount of different possible plasma processes, involving also the Ar in neutral–neutral and ion–neutral collisions. For example, atomic H can be produced in processes such as $e + NH_3 \rightarrow NH_2^- + H$, $NH_3 + Ar \rightarrow NH_2 + H + Ar$, $e + NH_3^+ \rightarrow NH_2 + H$, and $NH + NH \rightarrow N_2 + 2H$, just to name a few [235, 236].

presence of the atomic hydrogen, namely H Balmer series, with the dominant line H_α at 656 nm, and a strong contribution of the 1st and 2nd positive systems of electronically excited N_2. With applied power of 1000 W also the 1st negative system of N_2^+ can be observed, with the dominant emission band head at 391 nm.

In Fig. 43 the intensities of these selected species in the spectra are presented as a function of the plasma power, and compared to the RF characteristics of the ICP generator during the *E*–*H* mode transition. The transition onset was observed to be within the region of 1500–1750 W, being higher than in the O_2–Ar plasma with similar gas feed. The relative changes in the OES intensities during the transition are less drastic and straightforward than in the O_2–Ar plasma, but the characteristic features, such as the decrease in the electron temperature can be deduced. For example, the intensities of the Ar and N_2^+ lines, both being generated by high threshold energy electron-impact processes, decrease in the transition.

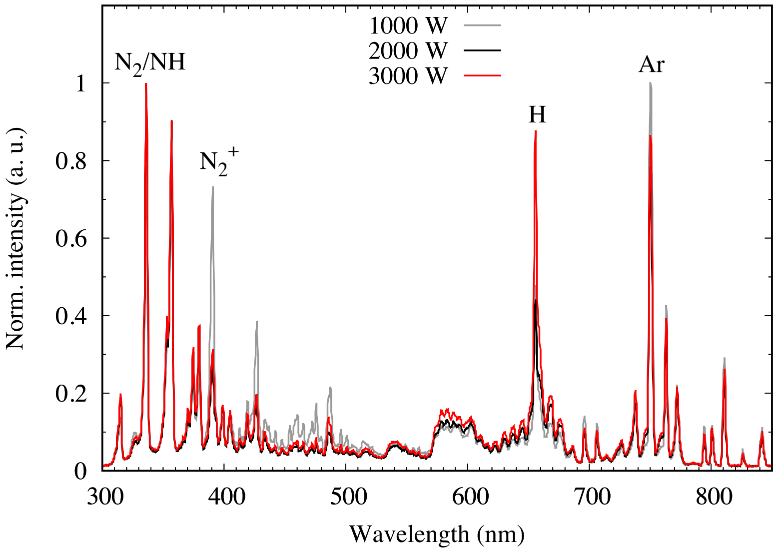

FIGURE 42 Optical emission spectra of the inductively-coupled NH_3–Ar plasma with plasma powers of 1000, 2000, and 3000 W. The spectra are normalized to the highest peak intensity of each spectrum

The mode transition may have an effect also on the PEALD processing, as the concentrations of the different plasma species potentially change also at the substrate level. Some indication of this was observed in the RT-PEALD of ZnO films, presented in Chapter 6, where the GPC of the films was reduced when the *H* mode plasma was used for the depositions. However, further studies and analysis of the plasma and its effects on the films would be needed to gain a better understanding of the significance of different plasma processes for PEALD film growth and properties.

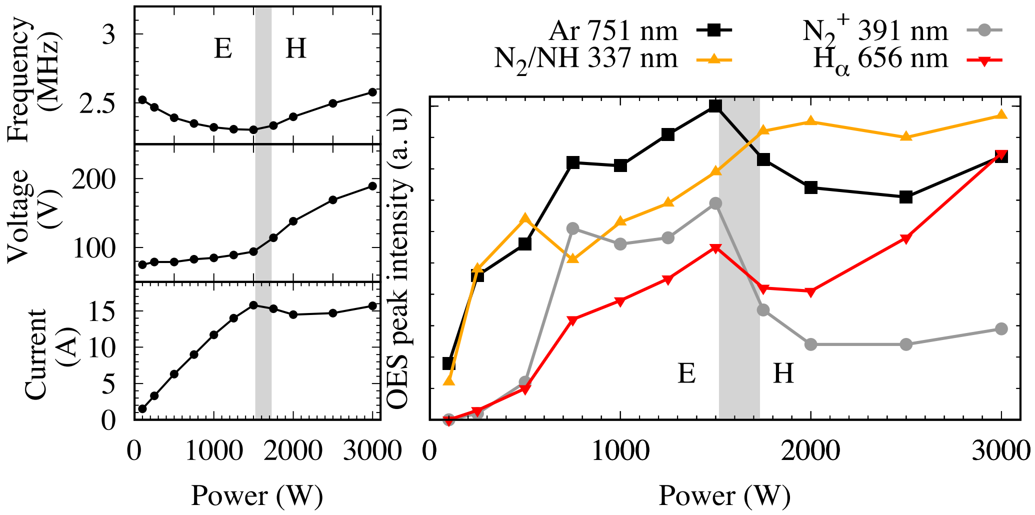

FIGURE 43 Left: ICP generator output frequency, DC Voltage, and DC current as a function of the applied power. Right: Ar 751 nm, N_2^+ 391 nm, N_2/NH 337 nm and H_α 656 nm peak intensities of the recorded OES spectra as a function of the applied power, normalized to the highest Ar 751 nm intensity. The *E*–*H* transition region is highlighted with grey.

8 SUMMARY AND OUTLOOK

ALD has become a state-of-the-art technique for thin film deposition, and it has proven to meet the demanding requirements for a variety of applications. With continuous expansion of the material selection and divergent needs for conformal, high quality, and ultra thin films, emerging branches of technology are setting new opportunities and challenges for ALD processing. For example, flexible electronics and other applications utilizing polymer materials require lower deposition temperatures than typically used in ALD.

In PEALD the processing freedom is increased by introduction of the reactive plasma species to the ALD. This allows to reduce the deposition temperature and also enables the growth of materials not easily accessible by traditional thermal ALD. However, the complexity of the plasmas and the interaction of the different species during the deposition make the establishment of the processes more convoluted.

The work in this thesis focused on the limitations of the low-temperature ALD and PEALD processing with demonstrated examples of metal oxide thin films. It was shown by depositing ZnO and Al_2O_3 on two different grades of PMMA, that in low-temperature thermal ALD on polymers the initiation of the growth depends significantly on both the deposited material and the surface of the polymer. The delay of hundreds of ALD cycles on the initial ZnO nucleation and clustering, followed by island-type growth may hamper the use of these films e. g. in barrier applications on smooth and dense polymer surfaces. However, it was also shown that despite the slow growth and increased surface roughness these films exhibited changes in the surface wettability under UV-illumination, being thus potentially applicable for surface functionalization purposes.

To overcome the issue of slow nucleation and inefficient processing due to long purging times ZnO films were also deposited by means of room-temperature

PEALD, using three different reactor configurations. Here, it was demonstrated that the effects of different plasma species to the film growth are substantial in the absence of additional thermal energy. Especially the role of the energetic ion bombardment during the deposition was proven to be significant. The viability of the room-temperature PEALD on polymer substrates was shown, the growth being similar on PMMA, PC, as well as on inorganic Si substrates. However, the higher quality films could only be deposited under conditions leading to plasma-induced damage on the polymer substrates.

Based on the experiments regarding the low-temperature ALD and PEALD on polymers, it can be concluded that the most efficient way for thin film deposition on polymer substrates would combine the advantages of the both techniques. The nucleation can be enhanced by applying plasma pulses for surface pre-treatment before deposition by thermal ALD. In this approach an optional plasma-enhancement can also be used to controllably modify the film properties while minimizing the damage to the substrates.

The last part of the thesis focused on the plasma mode transitions, which are fundamental characteristics of plasmas but have so far rarely been taken into account in PEALD processing. It was observed that the transition from the so-called α to the γ–mode in the capacitively coupled plasma used in the remote PEALD sets an upper limit for the applied RF power via formation of a parasitic discharge component that leads to non-uniform films. Similarly to the α–γ transitions in the capacitively-coupled plasmas, E–H transitions in inductively-coupled plasmas were observed under typical PEALD processing conditions.

The work on PEALD, both the room-temperature processing and the mode transition studies, demonstrated the importance of the comprehension of different plasma properties. The influence of the reactor configuration to the deposition is often neglected or simply forgotten, and more thorough studies of the plasma-surface interactions with respect to the thin film deposition would benefit the optimization of different PEALD processes and also give prospects for device development.

REFERENCES

[1] N. Puttaraksa, M. Napari, O. Chinthavorn, R. Norarat, T. Sajavaara, M. Laitinen, S. Singkarat, and H. J. Whitlow. Direct writing of channels for microfluidics in silica by MeV ion beam lithography. *Adv. Mat. Res.* 254 (2011) 132.

[2] Y.Zhao, J.-C. Grivel, M. Napari, D. Pavlopoulos, J. Bednarčic, and M. von Zimmerman. Highly textured $Gd_2Zr_2O_7$ films grown on textured Ni -5 at. % W substrates by solution deposition route: Growth, texture evolution and microstructure dependency. *Thin Solid Films* 520 (2012) 1965.

[3] R. Norarat, N. Puttaraksa, M. Napari, A. R. A. Sagari, M. Laitinen, T. Sajavaara, P. Yotprayoonsak, M. Petterson, O. Chienthavorn, and H. J. Whitlow. Why are hydrogen ions best for MeV ion beam lithography? *Microelectron. Eng.* 102 (2013) 22.

[4] L. Rojas, R. Norarat, M. Napari, H. Kivistö, O. Chienthavorn, and H. J. Whitlow. Lithographic fabrication of soda-lime glass based microfluidics. *Nucl. Instrum. Meth. B* 306 (2013) 296.

[5] N. Puttaraksa, M. Napari, L. Meriläinen, H. J. Whitlow, T. Sajavaara, and L. Gilbert. High speed microfluidic prototyping by programmable proximity aperture MeV ion beam lithography. *Nucl. Instrum. Meth. B* 306 (2013) 296.

[6] H. J. Whitlow, S. Gorelick, N. Puttaraksa, M. Napari, M. J. Hokkanen, and R. Norarat. Development of procedures for programmable proximity aperture lithography. *Nucl. Instrum. Meth. B* 306 (2013) 307.

[7] M. Palosaari, K. Kinnunen, J. Julin, M. Laitinen, M. Napari, T. Sajavaara, W. B. Doriese, J. Fowler, C. Reintsema, D. Swetz, D. Schmidt, J. Ullom, and I. Maasilta. Transition-edge sensors for particle induced X-ray emission measurements. *J. Low Temp. Phys.* 176 (2014) 285.

[8] N. Puttaraksa, H. J. Whitlow, M. Napari, L. Meriläinen, and L. Gilbert. Development of a microfluidic design for an automatic lab-on-chip operation. *Microfluid. Nanofluid.* 20 (2016) 142.

[9] S. M. George. Atomic Layer Deposition: An Overview. *Chem. Rev.* 110 (2009) 111.

[10] N. P. Dasgupta, H.-B.-R. Lee, S. F. Bent, and P. S. Weiss. Recent Advances in Atomic Layer Deposition. *Chem. Mater.* 28 (2016) 1943.

[11] R. Puurunen. A Short History of Atomic Layer Deposition: Tuomo Suntola's Atomic Layer Epitaxy. *Chem. Vap. Deposition* 20 (2014) 332.

[12] T. Suntola and J. Hyvärinen. Atomic Layer Epitaxy. *Ann. Rev. Mater. Sci.* 15 (1985) 177.

[13] T. Suntola and J. Antson. *Method for producing compound thin films*. International patent FIN 52359, US 4 085 430. 1977.

[14] R. W. Johnson, A. Hultqvist, and S. F. Bent. A brief review of atomic layer deposition: from fundamentals to applications. *Mater. Today* 17 (2014) 236.

[15] C. S. Hwang, ed. *Atomic Layer Deposition for Semiconductors*. Springer, 2014.

[16] B. J. O'Neill, D. H. K. Jackson, J. Lee, C. Canlass, P. C. Stair, C. L. Marshall, J. W. Elam, T. F. Kuech, J. A. Dumesic, and G. W. Huber. Catalyst Design with Atomic Layer Deposition. *ACS Catal.* 5 (2015) 1804.

[17] M. Tilli, T. Motooka, V.-M. Airaksinen, S. Franssila, M. Paulasto-Kröckel, and V. Lindroos, eds. *Handbook of Silicon based MEMS Materials and Technologies*. 2nd ed. Elsevier Inc., 2015.

[18] J. R. Bakke, K. L. Pickrahn, T. P. Brennan, and S. F. Bent. Nanoengineering and interfacial engineering of photovoltaics by atomic layer deposition. *Nanoscale* 3 (2011) 3482.

[19] D. H. Kim, M. D. Losego, Q. Peng, and G. N. Parsons. Atomic Layer Deposition for sensitized solar cells: Recent progress and prospects. *Adv. Mater. Interfaces* 3 (2016) 1600354.

[20] M.-H. Tseng, H.-H. Yu, K.-Y. Chou, J.-H. Jou, K.-L. Lin, C.-C. Wang, and F.-Y. Tsai. Low-temperature gas-barrier films by atomic layer deposition for encapsulating organic light emitting diodes. *Nanotechnology* 27 (2016) 295706.

[21] J.-S. Park, H. Chae, H. K. Chung, and S. I. Lee. Thin film encapsulation for flexible AM-OLED: a review. *Semicond. Sci. Technol.* 26 (2011) 034001.

[22] D. C. Lim, K.-D. Kim, S.-Y. Park, E. M. Hong, H. O. Seo, J. H. Lim, K. H. Lee, Y. Jeong, C. Song, E. Lee, Y. D. Kim, and S. Cho. Towards fabrication of high-performing organic photovoltaics: new donor-polymer, atomic layer deposited thin buffer layer and plasmonic effects. *Energy Environ. Sci.* 5 (2012) 9803.

[23] D. Yu, Y.-Q. Yang, Z. Chen, Y. Tao, and Y.-F. Liu. Recent progress on thin-film encapsulation technologies for organic electronic devices. *Opt. Comm.* 362 (2016) 43.

[24] S. A. Skoog, J. W. Elam, and R. J. Narayan. Atomic layer deposition: medical and biological applications. *Int. Mater. Rev.* 58 (2013) 113.

[25] H. Kim and I.-K. Oh. Review of plasma-enhanced atomic layer deposition: Technical enabler of nanoscale device fabrication. *Jpn. J. Appl. Phys.* 23 (2014) 03DA01.

[26] H. B. Profijt, S. E. Potts, M. C. M. van de Sanden, and W. M. M. Kessels. Plasma-assisted atomic layer deposition: Basics, opportunities, and challenges. *J. Vac. Sci. Technol. A* 29 (2011) 050801.

[27] V. Miikkulainen, M. Leskelä, M. Ritala, and R. Puurunen. Crystallinity of inorganic films grown by atomic layer deposition: Overview and general trends. *J. Appl. Phys.* 113 (2013) 021301.

[28] M. D. Groner, F. H. Fabreguette, J. W. Elam, and S. M. George. Low-temperature Al_2O_3 atomic layer deposition. *Chem. Mater.* 16 (2004) 639.

[29] T. Tynell and M. Karppinen. Atomic layer deposition of ZnO: a review. *Semicond. Sci. Technol.* 29 (2014) 043001.

[30] M. Lorenz et al. The 2016 oxide electronic materials and oxide interfaces roadmap. *J. Phys. D: Appl. Phys.* 49 (2016) 433001.

[31] R. L. Puurunen. Surface chemistry of atomic layer deposition: A case study for the trimethylaluminum/water process. *J. Appl. Phys* 97 (2005) 121301.

[32] M. Leskelä and M. Ritala. Atomic Layer Deposition (ALD): from precursors to thin film structures. *Thin Solid Films* 409 (2002) 138.

[33] B. S. Lim, A. Rahtu, and R. G. Gordon. Atomic layer deposition of transition metals. *Nat. Mater.* 2 (2003) 749.

[34] S. M. George, B. Yoon, and A. A. Dameron. Surface chemistry of molecular layer deposition of organic and hybrid organic-inorganic polymers. *Acc. Chem. Res.* 42 (2009) 498.

[35] O. M. E. Ylivaara, L. Kilpi, W. Liu, S. Sintonen, S. Ali, M. Laitinen, J. Julin, E. Haimi, T. Sajavaara, H. Lipsanen, S.-P. Hannula, H. Ronkainen, and R. L. Puurunen. Aluminum oxide/titanium dioxide nanolaminated grown by atomic layer deposition: growth and mechanical properties. *J. Vac. Sci. Technol. A* 35 (2017) 01B105.

[36] R. L. Puurunen. Growth per cycle in atomic layer deposition: A theoretical model. *Chem. Vap. Deposition* 9 (2003) 249.

[37] M. Ylilammi. Monolayer thickness in atomic layer deposition. *Thin Solid Films* 279 (1996) 124.

[38] V. Vandalon and W. M. M. Kessels. What is limiting low-temperature atomic layer deposition of Al_2O_3? A vibrational sum-frequency study. *Appl. Phys. Lett.* 108 (2016) 011607.

[39] S. E. Potts and W. M. M. Kessels. Energy-enhanced atomic layer deposition for more process and precursor versatility. *Coord. Chem. Rev.* 257 (2013) 3254.

[40] J. W. Klaus and S. M. George. Atomic layer deposition of SiO_2 at room-temperature using NH_3-catalyzed sequential surface reactions. *Surf. Sci.* 447 (2000) 81.

[41] J. S. Jur and G. N. Parsons. Atomic layer deposition of Al_2O_3 and ZnO at atmospheric pressure in a flow tube reactor. *ACS Appl. Mater. Interfaces* 3 (2011) 299.

[42] M. B. M. Mousa, C. J. Oldham, J. S. Jur, and G. N. Parsons. Effect of temperature and gas velocity of growth per cycle during Al_2O_3 and ZnO atomic layer deposition at atmospheric pressure. *J. Vac. Sci. Technol. A* 30 (2012) 01A155.

[43] H. C. Guo, E. Ye, Z. Li, M.-Y. Han, and X. J. Loh. Recent progress of atomic layer deposition on polymeric materials. *Mater. Sci. Eng. C* 70 (2017) 1182.

[44] K. L. Jarvis and P. J. Evans. Growth of thin barrier films on flexible polymer substrates by atomic layer deposition. *Thin Solid Films* 624 (2017) 111.

[45] Y.-Y. Lin, Y.-N. Chang, M.-H. Tseng, C.-C. Wang, and F.-Y. Tsai. Air-stable flexible organic light-emitting diodes enabled by atomic layer deposition. *Nanotechnology* 26 (2015) 024005.

[46] T. Hirvikorpi, M. Vähä-Nissi, T. Mustonen, E. Iiskola, and M. Karppinen. Atomic layer deposited aluminum oxide barrier coatings for packaging materials. *Thin Solid Films* 518 (2010) 2654.

[47] M. Vähä-Nissi, J. Sievänen, E. Salo, P. Heikkilä, E. Kenttä, L.-S. Johansson, J. T. Koskinen, and A. Harlin. Atomic and molecular layer deposition for surface modification. *J. Solid State Chem.* 214 (2014) 7.

[48] M. Kemell, E. Färm, M. Ritala, and M. Leskelä. Surface Modification of thermoplastics by atomic layer deposition of Al_2O_3 and TiO_2 thin films. *Eur. Polym. J.* 44 (2008) 3564.

[49] T. O. Kääriäinen, P. Maydannik, D. C. Cameron, K. Lahtinen, P. Johansson, and J. Kuusipalo. Atomic layer deposition on polymer based flexible packaging materials: Growth characteristics and diffusion barrier properties. *Thin Solid Films* 519 (2011) 3146.

[50] G. Triani, J. A. Campbell, P. J. Evans, J. Davis, B. A. Latella, and R. P. Burford. Low temperature atomic layer deposition of titania thin films. *Thin Solid Films* 518 (2010) 3182.

[51] A. K. Roy, D. Deduytsche, and C. Detavernier. Wetting transitions of polymers via thermal and plasma enhanced atomic layer depositions. *J. Vac. Sci. Technol. A* 31 (2013) 01A147.

[52] J. S. Spagnola, B. Gong, and G. N. Parsons. Surface texture and wetting stability of polydimethylsiloxane coated with aluminum oxide at low temperature by atomic layer deposition. *J. Vac. Sci. Technol. A* 28 (2010) 1003.

[53] X. Liang, A. D. Lynn, D. M. King, S. J. Bryant, and A. W. Weimer. Biocompatible interface films deposited within porous polymers by atomic layer deposition (ALD). *ACS Appl. Mater. Interfaces* 1 (2009) 1988.

[54] J. Nikkola, J. Sievänen, M. Raulio, J. Wei, J. Vuorinen, and C. Y. Tang. Surface modification of thin film composite polyamide membrane using atomic layer deposition method. *J. Membrane Sci.* 450 (2014) 174.

[55] A. H. Brozena, C. J. Oldham, and G. N. Parsons. Atomic layer deposition on polymer fibers and fabrics for multifunctional and electronic textiles. *J. Vac. Sci. Technol. A* 34 (2016) 010801.

[56] W. M. M. Kessels and M. Putkonen. Advanced process technologies: Plasma, direct-write, atmospheric pressure, and roll-to-roll ALD. *MRS Bull.* 36 (2011) 907.

[57] P. Abgrall and A.-M. Gué. Lab-on-chip technologies: making a microfluidic network and coupling it into a complete microsystem - a review. *J. Micromech. Microeng.* 17 (2007) R15.

[58] Y. Lu, P. I. Reyes, J. Zhong, and H. Chen. Multifunctional ZnO nanostructure-based devices. In: *GaN and ZnO-based materials and devices*. Ed. by S. Pearton. Berlin Heidelberg: Springer, 2012. Chap. 13.

[59] O. Yamamoto. Influence of particle size on the antibacterial activity of zinc oxide. *Int. J. Inorg. Mater.* 3 (2001) 643.

[60] C. Wöll. The chemistry and physics of zinc oxide surfaces. *Prog. Surf. Sci.* 82 (2007) 55.

[61] Ü. Özgür, Y. I. Alivov, C. Liu, A. Teke, M. A. Reshchikov, S. Dogan, V. Avrutin, S.-J. Cho, and H. Morkoç. A comprehensive review of ZnO materials and devices. *J. Appl. Phys.* 98 (2005) 041301.

[62] Y. Q. Fu, J. K. Luo, X. Y. Du, A. J. Flewitt, Y. Li, G. H. Markx, A. J. Walton, and W. I. Milne. Recent developments of ZnO films for acoustic wave based bio-sensing and microfluidic applications: a review. *Sensor. Actuat. B* 143 (2010) 606.

[63] M. Tammenmaa, T. Koskinen, L. Hiltunen, and L. Niinistö. Zinc chalcogenide thin films grown by the atomic layer epitaxy technique using zinc acetate as source material. *Thin Solid Films* 124 (1985) 125.

[64] E. Guziewicz, I. A. Kowalik, M. Godlewski, K. Kopalko, V. Osinniy, A. Wójcik, S. Yatsunenko, E. Łusakowska, W. Paszkowicz, and M. Guziewicz. Extremely low temperature growth of ZnO by atomic layer deposition. *J. Appl. Phys.* 103 (2008) 022515.

[65] K.-S. An, W. Cho, B. K. Lee, S. S. Lee, and C. G. Kim. Atomic layer deposition of undoped and Al-doped ZnO thin films using the Zn alkoxide precursor methylzinc isopropoxide. *J. Nanosci. Nanotechnol.* 8 (2008) 4869.

[66] K. Kopalko, A. Wójcik, M. Godlewski, E. Łusakowska, W. Paszkowicz, J. Z. Domagała, M. M. Godlewski, A. Szczerbakow, Światek, and K. Dybko. Growth by atomic layer epitaxy and characterization of thin films of ZnO. *Phys. Stat. Sol. C* 2 (2005) 3.

[67] H. Makino, A. Miyake, T. Yamada, N. Yamamoto, and T. Yamomoto. Influence of substrate temperature and Zn-precursors on atomic layer deposition of polycrystalline ZnO films on glass. *Thin Solid Films* 517 (2009) 3138.

[68] T. Krajewski, E. Guziewicz, M. Godlewski, L. Wachnicki, I. A. Kowalik, A. Wojcik-Glodowska, M. Lukasiewicz, K. Kopalko, V. Osinniy, and M. Guziewicz. The influence of growth temperature and the precursors' doses on electrical parameters of ZnO thin films grown by atomic layer deposition. *Microelectron. J.* 40 (2009) 293.

[69] A. W. Ott and R. P. H. Chang. Atomic layer-controlled growth of transparent conducting ZnO on plastic substrates. *Mater. Chem. Phys.* 58 (1999) 132.

[70] S.-Y. Pung, K.-L. Choy, X. Hou, and C. Shan. Preferential growth of ZnO thin films by the atomic layer deposition technique. *Nanotechnology* 19 (2008) 435609.

[71] Y.-S. Min, C. J. An, S. K. Kim, J. Song, and C. S. Hwang. Growth and characterization of conducting ZnO thin films by atomic layer deposition. *Bull. Korean Chem. Soc.* 31 (2010) 2503.

[72] E. B. Yousfi, J. Fouache, and D. Lincot. Study of atomic layer epitaxy of zinc oxide by in-situ quartz crystal microgravimetry. *Appl. Surf. Sci.* 153 (2000) 223.

[73] C.-S. Ku, H.-Y. Lee, J.-M. Huang, and C.-M. Lin. Epitaxial growth of ZnO films at extremely low temperature by atomic layer deposition with interrupted flow. *Mater. Chem. Phys.* 120 (2010) 236.

[74] J. Malm, E. Sahramo, J. Perälä, T. Sajavaara, and M. Karppinen. Low temperature atomic layer deposition of ZnO thin films: Control of crystallinity and orientation. *Thin Solid Films* 519 (2011) 5319.

[75] E. Janocha and C. Pettenkofer. ALD of ZnO using diethylzinc as metal-precursor and oxygen as oxidizing agent. *Appl. Surf. Sci.* 257 (2011) 10031.

[76] S. K. Kim, C. S. Hwang, S.-H. K. Park, and S. J. Yun. Comparison between ZnO films grown by atomic layer deposition using H_2O or O_3 as oxidant. *Thin Solid Films* 478 (2005) 103.

[77] Y.-T. Lin, P.-H. Chung, H.-W. Lai, H.-L. Su, D.-Y. Lyu, K.-Y. Yen, T.-Y. Lin, C.-Y. Kung, and J.-R. Gong. Self-limiting growth of ZnO films on (0 0 0 1) sapphire substrates by atomic layer deposition at low temperatures using diethyl-zinc and nitrous oxide. *Appl. Surf. Sci.* 256 (2009) 819.

[78] S.-H. K. Park, C.-S. Hwang, H.-S. Kwack, J.-H. Lee, and H. Y. Chu. Characteristics of ZnO thin films by means of plasma-enhanced atomic layer deposition. *Electrochem. Solid-State Lett.* 9 (2006) G299.

[79] M. A. Thomas and J. B. Cui. Highly tunable electrical properties in undoped ZnO grown by plasma enhanced thermal-atomic layer deposition. *ACS Appl. Mater. Interfaces* 4 (2012) 3122.

[80] P. C. Rowlette, C. G. Allen, O. B. Bromley, A. E. Dubetz, and C. A. Wolden. Plasma-enhanced atomic layer deposition of semiconductor grade ZnO using dimethyl zinc. *Chem. Vap. Deposition* 15 (2009) 15.

[81] Y. Kawamura, N. Hattori, N. Miyatake, and Y. Uraoka. Comparison between ZnO films grown by plasma-assisted atomic layer deposition using H_2O plasma and O_2 plasma as oxidant. *J. Vac. Sci. Technol. A* 31 (2013) 01A142.

[82] I. A. Kowalik, E. Guziewicz, K. Kopalko, S. Yatsunenko, Wójcik-Głodowska, M. Godlewski, P. Dłużewski, E. Łusakowska, and W. Paszkowicz. Structural and optical properties of low-temperature ZnO films grown by atomic layer deposition with diethylzinc and water precursors. *J. Cryst. Growth* 311 (2009) 1096.

[83] T.-Y. Chiang, C.-L. Dai, and D.-M. Lian. Influence of growth temperature on the optical and structural properties of ultrathin ZnO films. *J. Alloy. Compd.* 509 (2011) 5623.

[84] T. Singh, T. Lehnen, T. Leuning, D. Sahu, and S. Mathur. Thickness dependence of optoelectronic properties in ALD growh ZnO. *Appl. Surf. Sci.* 289 (2014) 27.

[85] E. Guziewicz, M. Godlewski, L. Wachnicki, T. A. Krajewski, G. Luka, S. G. adn R. Jakiela, A. Stonert, W. Lisowski, M. Krawczyk, J. W. Sobczak, and A. Jablonski. ALD grown zinc oxide with controllable electrical properties. *Semicond. Sci. Technol.* 27 (2012) 074011.

[86] N. Y. Yuan, S. Y. Wang, C. B. Tan, X. Q. Wang, G. G. Chen, and J. N. Ding. The influence of deposition temperature on growth mode, optical and mechanical properties of ZnO films prepared by the ALD method. *J. Cryst. Growth* 366 (2013) 43.

[87] J. Y. Lee, C. M. Shin, J. H. Heo, C. R. Kim, J. H. Park, T. M. Lee, H. Ryu, C. S. Son, B. C. Shin, and W. J. Lee. Effects of O_2 plasma pre-treatment on ZnO thin films grown on polyethersulftone substrates at various deposition temperatures by atomic layer deposition. *Curr. Appl. Phys.* 10 (2010) S290.

[88] J. H. Heo, H. Ryu, and W.-J. Lee. Effect of O_2 plasma pretreatment on structural and optical properties of ZnO films on PES substrate by atomic layer deposition. *J. Ind. Eng. Chem.* 19 (2013) 1638.

[89] C. R. Kim, J. Y. Lee, C. M. Shin, J. Y. Leem, H. Ryu, J. H. Chang, H. C. Lee, C. S. Son, W. J. Lee, W. G. Jun, S. T. Tan, J. L. Zhao, and X. Sun. Effects of annealing temperature of buffer layer on structural and optical properties of ZnO thin film grown by atomic layer deposition. *Solid State Commun.* 148 (2008) 395.

[90] C. R. Kim, C. M. Shin, J. Y. Lee, J. H. Heo, T. M. Lee, H. J. Park, H. Ryu, C. S. Son, and J. H. Chang. Influence of annealing duration on optical property and surface morphology of ZnO thin film grown by atomic layer deposition. *Curr. Appl. Phys.* 10 (2010) S294.

[91] V. Lujala, J. Karp, M. Tammenmaa, and T. Suntola. Atomic layer epitaxy growth of doped zinc oxide thin films from organometals. *Appl. Surf. Sci.* 82–83 (1994) 34.

[92] G. Luka, B. S. Witkowski, L. Wachnicki, R. Jakiela, I. S. Virt, M. Andrzejczuk, M. Lewanowska, and M. Godlewski. Electrical and mechanical stability of aluminum-doped ZnO films grown on flexible substrates by atomic layer deposition. *Mater. Sci. Eng. B* 186 (2014) 15.

[93] S. J. Lim, J.-M. Kim, D. Kim, S. Kwon, J.-S. Park, and H. Kim. Atomic layer deposition of ZnO:N thin films transistors: The effects of N concentration on the devide properties. *J. Electrochem. Soc.* 157 (2010) H214.

[94] H. Yuan, B. Luo, S. A. Campbell, and W. L. Gladfelter. Atomic layer deposition of p-type phosphorus-doped zinc oxide films using diethylzinc, ozone and trimethylphosphite. *Electrochem. Solid-State Lett.* 14 (2011) H181.

[95] S.-B. Zhu, Y. Geng, H.-L. Lu, Y. Zhang, Q.-Q. Sun, S.-J. Ding, and D. W. Zhang. Effects of rapid thermal annealing on Hf-doped ZnO films grown by atomic layer deposition. *J. Alloy. Compd.* 340 (2013) 43.

[96] K. Bergum, H. Fjellvåg, and O. Nilsen. Thickness dependent structural, optical and electrical properties of Ti-doped ZnO films prepared by atomic layer deposition. *Appl. Surf. Sci.* 332 (2015) 494.

[97] W. J. Maeng and J.-S. Park. Growth characteristics and film properties of gallium doped zinc oxide prepared by atomic layer deposition. *J. Electroceram.* 31 (2013) 338.

[98] S. I. Boyadjiev, V. Georgieva, R. Yordanov, Z. Raicheva, and I. M. Szilágyi. Preparation and characterization of ALD deposited ZnO thin films studied for gas sensors. *Appl. Surf. Sci.* 387 (2016) 1230.

[99] M.-j. Jin, J. Jo, G. P. Neupane, J. Kim, K.-S. An, and J.-W. Yoo. Tuning of undoped ZnO thin film via plasma enhanced atomic layer deposition and its application for an inverted polymer solar cell. *AIP Adv.* 3 (2013) 102114.

[100] C. X. Shan, J. Y. Zhang, B. Yao, D. Z. Shen, and X. W. Fan. Ultraviolet photodetector fabricated from atomic-layer-deposited ZnO films. *J. Vac. Sci. Technol. B* 27 (2009) 1765.

[101] S.-H. K. Park, C.-S. Hwang, H. Y. Jeong, H. Y. Chu, and K. I. Cho. Transparent ZnO-TFT arrays fabricated by atomic layer deposition. *Electrochem. Solid-State Lett.* 11 (2008) H10.

[102] M. L. Kääriäinen, C. K. Weiss, S. Ritz, S. Pütz, D. C. Cameron, V. Mailänder, and K. Landfester. Zinc release from atomic layer deposited zinc oxide thin films and its antibacterial effect on Escherichia Coli. *Appl. Surf. Sci.* 287 (2013) 375.

[103] M. Vähä-Nissi, M. Pitkänen, E. Salo, E. Kenttä, A. Tanskanen, T. Sajavaara, M. Putkonen, J. Sievänen, A. Sneck, M. Rättö, M. Karppinen, and A. Harlin. Antibacterial and barrier properties of oriented polymer films with ZnO thin films applied with atomic layer deposition at low temperatures. *J. Solid State Chem.* 214 (2014) 7.

[104] D. Zhao, D. A. Mourey, and T. N. Jackson. Fast flexible plastic substrate ZnO circuits. *IEEE Electron Device Lett.* 340 (2010) 323.

[105] J. W. Elam, Z. A. Sechrist, and S. M. George. ZnO/Al_2O_3 nanolaminates fabricated by atomic layer deposition: growth and surface roughness measurements. *Thin Solid Films* 414 (2002) 43.

[106] D.-w. Choi, S.-J. Kim, J. H. Lee, K.-B. Chung, and J.-S. Park. A study of thin film encapsulation on polymer substrate using low temperature hybrid ZnO/Al_2O_3 layers atomic layer deposition. *Curr. Appl. Phys.* 12 (2012) S19.

[107] K. Lahtinen, T. Kääriäinen, P. Johansson, S. Kotkamo, P. Maydannik, Y. Seppänen, J. Kuusipalo, and D. C. Cameron. UV protective zinc oxide coating for biaxially oriented polypropylene packaging film by atomic layer deposition. *Thin Solid Films* 570 (2014) 33.

[108] V. Kekkonen, A. Hakola, T. Kajava, E. Sahramo, J. Malm, M. Karppinen, and R. H. A. Ras. Self-erasing and rewritable wettability patterns of ZnO thin film. *Appl. Phys. Lett.* 97 (2010) 044102.

[109] M. A. Lieberman and A. J. Lichtenberg. *Principles of Plasma Discharges and Materials Processing*. Wiley, New York, 2005.

[110] S. M. Rossnagel, A. Sherman, and F. Turner. Plasma-enhanced atomic layer deposition of Ta and Ti for interconnect diffusion barriers. *J. Vac. Sci. Technol. B* 18 (2013) 2016.

[111] R. J. Goldston and P. H. Rutherford. *Introduction to plasma physics*. IOP Publishing, Bristol, 1995.

[112] A. A. Fridman and L. A. Kennedy. *Plasma Physics and Engineering*. Taylor & Francis, New York, 2004.

[113] T. E. Sheridan and J. Goree. Collisional plasma sheath model. *Phys. Fluids B* 3 (1991) 2796.

[114] N. Xiang and F. L. Waelbroeck. Collisional sheath dynamics in the intermediate radio-frequency regime. *J. Appl. Phys.* 95 (2004) 860.

[115] J. T. Gudmundsson and M. A. Lieberman. On the role of metastables in capacitively coupled oxygen discharges. *Plasma Sources Sci. Technol.* 24 (2015) 035016.

[116] D. A. Toneli, R. S. Pessoa, M. Roberto, and J. T. Gudmundsson. On the formation and annihilation of the singlet molecular metastables in an oxygen discharge. *J. Phys. D: Appl. Phys.* 48 (2015) 325202.

[117] J. T. Gudmundsson, I. G. Kouznetsov, K. K. Patel, and M. A. Liebermann. Electronegativity of low-pressure high-density oxygen discharges. *J. Phys. D: Appl. Phys* 34 (2001) 1100.

[118] V. Laporta, R. Celiberto, and J. Tennyson. Dissociative electron attachment and electron-impact resonant dissociation of vibrationally excited O_2 molecules. *Phys. Rev. A.* 91 (2015) 012701.

[119] R. N. Franklin. Electronegative plasmas-why are they so different? *Plasma Sources Sci. Technol.* 4 (2002) A31.

[120] A. Aanesland, J. Breding, and P. Chabert. A review on ion-ion plasmas created in weakly magnetized electronegative plasmas. *Plasma Sources. Sci. Technol.* 23 (2014) 044003.

[121] S. G. Belostotsky, D. J. Economou, D. V. Lopaev, and T. V. Rakhimova. Negative ion destruction by O(^3P) atoms and $O_2(a^1\Delta_g)$ molecules in oxygen plasma. *Plasma Sources Sci. Technol.* 14 (2005) 532.

[122] J. T. Gudmundsson and B. Ventéjou. The pressure dependence of the discharge properties in a capacitively coupled oxygen discharge. *J. Appl. Phys.* 118 (2015) 153302.

[123] H. Singh, J. W. Coburn, and D. B. Graves. Recombination coefficients of O and N radicals on stainless steel. *J. Appl. Phys.* 88 (2000) 3748.

[124] R. L. Sharpless and T. G. Slanger. Surface Chemistry of metastable oxygen. II. Destruction of $O_2(a^1\Delta_g)$. *J. Chem. Phys.* 91 (1989) 7947.

[125] K. Kutasi and J. Loureiro. Role of the wall reactor material on the species density distributions in N_2–O_2 post-discharge for plasma sterilization. *J. Phys. D: Appl. Phys.* 40 (2007) 5612.

[126] U. Cvelbar, M. Mozetič, and A. Ricard. Characterization of oxygen plasma with a fiber optic catalytic probe and determination of recombination coefficients. *IEEE Trans. Plasma Sci.* 33 (2012) 834.

[127] P. Macko, P. Veis, and G. Cernogora. Study of oxygen atom recombination on a Pyrex surface at different wall temperatures by means of time-resolved actinometry in a double pulse discharge technique. *Plasma Sources Sci. Technol.* 13 (2004) 251.

[128] M. J. Sowa. Role of plasma enhanced atomic layer deposition reactor wall conditions on radical and ion fluxes. *J. Vac. Sci. Technol. A* 32 (2014) 01A106.

[129] H. C. M. Knoops, E. Langereis, M. C. M. van de Sanden, and W. M. M. Kessels. Conformality of plasma-assisted ALD: Physical processes and modeling. *J. Electrochem. Soc.* 157 (2010) G241.

[130] J. Dendooven, D. Deduytsche, J. Musschoot, R. L. Vanmeirhaege, and C. Detavernier. Conformality of Al_2O_3 and AlN deposited by plasma-enhanced atomic layer deposition. *J. Electrochem. Soc.* 157 (2010) G111.

[131] J. T. Gudmundsson and E. G. Thorsteinsson. Oxygen discharges diluted with argon: dissociation processes. *Plasma Sources Sci. Technol.* 16 (2007) 399.

[132] I. A. Kossyi, A. Y. Kostinsky, M. A. Matveyev, and V. P. Silakov. Kinetic scheme of the non-equilibrium discharge in nitrogen-oxygen mixture. *Plasma Sources Sci. Technol.* 1 (1992) 207.

[133] B. Gordiets and A. Ricard. Production of N, O, and NO in N_2–O_2 flowing discharges. *Plasma Sources. Sci. Technol* 2 (1993) 158.

[134] V. Guerra and J. Loureiro. Kinetic model of low-pressure microwave discharge in O_2–N_2 including the effects of O- ions on the characteristics for plasma maintenance. *Plasma Sources Sci. Technol.* 8 (1999) 110.

[135] H. B. Profijt, P. Kudlacek, M. C. M. van de Sanden, and W. M. M. Kessels. Ion and photon surface interaction during remote plasma ALD of metal oxides. *J. Electrochem. Soc.* 158 (2011) G88.

[136] S. B. S. Heil, J. L. van Hemmen, M. C. M. van de Sanden, and W. M. M. Kessels. Reaction mechanisms during plasma-assisted atomic layer deposition of metal oxides: A case study of Al_2O_3. *J. Appl. Phys.* 103 (2008) 103302.

[137] E. Langereis, J. Keijmel, M. C. M. van de Sanden, and W. M. M. Kessels. Surface chemistry of plasma-assisted atomic layer deposition of Al_2O_3 studied by infrared spectroscopy. *Appl. Phys. Lett.* 92 (2008) 231904.

[138] V. R. Rai, V. Vandalon, and S. Agarwal. Surface reaction mechanisms during ozone and oxygen plasma assisted atomic layer deposition of aluminum oxide. *Langmuir* 26 (2010) 13732.

[139] V. R. Rai, V. Vandalon, and S. Agarwal. Influence of surface temperature on the mechanism of atomic layer deposition aluminum oxide using an oxygen plasma and ozone. *Langmuir* 28 (2012) 350.

[140] H. C. M. Knoops, K. de Peuter, and W. M. M. Kessels. Redeposition in plasma-assisted atomic layer deposition: Silicon nitride film quality ruled by the gas residence time. *Appl. Phys. Lett.* 107 (2015) 014102.

[141] J. Musschoot. “Advantages and challenges of plasma enhanced atomic layer deposition”. PhD thesis. Universiteit Gent, 2011.

[142] T. Silva, N. Britun, T. Godfroid, and R. Snyders. Optical characterization of a microwave pulsed discharge used for dissociation of CO_2. *Plasma Sources Sci. Technol* 23 (2014) 025009.

[143] H. B. Profijt, M. C. M. van de Sanden, and W. M. M. Kessels. Substrate-biasing during plasma-assisted atomic layer deposition to tailor metal-oxide thin film growth. *J. Vac. Sci. Technol. A* 31 (2013) 01A106.

[144] S. Ratzsch, E.-B. Kley, A. Tünnermann, and A. Szeghalmi. Influence of the oxygen plasma parameters on the atomic layer deposition of titanium dioxide. *Nanotechnology* 26 (2015) 024003.

[145] J. Kim, S. Kim, H. Kang, J. Choi, H. Jeon, M. Cho, K. Chung, S. Back, K. Yoo, and C. Bae. Composition, structure and electrical characteristics of HfO_2 gate dielectrics grown using the remote- and direct-plasma atomic layer deposition methods. *J. Appl. Phys.* 98 (2005) 094504.

[146] N. Samal, H. Du, R. Luberoff, K. Chetry, R. Bubber, A. Hayes, and A. Devasahayam. Low-temperature ($\leq 200°C$) plasma enhanced atomic layer deposition of dense titanium nitride films. *J. Vac. Sci. Technol. A* 31 (2013) 01A137.

[147] S. Ratzsch, E.-B. Kley, A. Tünnermann, and A. Szeghalmi. Inhibition of Crystal growth during plasma enhanced atomic layer deposition by applying bias. *Materials* 8 (2015) 7805.

[148] H. Kim, S. Woo, J. Lee, Y. Kim, H. Lee, I.-J. Choi, Y.-D. Kim, C.-W. Chung, and H. Jeon. Effect of DC bias on the plasma properties in remote plasma atomic layer deposition and its application to HfO_2 thin films. *J. Electrochem. Soc.* 158 (2011) H21.

[149] J.-C. Kwak, Y.-H. Lee, and B.-H. Choi. Preparation of tantalum oxide thin films by photo-assisted atomic layer deposition. *Appl. Surf. Sci.* 230 (2004) 249.

[150] B. H. Lee, S. C. J. K. Hwang, S. H. Kim, and M. M. Sung. UV-enhanced atomic layer deposition of ZrO_2 thin films at room temperature. *Thin Solid Films* 518 (2010) 6432.

[151] K. H. Yoon, H. Kim, Y.-E. K. Lee, N. K. Shrestha, and M. M. Sung. UV-enhanced atomic layer deposition of Al_2O_3 thin films at low temperature for gas-diffusion barriers. *RCS Adv.* 7 (2017) 5601.

[152] T. O. Kääriäinen, D. C. Cameron, and M. Tanttari. Adhesion of Ti and TiC Coatings on PMMA Subject to Plasma Treatment: Effect of Intermediate Layers of Al_2O_3 and TiO_2 Deposited by Atomic Layer Deposition. *Plasma Process. Polym.* 6 (2009) 631.

[153] H. Ren, Y. Nishi, and J. L. Shohet. Changes to charge and defects in dielectrics from ion and photon fluences during plasma exposure. *Electrochem. Solid-State Lett.* 14 (2011) H107.

[154] A. Niskanen, A. Rahtu, T. Sajavaara, K. Arstila, M. Ritala, and M. Leskelä. Radical-enhanced atomic layer deposition of metallic copper thin films. *J. Electrochem Soc.* 152 (2005) G25.

[155] A. Niskanen, U. Kreissig, M. Leskelä, and M. Ritala. Radical enhanced atomic layer deposition of tantalum oxide. *Chem. Mater.* 19 (2007) 2316.

[156] C. D. Pham, J. Chang, M. A. Zurbuchen, and J. P. Chang. Synthesis and characterization of $BiFeO_3$ thin films for multiferroic applications by radical enhanced atomic layer deposition. *Chem. Mater.* 27 (2015) 7282.

[157] S. Tinck and A. Bogaerts. Computer simulations of an oxygen inductively coupled plasma used for plasma-assisted atomic layer deposition. *Plasma Sources Sci. Technol.* 20 (2011) 015008.

[158] A. Matsuda and K. Tanaka. Investigation of the growth kinetics of glow-discharge hydrogenated amorphous silicon using a radical separation technique. *J. Appl. Phys.* 60 (1986) 2351.

[159] Y. Show, Y. Yabe, T. Izumi, and H. Yamauchi. Development of triode type RF plasma enhanced CVD equipment for low-temperature growth of carbon nanotube. *Diam. Rel. Mater.* 14 (2005) 1848.

[160] T. O. Kääriäinen and D. C. Cameron. Plasma-Assisted Atomic Layer Deposition of Al_2O_3 at Room Temperature. *Plasma Process. Polym.* 6 (2009) S237.

[161] M. Bosund, T. Sajavaara, M. Laitinen, T. Huhtio, M. Putkonen, V.-M. Airaksinen, and H. Lipsanen. Properties of AlN grown by plasma enhanced atomic layer deposition. *Appl. Surf. Sci.* 257 (2011) 7827.

[162] A. Grill, ed. *Cold plasma materials fabrication: From fundamentals to applications*. IEEE Press, New York, 1994.

[163] M. A. Lieberman and V. A. Godyak. From Fermi acceleration to collisionless discharge heating. *IEEE Trans. Plasma Sci.* 26 (1998) 955.

[164] F. F. Chen. *Capacitor tuning circuits for inductive loads*. 1992. URL: www.seas.ucla.edu/~ffchen/Publs/Chen144.pdf.

[165] E. Kawamura, V. Vahedi, M. A. Liebermann, and C. K. Birdsall. Ion energy distribution in rf sheaths; review, analysis and simulations. *Plasma Sources Sci. Technol.* 8 (1999) R45.

[166] V. A. Godyak, R. B. Piejak, and B. M. Alexandrovich. Electron energy distribution function measurements and plasma parameters in inductively coupled argon plasma. *Plasma Sources Sci. Technol.* 11 (2002) 525.

[167] J. Hopwood. Review of inductively coupled plasmas for plasma processing. *Plasma Sources Sci. Technol.* 1 (1992) 109.

[168] H. B. Profijt and W. M. M. Kessels. Ion bombardment during plasma-assisted atomic layer deposition. *ECS Trans.* 50 (2013) 23.

[169] M. Putkonen, T. Sajavaara, L. Niinistö, and J. Keinonen. Analysis of ALD-processed thin films by ion-beam techniques. *Anal. Bioanal. Chem.* 382 (2005) 1791.

[170] M. Laitinen, M. Rossi, J. Julin, and T. Sajavaara. Time-of-flight – Energy spectrometer for elemental depth profiling – Jyväskylä design. *Nucl. Instrum. Meth. B* 337 (2014) 55.

[171] K. Arstila, J. Julin, M. Laitinen, J. Aalto, T. Konu, S. Kärkkäinen, S. Rahkonen, M. Raunio, J. Itkonen, J.-P. Santanen, T. Tuovinen, and T. Sajavaara. Potku – New analysis software for heavy ion elastic recoil detection analysis. *Nucl. Instrum. Meth. B* 331 (2014) 34.

[172] M. Ohring. *Materials Science of Thin Films*. 2nd ed. Academic Press, San Diego, 2002.

[173] D. K. Schroder. *Semiconductor material and device characterization*. 3rd ed. John Wiley & Sons, New Jersey, 2006.

[174] L. Sabbatini, ed. *Polymer surface characterization*. de Gruyter, Berlin, 2014.

[175] B. C. Smith. *Fundamentals of Fourier transform infrared spectroscopy*. 2nd ed. CRC Press, Boca Raton, 2011.

[176] G. Hlawacek and A. Gölzhäuser, eds. *Helium Ion Microscopy*. Springer, Switzerland, 2016.

[177] A. J. M. Mackus, S. B. S. Heil, E. Langereis, H. C. M. Knoops, M. C. M. van de Sanden, and W. M. M. Kessels. Optical emission spectroscopy as a tool for studying, optimizing, and monitoring plasma-assisted atomic layer deposition processes. *J. Vac. Sci. Technol. A* 28 (2010) 77.

[178] U. Fantz. Basics of plasma spectroscopy. *Plasma Sources Sci. Technol.* 15.4 (2006) S137.

[179] National Institute of Standards and Technology. *NIST Atomic Spectra Database*. URL: https://www.nist.gov/pml/atomic-spectra-database.

[180] E. Biémont and C. J. Zeippen. Electric dipole transitions in atomic oxygen and the lifetimes of the $2p^3(^4S^0)3s\ ^5S^0$ and $^3S^0$ states. *Astron. Astrophys* 256 (1992) 1036.

[181] A. Lofthus and P. H. Krupenie. Spectrum of Molecular Nitrogen. *Phys. Chem. Ref. Data* 6 (1977) 113.

[182] F. R. Gilmore. Potential energy curves for N_2, NO, and O_2 and correponding ions. *J. Quant. Spectrosc. Radiat. Transfer* 5 (1965) 369.

[183] Phys4Entry. *Database for European Phys4Entry Project*. 2012–2014. URL: http://users.ba.cnr.it/imip/cscpal38/phys4entry/database.html.

[184] G. N. Parsons, S. E. Atanasov, E. C. Dandley, C. K. Devine, B. Gong, J. S. Jur, K. Lee, C. J. Oldham, Q. Peng, J. C. Spagnola, and P. S. Williams. Mechanisms and reactions during atomic layer deposition on polymers. *Coord. Chem. Rev.* 257 (2013) 3323.

[185] S.-M. Lee, E. Pippel, U. Gösele, C. Dresbach, Y. Quin, C. V. Chadran, T. Bräuningen, G. Hause, and M. Knez. Greatly increased toughness of infiltrated spider silk. *Science* 324 (2009) 488.

[186] B. Gong, Q. Peng, J. S. Jur, C. K. Devine, K. Lee, and G. N. Parsons. Sequential vapor infiltration of metal oxides into sacrificial polyester fibers: Shape replication and controlled porosity of microporous/mesoporous oxide monoliths. *Chem. Mater.* 23 (2011) 3476.

[187] C. A. Wilson, R. K. Grubbs, and S. M. George. Nucleation and growth during Al_2O_3 atomic layer deposition on polymers. *Chem. Mater.* 17 (2005) 5625.

[188] R. J. Crawford. *Plastics Engineering*. 3rd ed. Butterworth-Heinemann, Burlington, 1998.

[189] M. Gad-El-Hak, ed. *MEMS Handbook*. CRC Press LLC, Boca Raton, Florida, 2002.

[190] J. S. Spagnola, B. Gong, S. A. Arvidson, J. S. Jur, S. A. Khan, and G. N. Parsons. Surface and sub-surface reactions during low-temperature aluminium oxide atomic layer deposition on fiber-forming polymers. *J. Mater. Chem.* 20 (2010) 4213.

[191] K. Guan. Relationship between photocatalytic activity, hydrophilicity and self-cleaning effect of TiO_2/SiO_2 films. *Surf. Coat. Technol.* 191 (2005) 155.

[192] J. Malm, E. Sahramo, M. Karppinen, and R. H. A. Ras. Photo-controlled wettability switching by conformal coating on nanoscale topographies with ultrathin oxide films. *Chem. Mater.* 22 (2010) 3349.

[193] S. E. Potts, H. B. Profijt, R. Roelofs, and W. M. M. Kessels. Room-temperature ALD of metal oxide thin films by energy-enhanced ALD. *Chem. Vap. Deposition* 19 (2013) 1.

[194] T. Nam, J.-M. Kim, M.-K. Kim, H. Kim, and W.-H. Kim. Low-temperature atomic layer deposition of TiO_2, Al_2O_3, and ZnO thin films. *J. Korean Phys. Soc.* 59 (2011) 452.

[195] K. Kanomata, P. P. Pansila, B. Ahmmad, S. Kubota, K. Hirahara, and F. Hirose. Infrared study of room-temperature atomic layer deposition of TiO_2 using tetrakis(dimethylamino)titanium and remote-plasma-excited water vapor. *Appl. Surf. Sci.* 308 (2014) 328.

[196] K. Kikuchi, M. Miura, K. Kanomata, B. Ahmmad, S. Kubota, and F. Hirose. Room temperature atomic layer deposition of TiO_2 on gold nanoparticles. *J. Vac. Sci. Technol. A* 35 (2017) 01B121.

[197] A. Strobel, H.-D. Schnabel, U. Reinhold, S. Rauer, and A. Neidhardt. Room temperature plasma enhanced atomic layer deposition of TiO_2 and WO_3 films. *J. Vac. Sci. Technol. A* 34 (2016) 01A118.

[198] K. Kanomata, H. Ohba, P. P. Pansila, B. Ahmmad, S. Kubota, K. Hirahara, and F. Hirose. Infrared study of room-temperature atomic layer deposition of HfO_2 using tetrakis(ethylmethylamino)hafnium and remote plasma oxidizing agents. *J. Vac. Sci. Technol. A* 33 (2015) 01A113.

[199] K. Kanomata, K. Tokoro, T. Imai, P. P. Pansila, M. Miura, B. Ahmmad, S. Kubota, K. Hirahara, and F. Hirose. Room-temperature atomic layer deposition of ZrO_2 using tetrakis(ethylmethyl)zirconium and plasma-excited humidified argon. *Appl. Surf. Sci.* 387 (2016) 497.

[200] A. J. M. Mackus, D. Garcia-Alonso, H. C. M. Knoops, A. A. Bol, and W. M. M. Kessels. Room-temperature atomic layer deposition of platinum. *Chem. Mater.* 25 (2013) 1769.

[201] V. Verlaan, L. R. J. G. van den Elzen, G. Dingemans, M. C. M. van de Sanden, and W. M. M. Kessels. Composition and bonding structure of plasma-assisted ALD Al_2O_3 films. *Phys. Status Solidi C* 7 (2010) 976.

[202] T. O. Kääriäinen, S. Lehti, M.-L. Kääriäinen, and D. C. Cameron. Surface modification of polymers by plasma-assisted atomic layer deposition. *Surf. Coat. Technol.* 205 (2011) S475.

[203] P. Gröning, O. M. Küttel, M. Collaud-Coen, G. Dietler, and L. Schlapbach. Interaction of low-energy ions (< 10 eV) with polymethylmethacrylate during plasma treatment. *Appl. Surf. Sci.* 89 (1995) 83.

[204] A. C. Fozza, J. E. Klemberg-Sapieha, A. Kruse, A. Holländer, and M. R. Wertheimer. Oxidation and ablation of polymers by vacuum-UV radiation from low-pressure plasmas. *Nucl. Instrum. Meth. B* 131 (1997) 205.

[205] Y. Setsuhara, K. Cho, K. Takenaka, M. Shiratani, M. Sekine, M. Hori, E. Ikenaga, and S. Zaima. Low-damage surface modification of polymethylmethacrylate with argon–oxygen mixture plasmas driven by multiple low-inductance antenna units. *Thin Solid Films* 518 (2010) 3561.

[206] K. Cho, Y. Setsuhara, K. Takenaka, M. Shiratani, M. Sekine, and M. Hori. Effects of photoirradiation in UV and VUV regions during plasma exposure to polymers. *Thin Solid Films* 519 (2011) 6810.

[207] J.-H. Park, S. H. Lee, K. H. Choi, H. S. Noh, J. W. Lee, and S. J. Pearton. Comparison of dry etching of PMMA and polycarbonate in diffusion pump-based O_2 capacitively coupled plasma and inductively coupled plasma. *Semicond. Sci. and Technol.* 518 (2010) 6465.

[208] A. C. Fozza, J. E. Klemberg-Sapieha, and M. R. Wertheimer. Vacuum Ultraviolet Irradiation of Polymers. *Plasmas Polym.* 4 (1999) 183.

[209] A. Vesel and M. Mozetic. Surface modification and ageing of PMMA polymer by oxygen plasma treatment. *Vacuum* 86 (2012) 634.

[210] M. Collaud Coen, R. Lehmann, P. Groening, and L. Schlapbach. Modification of the micro- and nanotopography of several polymers by plasma treatments. *Appl. Surf. Sci.* 207 (2003) 276.

[211] V. A. Godyak, R. B. Piejak, and B. M. Alexandrovich. Measurements of electron energy distributions in low-pressure RF discharges. *Plasma Sources Sci. Technol.* 1 (1992) 36.

[212] S. J. You, S. K. Ahn, and H. Y. Chang. Driving frequency effect on electron heating mode transition in capacitive discharge. *Appl. Phys. Lett* 89 (2006) 171502.

[213] P. Belenguer and J. P. Boeuf. Transition between different regimes of rf glow discharges. *Phys. Rev. A* 41 (1999) 4447.

[214] S. Y. Moon, J. K. Rhee, D. B. Kim, B. M. Gweon, and W. Choe. Capacitive discharge mode transition in moderate and atmospheric pressure. *Curr. Appl. Phys.* 9 (2009) 274.

[215] V. Lisovskiy, J.-P. Booth, K. Landry, D. Douai, V. Cassange, and V. Yegorenkov. Modes and the alpha–gamma transition in rf capacitive discharges in N_2O at different rf frequencies. *Phys. Plasmas* 13 (2006) 103505.

[216] I. Odrobina and M. Kando. Discontinuous transitions between alpha and gamma regimes of rf capacitive discharges. *Plasma Sources Sci. Technol.* 5 (1996) 517.

[217] A. Derzsi, I. Korolov, E. Schüngel, Z. Donko, and J. Schulze. Effects of fast atoms and energy-dependent secondary electron emission yields in PIC/MCC simulations of capacitively coupled plasmas. *Plasma Sources Sci. Technol.* 24 (2015) 034002.

[218] V. Lisovskiy and V. Yegorenkov. Alpha–gamma transition in RF capacitive discharge in low-pressure oxygen. *Vacuum* 74 (2004) 19.

[219] X. Yang, M. Moravej, G. R. Nowling, S. E. Babayan, J. Panelon, J. P. Chang, and R. F. Hicks. Comparison of an atmospheric pressure, radio-frequency discharge operating in the α and γ modes. *Plasma Sources Sci. Technol.* 14 (2005) 314.

[220] P. Vidaud, S. M. A. Durrani, and D. R. Hall. Alpha and gamma RF capacitative discharges in N_2 at intermediate pressures. *J. Phys. D: Appl. Phys.* 21 (1988) 57.

[221] V. Lisovskiy, J.-P. Booth, K. Landry, D. Douai, V. Cassagne, and V. Yegorenkov. RF discharge dissociative mode in NF_3 and SiH_4. *J. Phys. D: Appl. Phys* 40 (2007) 6631.

[222] V. Lisovskiy, J.-P. Booth, J. Jolly, S. Martins, K. Landry, D. Douai, V. Cassagne, and V. Yegorenkov. Modes of rf capacitive discharge in low-pressure sulfur hexafluoride. *J. Phys. D: Appl. Phys* 40 (2007) 6989.

[223] Y. Itikawa. Cross sections for electron collisions with nitrogen molecules. *J. Phys. Chem. Ref. Data* 35 (2006) 31.

[224] S. Y. Moon, J. K. Rhee, D. B. Kim, and W. Choe. α, γ, and normal, abnormal glow discharge modes in radio-frequency capacitively coupled discharges at atmospheric pressure. *Phys. Plasmas* 13 (2006) 033502.

[225] E. Abdel-Fattah and O. F. Farag. Alpha to gamma mode transition in hydrogen capacitive radio-frequency discharge. *J. Can. Phys.* 91 (2013) 1062.

[226] H. Van Bui, A. W. Groenland, A. A. I. Aarnink, R. A. M. Wolters, J. Schmitz, and A. Y. Kovalgin. Growth kinetics and oxidation mechanism of ALD TiN Thin film monitored by in situ spectroscopic ellipsometry. *J. Electrochem. Soc.* 158 (2011) H214.

[227] J. I. Hong, S. H. Seo, S. S. Kim, N. S. Yoon, and C. S. C. adn H. Y. Chang. Electron temperature control with grid bias in inductively coupled argon plasma. *Phys. Plasmas* 6 (1999) 107.

[228] T. Wegner, C. Küllig, and J. Meischner. E-H transition in argon/oxygen inductively coupled RF plasmas. *Contrib. Plasma Phys.* 55 (2015) 728.

[229] U. Kortshagen, N. D. Gibson, and J. E. Lawler. On the E - H mode transition in RF inductive discharges. *J. Appl. Phys. D: Appl. Phys.* 29 (1996) 1224.

[230] J.-K. Lee, H. Lee, and C.-W. Chung. E-H mode transition in inductively coupled plasma using Ar, O_2, N_2, and mixture gas. *Curr. Appl. Phys.* 11 (2011) S149.

[231] Z. M. Jelenak, Z. B. Velikić, J. V. Božin, Z. L. Petrović, and B. M. Jelenković. Electronic excitation of the 750- and 811-nm lines of argon. *Phys. Rev. E* 47 (1993) 3566.

[232] P. Palmeri and E. Biémont. Energy levels of high /-states in neutral and singly ionized argon. *Phys. Scr.* 51 (1995) 76.

[233] T. Wegner, C. Küllig, and J. Meischner. On the E-H transition in inductively coupled radio frequency oxygen plasmas: I. Density and temperature of electrons, ground state and singlet metastable molecular oxygen. *Plasma Sources Sci. Technol.* 26 (2017) 025006.

[234] T. Wegner, C. Küllig, and J. Meischner. On the E-H transition in inductively coupled radio frequency oxygen plasmas: II. Electronegativity and the impact on particle kinetics. *Plasma Sources Sci. Technol.* 26 (2017) 025007.

[235] A. Fateev, F. Leipold, Y. Kusano, B. Stenum, E. Tsakadze, and H. Bislev. Plasma chemistry in an atmospheric pressure Ar/NH_3 dielectric barrier discharge. *Plasma Process. Polym.* 2.1 (2005) 193.

[236] S. J. Kang and V. M. Donelly. Optical absorption and emission spectroscopy studies of ammonia-containing plasmas. *Plasma Sources Sci. Technol.* 16 (2007) 265.